Spring 2017

Crabbing System for an Electron-Ion Collider

Alejandro Castilla
Old Dominion University

CRABBING SYSTEM FOR AN ELECTRON-ION COLLIDER

by

Alejandro Castilla
B.E. September 2007, Universidad Autónoma de Yucatán, Mexico.
M.S. January 2010, Universidad de Guanajuato, Mexico.
M.S. May 2013, Old Dominion University.

A Dissertation Submitted to the Faculty of
Old Dominion University in Partial Fulfillment of the
Requirements for the Degree of

DOCTOR OF PHILOSOPHY

PHYSICS

OLD DOMINION UNIVERSITY
May 2017

Approved by:

Jean Roger Delayen (Director)

Mauro Napsuciale Mendívil (Co-Director)

Rocco Schiavilla (Member)

Geoffrey Krafft (Member)

Todd Satogata (Member)

Mileta Tomovic (Member)

ABSTRACT

CRABBING SYSTEM FOR AN ELECTRON-ION COLLIDER

Old Dominion University, 2017
Director: Dr. Jean Roger Delayen
Co-Director: Dr. Mauro Napsuciale Mendívil

As high energy and nuclear physicists continue to push further the boundaries of knowledge using colliders, there is an imperative need, not only to increase the colliding beams' energies, but also to improve the accuracy of the experiments, and to collect a large quantity of events with good statistical sensitivity. To achieve the latter, it is necessary to collect more data by increasing the rate at which these processes are being produced and detected in the machine. This rate of events depends directly on the machine's luminosity. The luminosity itself is proportional to the frequency at which the beams are being delivered, the number of particles in each beam, and inversely proportional to the cross-sectional size of the colliding beams. There are several approaches that can be considered to increase the events statistics in a collider other than increasing the luminosity, such as running the experiments for a longer time. However, this also elevates the operation expenses, while increasing the frequency at which the beams are delivered implies strong physical changes along the accelerator and the detectors. Therefore, it is preferred to increase the beam intensities and reduce the beams cross-sectional areas to achieve these higher luminosities. In the case where the goal is to push the limits, sometimes even beyond the machines design parameters, one must develop a detailed **High Luminosity Scheme**. Any high luminosity scheme on a modern collider considers—in one of their versions—the use of crab cavities to correct the geometrical reduction of the luminosity due to the beams crossing angle. In this dissertation, we present the design and testing of a proof-of-principle compact superconducting crab cavity, at 750 MHz, for the future electron-ion collider, currently under design at Jefferson Lab. In addition to the design and validation of the cavity prototype, we present the analysis of the first order beam dynamics and the integration of the crabbing systems to the interaction region. Following this, we propose the concept of **twin crabs** to allow machines with variable beam transverse coupling in the interaction region to have full crabbing in only the desired plane. Finally, we present recommendations to extend this work to other frequencies.

ACKNOWLEDGEMENTS

First of all, I would like to sincerely thank my supervisor Dr. Jean Delayen, for all the support and time that he invested in my long journey through my research and studies. To my supervisor Dr. Mauro Napsuciale, for all the trust he has had in me throughout these years, I would not be here without his guidance. I would like to thank the Physics Department at Old Dominion University and the Physics Department at the University of Guanajuato, for all their support, patience, and for all the professors and colleagues from whom I have learnt so much. I am very thankful to CONACYT for all the support.

To Dr. Hari Areti and the JSA for all the encouragement and support given to me and my young colleagues. To Dr. Todd Satogata and Dr. Vasiliy Morozov from the Center for Advanced Studies of Accelerator at Jefferson Lab, for all the time and positive attitude that they spent and showed while letting me learn from them, it was really one of the best parts of my research experience. To Joe Preble, Bob Rimmer, Tom Powers, Kirk Davis, and Pete Kushnick from the Superconducting Radiofrequency Institute at Jefferson Lab, for letting me and my colleagues learn from the best and carry out our experimental work without causing too many disasters, I would like to specially thank the amazing technical support of: Chris Dreyfuss, Roland Overton, and of course Danny Forehand, you guys rock!

To Terry Grim, Chase Boulware, and Dmitry Gorelov at Niowave, Inc. for their help and work done building and testing the 750 MHz crab cavity. To my thesis committee, for their time and helpful comments. I would like to give special thanks to my brothers and sisters in arms, my friends and colleagues: Chris Hopper, HyeKyoung Park, Kevin Mitchell, and of course Subashini De Silva, for all the tears, sweat, and blood shed day and night throughout our discussions and experimental work. To Carlos Hernandez-Garcia and his family, for their friendship, inspiration and support, it did not pass unnoticed.

Finally and most importantly, to all my friends and family, that in the good and the ill have endured with me and lifted my spirit up, you all occupy a special place in my life.

TABLE OF CONTENTS

LIST OF TABLES

LIST OF FIGURES

CHAPTER 1

INTRODUCTION

1.1 MOTIVATION

In the search of shedding light into the processes of nature, that have not been yet accessible to modern scientific research, more and more advanced experiments are under construction or design. In order to gather the observables of rare physical processes, many experiments using colliders are foreseen to use particles at higher energies, more stable beams, higher polarization, more precise and complex detection systems, and higher statistics. To reach these goals, accelerator physicists must push the machine design to their limits. Multiple interaction regions with higher acceptance detector capabilities are necessary to carry out these experiments, but also impose strict dimensional constrictions on the machine, at the same time that introduce beam crossing angles to reduce parasitic collisions, to allow forward detection, etc. These crossing angles and cramped spaces near the interaction regions give some extra complications: first of all, the need of crabbing correctors to restore the luminosity, and secondly, they require compact crab cavity designs that can sustain the necessary transverse voltages to provide the correct rotation of the bunches at the interaction point, which can also fit in the reduced available space in the tunnels.

Jefferson Lab is one of the places where the study of nuclear physics and the Standard Model is of main focus. This facility is currently running under its brand new 12 GeV upgrade era and it is expected to extend in the following years the already successful list of discoveries made under their 6 GeV lifetime [1]. Many experiments including electron-proton and electron-ion deep inelastic scattering are waiting to prove and push the latest theories of nuclear and elementary particle physics. However, a great effort in designing and proposing the next step has already been undergoing for the past few years, namely the Electron-Ion Collider (EIC).

The EIC will collide beams of electrons, protons, and several species of ions, over a wide energy range. Amongst its many peculiarities, the EIC interaction region imposes a relatively large beam crossing angle of 50 mrad. Therefore, in order to achieve the luminosity requirements ($\sim 10^{34}$ cm^{-2}s^{-1}), crabbing systems are needed to restore the luminosity. The goals of this research dissertation are to optimize and test a superconducting rf dipole geometry for a 750 MHz crabbing application for the EIC, and to analyse—up to first order—some of the complications and considerations occurring when integrating the crabbing systems to the interaction region. These complications include synchro-betatron coupling and implications of crabbing in the presence of beam transverse coupling. Resulting from these studies, some novel mitigation schemes are proposed for these cases. More generally, these schemes could allow crabbing systems to provide full crossing angle correction in machines with variable transverse coupling at their interaction regions.

1.1.1 ABOUT SRF DEFLECTING AND CRABBING DESIGNS

The principal use of radiofrequency cavities in accelerators is to accelerate beams. The most common geometry of the accelerating cavities is the elliptical geometry, operated in its lowest resonant mode, the so-called TM_{010} mode. The TM_{010} mode has a longitudinal field that couples to the beam charges, thus, increasing their longitudinal momentum. While the elliptical cavities are the most suitable for high β particles, for low and medium β particles, other more complex, TEM structures are commonly used, such as the quarter-wave, half-wave, or spoke cavities. Recent developments have also allowed the use of spoke cavities for high-beta applications [2].

A less common type of rf cavities are those that can provide transverse momentum to the beams. Such type of cavities are called—in general—**transverse deflectors**. However, depending on their application, they are also known simply as deflectors, separators, or crab cavities. The study and applications of transverse deflectors is a growing field and most of the modern and future colliders adopt—for their high luminosity schemes—the use of crab cavities to reach their experimental goals.

A deflector/separator will simply change the transverse momentum of the centroid of the beam bunches, changing the direction of their trajectory downstream, or **deflecting** the beam. In a nutshell, a crab cavity is a deflector that imprints a transverse momentum equal and in opposite direction to the particles in the head and the tail of the beam bunches, respectively, while the effective transverse momentum given to the centroid of the bunch is zero. A crab cavity, therefore, will not perturb the trajectory of the bunches or effectively change their longitudinal momentum, but will cause a rotation downstream that—following the beam's beta functions in the interaction region—will be maximum at $(2n+1)\pi/2$ and minimum at $n\pi$ for the phase advance in the direction of the crabbing. Transverse deflectors are also used for beam diagnostics, emittance exchange, and x-ray pulse compression [3].

On the other hand, superconducting resonant cavities provide a series of advantages over normal conducting cavities, such as higher gradients during continuous-wave (CW) operation, higher shunt impedance, and reduced power dissipation. Even when they require cryogenic systems to operate, they can still lower the cost of operation and reach tough specification levels that would not be achievable using normal conducting technology. As mentioned before, the main advantage of the superconducting materials is that they are not limited by ohmnic losses like their normal conducting predecessors and, with a proper design and optimisation, it is possible to obtain compact structures that cope with some of the tight spacial constraints that many of the complicated lattices have in their interaction regions.

Many deflecting and crabbing structures have been designed and operated since the 1960's all over the world, commonly using the transverse magnetic field of the TM_{110} mode in an elliptical—or squashed elliptical—cavity to change the transverse momentum of the particles [4]. However, the need of compact structures [5] have pushed TEM and TE-like type of geometries to be more attractive and feasible for the modern applications, where the particles' transverse momentum change is given mostly by the transverse electric field component of the crabbing modes.

The compact rf dipole geometry has already been optimized for several other deflecting (at 499 MHz for the Continuos Electron Beam Accelerator Facility's 12 GeV upgrade at Jefferson Lab) and crabbing applications (at 400 MHz for the High Luminosity Upgrade of the LHC at CERN) [6]. For this reason, we have found the rf dipole geometry, to be a suitable candidate for the EIC crab cavities.

1.2 SCIENCE AT THE 12 GEV CEBAF: THE NEAR FUTURE

The motivation behind the 12 GeV upgrade of the CEBAF itself, is based on that, currently, significant challenges are still in place for nuclear and particle physics. For example: exploring the non-Abelian nature of Quantum Chromodynamics (QCD), the strong coupling at low energies, or the production of exotic mesons from excitations of the gluon field. Multidimensional images of hadrons could give an insight on the spin content of the nucleon through observables related to the orbital angular momenta of quarks and gluons. Furthermore, the capability to have high intensity (up to 180 μA in CW), highly polarized (86%) electron beams, with improved stability, provides a new opportunity for probing and extending the Standard Model. Or, as Dudek et al. put it in [7]:

"*...the 12 GeV upgrade of the CEBAF at Jefferson Lab will enable a new experimental program with potential to address these and other important topics in nuclear, hadronic, and electroweak physics.* "

The Jefferson Lab Program Advisory Committee (PAC) has presently approved 52 proposals of experiments that will require the upgraded facility to run nearly at full efficiency for 6 years, extending its productivity into the 2020's.

1.3 THE EIC: ONE STEP FURTHER

In order to understand the dynamical origin of mass in the macroscopic universe along with the behavior of matter at densities and temperatures in astrophysical contexts, it is crucial to understand—from first principles—the internal structure of hadrons and nuclei on the basis of the fundamental theory of strong interactions, QCD. Theoretical QCD methods have been greatly developed in the last couple of decades, but rely vitally on new experimental information for further progress. As yet, there are still several open questions to understand [8]:

1. The three-dimensional structure of the nucleon in QCD: non-valence quarks and gluons spatial distributions, orbital motion, polarization and correlations.

2. The fundamental color fields in nuclei: nuclear parton densities, shadowing, coherence effects, color transparency.

3. The conversion of color charge to hadrons: fragmentation, parton propagation through matter, in-medium jets.

A polarized electron-ion collider, with a variable *ep* center-of-mass (CM) energy in the range of $\sqrt{s} = 20 - 70$ GeV and luminosity of $\sim 10^{34}\text{cm}^{-2}s^{-1}$ over most of its range, would offer a unique opportunity to address these questions. It will represent the natural next step after the high-luminosity fixed-target ep/eA experiments (JLab 12 GeV, SLAC) and the high-energy HERA *ep* collider (protons only, unpolarized). The design proposed by Jefferson Lab (JEIC) would use the 11 GeV CEBAF electron accelerator and a newly built ion complex as injectors for a ring-ring ep/eA collider with energies $E_e = 4-10$ GeV and $E_p = 20-100$ GeV and a circumference of ~ 1 km, slightly smaller than that of the present CEBAF accelerator. The interaction regions at the JEIC include ultra high to essentially full detector acceptance capabilities [9].

1.3.1 TECHNICALITIES OF THE JEIC

To have a full acceptance detector, a relatively large crossing angle (50 mrad) of the colliding beams has to be introduced. Then, the only way to reach the high luminosity required is to implement crab crossing correctors. A crab cavity suitable for this application is an rf deflector that operates at the transverse voltages needed to restore this angle for both protons up to 100 GeV and electrons up to 10 GeV. The proposed design as a crab cavity candidate for the EIC at Jefferson Lab is an rf dipole geometry, which operates on a fundamental TE-like mode.

From the points described above as expectations for the nuclear physics program, the technical requirements for the EIC machine can be summarised roughly as:

1. The CM energy should be between 15 and 65 GeV, $s = (4E_eE_u)$ from a few hundred to a few thousand GeV^2, where E_e and E_u are the kinetic energies of the electron and nucleon respectively. So the colliding beams should range:

   - from 4 to 10 GeV for electrons,
   - from 30 to 100 GeV for protons,
   - and up to 40 GeV per nucleon for ions,

   while $<$ 20 GeV protons and ions are interesting for other physics processes investigations.

2. Polarized protons, deuterons, and helium-3 are attractive to use, among other polarized light ions and heavy ions up to lead without polarization.

3. Three detectors with at least two of them available for collisions of electrons with medium energy ions. A third detector is desirable for electron collisions with ions of $<$ 20 GeV/u.

4. 70% of longitudinal polarization for both electron and light-ion beams at the collision points should be achieved. Transverse polarization of the ions and spin-flip of both beams at the collision point are desired. And $1 - 2\%$ ion polarimetry is required.

5. Polarized positron-ion collisions are desirable with a high luminosity.

6. This point is of the most importance for the present dissertation: **The luminosity should range between mid 10^{33} to above 10^{34} $\mathbf{cm^{-2}s^{-1}}$ per interaction point, over a broad energy range**. While the optimisation of the luminosity should be centered around 45 to 50 GeV CM energy ($s \sim 2000$ to 2500 GeV^2)*.

*Further, an EIC design should be flexible enough to allow an option of future energy upgrade up to 20 GeV for the electron beam, 250 GeV for protons and up to 100 GeV per nucleon for ions. [10]

CHAPTER 2

ACCELERATOR PHYSICS AND LINEAR OPTICS

In this chapter we will present a summary of the most relevant concepts related to linear optics, colliders, and the motivation behind the crab crossing scheme to recover luminosity. Section 2.1 will introduce the basic lattice elements and the concept of transport matrices. Then, Section 2.2 will describe what is luminosity, its importance for colliders and the basic machine parameters that affect it. And finally, Section 2.3 will describe the crabbing concept and its two main schemes (global and local) as a preamble for Section 4, where these concepts will be employed and extended.

This section is not intended to be a full bestiary of accelerator physics or a consulting reference, for this, we already have excellent sources like [11, 12, 13] and of course the handbook [14], to mention just a few. Also, there are countless great lecture notes from several particle accelerator schools such as USPAS [15], CAS [16], etc. that serve this purpose. The simple objective of this chapter, is to provide the reader with a quick overview of a subset of accelerator physics concepts, sufficient to understand the subject of this dissertation and highlight the goals and motivations driving its content.

2.1 BASIC ELEMENTS AND TRANSPORT MATRICES

Typically, an accelerator design is based on a basic set of elements—magnets, drift tubes, etc.—that repeats throughout the lattice, with some extra elements here and there—like kickers, accelerating structures, or correctors. We call this basic set of elements a **cell** and it is in a way, like our LEGO® block. A cell is designed to ensure that a beam passing through it, will exit with a proper distribution, given the distribution at the entrance of the cell. These cells could be periodic or not, depending on their function and the nature of the machine.

Particle accelerators come in two basic flavours, linear and circular machines. A linear machine is that on which the particles pass through each element only once, while in a circular accelerator, the same bunch particles will go through every element numerous times. In this work, we will develop concepts and technology that could be employed in any collider, being it linear or circular, as long as it requires high luminosity performance. However, we explore a particular application of these [crabbing] systems for a circular electron-ion collider. Setting specific goals will help us to explore the parameter space of the proposed rf structure, in order to understand the correlations between geometry and performance, as well as to study some of the effects on the beam dynamics derived from them. For this reason, we will employ the nomenclature and definitions commonly used in circular machines, but, making the remark that one should be careful when consulting different sources, if they are talking about linear or circular, for leptons or hadrons machines, since all of them carry their own *slang*, even when the function that relates them is bijective, it can be a bit confusing. The historical difficulty to standardise the terminology and definitions in acceleration physics, seems to be a time invariant.

2.1.1 LORENTZ FORCE AND MOVING COORDINATES

It is in the basics of classical electromagnetism that we find our *war-horse*, since many important concepts are derived from the definition of the electromagnetic force, better known as the Lorentz force:

$$\vec{F} = q\left(\vec{E} + \vec{v} \times \vec{B}\right), \tag{1}$$

where q is the charge, $\vec{E}$ an external applied electric field, $\vec{v}$ the particle's velocity, and $\vec{B}$ an external applied magnetic field. Equation 1 gives us already a great deal of information, such as that to accelerate a particle, we need to apply an electric field in the direction that we want to accelerate, meanwhile in order to deflect or bend the particle, we need to apply a magnetic field perpendicular to both the direction of the particle's momentum and the direction of the desired bend. Obviously, this only works for charged particles since if $q = 0$, then the Lorentz force will also be null.

Now, if we imagine a single particle of charge q, moving with constant velocity $\vec{v}$ perpendicular to a constant field $\vec{B}$, then the particle will describe a circular orbit of radius ρ, as illustrated in Fig. 1.

Then, we can remember from classical mechanics that the necessary force to constrain the particle to this circular orbit, can be derived as follows:

$$\begin{aligned} |\vec{a}| &= \frac{|\vec{v}|^2}{\rho}, \\ \Rightarrow F &= ma = \frac{mv^2}{\rho} \end{aligned} \tag{2}$$

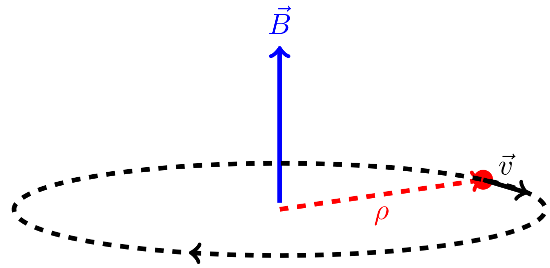

FIG. 1: Charged particle describing a circular orbit, due to a perpendicular constant magnetic field $\vec{B}$.

and using Eq. 2, Fig. 1, and the definition of the Lorentz force in absence of electric fields, with a constant magnetic field $\vec{B}$, then $\dot{\gamma} = 0$, then we can write:

$$\begin{aligned} F &= qvB = \dot{p} = \frac{\gamma m v^2}{\rho}, \\ \Rightarrow B\rho &= \frac{\gamma m v}{q}, \\ \therefore B\rho &= \frac{p}{q}, \end{aligned} \tag{3}$$

with p as the relativistic linear momentum of the particle. Equation 3 is called **Rigidity** and relates parameters of the lattice—in the l.h.s.—as the field B from the magnets and the radius ρ of the design orbit, with beam parameters—in the r.h.s.—as the momentum p of the particles and their electrical charge q. The rigidity is a very important and handy quantity when dealing with beam dynamics and lattice design.

Now, let's look again at Fig. 1 and set a coordinate system moving on the particles reference frame (see Fig. 2), where we set the longitudinal coordinate around the design orbit as $s = \rho\theta$ and the horizontal coordinate as $x = R - \rho$. However, we already mentioned that this circular orbit (which is typically called *design orbit* or *golden particle's orbit*), derives from the Lorentz force $\vec{F_0} = q\vec{v_0} \times \vec{B}$.

What happens then if there is a second particle with the same charge but with a velocity $\vec{v_i}$ pointing out at a slightly different angle than the original one? Well, then the bending force exerted onto this other particle will be pointing out in a slightly different position $\vec{F_i} = q\vec{v_i} \times \vec{B}$ and if the angle difference between the velocities is small, then the orbit will also be slightly different (see Fig. 3).

If we plot the horizontal displacement of both particles, as a function of the angle θ along s, we see a sinusoidal oscillation of the second particle's orbit with respect to

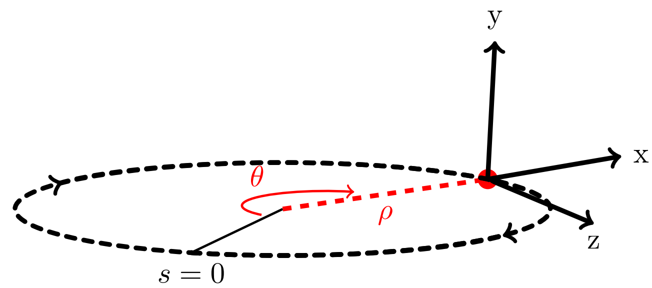

FIG. 2: Coordinate systems and reference orbit used for the equations of motion.

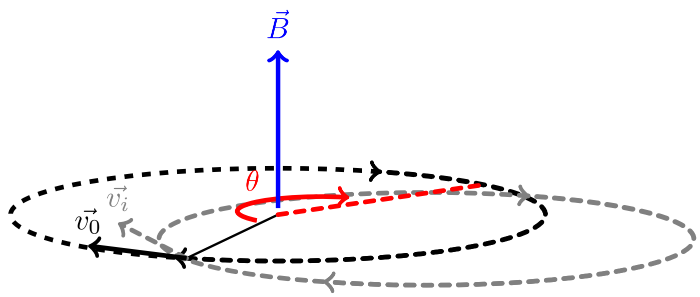

FIG. 3: Orbits of two particles with different initial angle in an external dipole field.

the design orbit, as shown in Fig. 4. This transverse oscillations are called **betatron oscillations** and analogous to the horizontal plane, there is also a betatron motion in y, typically the two of them are completely independent, as long as they are not *skewed* elements or other mechanisms to couple them—some of these cases will be discussed in Section 4.4.

The number of oscillations performed for a particle in the horizontal (x) or vertical (y) plane is accounted by a quantity named the **betatron tune** $Q_{x,y}$ where:

$$Q_{x,y} = \frac{\#\text{ of betatron oscillations in } x, y}{\#\text{ of turns}} = \frac{\text{phase advance per turn}}{2\pi} \tag{4}$$

and the condition for strong focusing is given by:

$$Q > 1.$$

Commonly, we use the **fractional betatron tunes**, denoted $\nu_{x,y}$, since the integer parts of the tune do not give meaningful information as the fractional part does. For example, if we have a tune of $Q_x = 3.16$, its fractional tune is said to be $\nu_x = 0.16$, after leaving out the integer part.

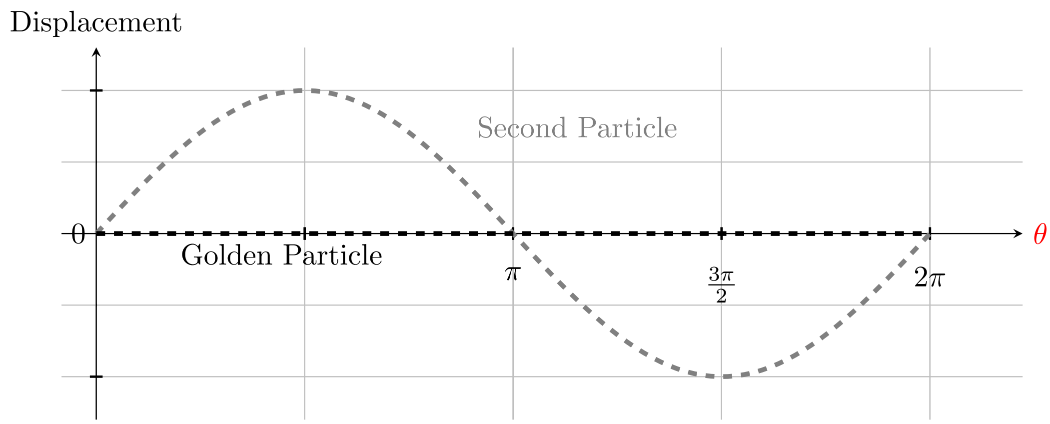

FIG. 4: Transverse oscillation of a second particle around the design orbit, showing an integer tune (only if there is focusing by bending).

2.1.2 MAGNETS

Next, we will employ magnetic fields in accelerators to deflect (dipoles), focus (quadrupoles), or correct higher order effects (sextupoles, octupoles, etc.). For this we will come back to Eq. 1 in absence of external electric fields: $\vec{F} = q\vec{v} \times \vec{B}$ and Maxwell's equations in vacuum and without free currents or external electric fields,

$$\vec{\nabla} \cdot \vec{B} = 0, \tag{5}$$

$$\vec{\nabla} \times \vec{B} = 0. \tag{6}$$

We then obtain—in the 2D model—from Eq. 5 and 6, respectively,

$$\frac{\partial B_x}{\partial x} + \frac{\partial B_y}{\partial y} = 0, \tag{7}$$

$$\frac{\partial B_x}{\partial y} = \frac{\partial B_y}{\partial x}. \tag{8}$$

Using cylindrical coordinates ($x = r\cos\theta$ and $y = r\sin\theta$), we can expand the magnetic fields in a series of multipoles, with respect to a reference radius a (typically of the order of $\frac{2}{3}$ the radius of the beam pipe), as follows:

$$B_y = B_0 \sum_{n=0}^{\infty} \left(\frac{r}{a}\right)^n \left(b_n \cos(n\theta) - a_n \sin(n\theta)\right), \tag{9}$$

$$B_x = B_0 \sum_{n=0}^{\infty} \left(\frac{r}{a}\right)^n \left(a_n \cos(n\theta) + b_n \sin(n\theta)\right), \tag{10}$$

with B_0 as the central field, and rearranging the equation back to Cartesian notation we have

$$B_x - iB_y = B_0 \sum_{n=0}^{\infty} (a_n - ib_n) \left(\frac{x+iy}{a} \right)^n . \tag{11}$$

We call the coefficients b_n in Eq. 11 the *normal* $2\,(n+1)$-pole coefficients, while the a_n are the *skew* $2\,(n+1)$-pole coefficients. Therefore, a magnet with $b_0 = 1$ and $b_n = 0$ for all $n \neq 0$, as well as $a_n = 0$ for all n, is called a *normal dipole*. In the same way, for a magnet which only non-zero element is $b_1 = 1$, we call it a *normal quadrupole* and so on [12]. Figure 5 shows the schematic cross section of a normal dipole (a) and a normal quadrupole (b). Strictly speaking, the $\vec{B}$ field lines should be shown closing into themselves (since $\vec{\nabla} \cdot \vec{B} = 0$), however, Fig. 5 is just a simplified conceptual image, intended to show the deflecting principles of dipoles (a) and quadrupoles (b).

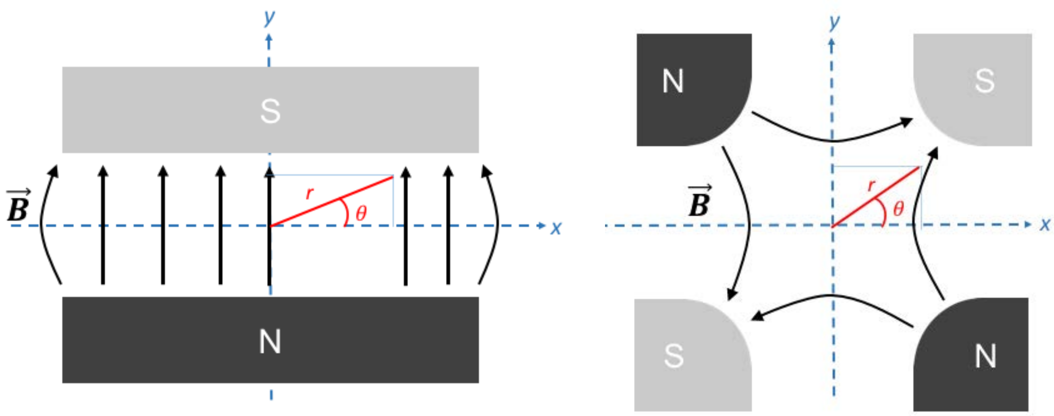

(a) Dipole (b) Quadrupole

FIG. 5: Pole profile of two different bending magnets.

Normal dipoles (without focusing) are very important in circular machines, since they provide the bending guidance for the particle to stay in orbit around the machine. Also, dipoles are greatly used as *momentum selectors* in many detectors, since they can separate particles with different rigidities. Equation 11 for $b_0 = 1$, as the only non zero element of the expansion, reduces to Eq. 12 for a pure dipole with focusing in the bend plane and without fringe fields.

$$\vec{B} = B_0 \hat{y}. \tag{12}$$

Quadrupoles, on the other hand, are used in all accelerators as *lenses*—by analogy with optics—due to the fact that they can focus/defocus the beam in the transverse direction of its motion, since a charged particle traveling through the magnet will see a force pushing it towards the center in one transverse plane and pulling it outwards in the other, shown in Fig. 6 with red arrows. Again, the field expansion for a normal quadrupole is described by Eq. 13.

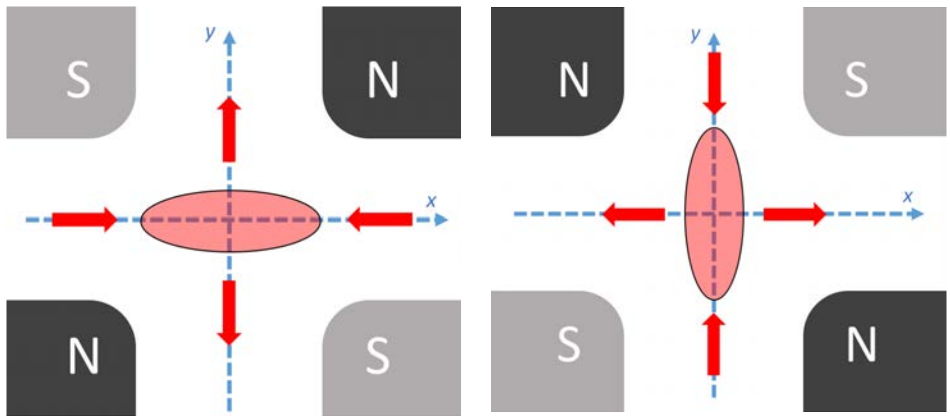

(a) $Q_{F,x}$ or $Q_{D,y}$ (b) $Q_{D,x}$ or $Q_{F,y}$

FIG. 6: Focusing/defocusing force due to one quadrupole (a) and another identical quadrupole rotated by 90° (b), for a charged particle traveling "*into the page*".

$$\vec{B} = (x\hat{y} + y\hat{x}) \left(\frac{\partial B_y}{\partial x} \right). \tag{13}$$

It is very important to remember that a focusing quadrupole Q_F in one plane, will always be a defocusing quadrupole Q_D in the perpendicular plane. This becomes useful under the concept of *strong focusing* (see Section 2.1.4 bellow). Also, in the present work, we will focus on up to the sextupole ($n = 2$) component of the expansion, due to its effects on the beam emittance and more importantly, due to the fact that the sextupole magnets are typically the most important *non-linear* contribution to the beam dynamics in synchrotron lattices.

2.1.3 SINGLE ELEMENT OPTICS

Using K.L. Brown approach [14], we can track a charged particle at any position s with respect to the reference trajectory by a column vector $\mathbf{X}^t(s) = (x(s), x'(s), y(s), y'(s), z(s), \Delta P/P_0)$, where x and y are the horizontal and vertical displacements with respect to the trajectory of the golden particle, as shown in Fig. 4, $x' = dx/ds$ and $y' = dy/ds$ are the angle of the particle's trajectory with respect to the horizontal and vertical plane, respectively, z is the path difference between the particle's trajectory and the design trajectory, measured from $s = 0$ and $\Delta P/P_0$ is the momentum deviation with respect to the golden particle. Then, the golden particle's trajectory is defined by $\mathbf{X}(0) = \mathbf{0}$. If we imagine a particle at a position $s = s_0$ going through a magnet—as the ones described in Fig. 5—with $\mathbf{X}(s_0)$ and coming out from it at $s = s_1$ with $\mathbf{X}(s_1)$, we can define a transformation $\mathbb{M}\left(s_0 \rightarrow s_1\right)$ for this magnet, such as:

$$\mathbf{X}\left(s_1\right) = \mathbb{M}\left(s_0 \rightarrow s_1\right) \mathbf{X}\left(s_0\right). \tag{14}$$

This 6×6 matrix $\mathbb{M}$ contains all the physics of every single element—being this a dipole, drift, rf cavity, etc.—derived from the equations of motion for a charged particle passing through it. Being able to define a linear transformation such as this for every element of the accelerator, is enormously convenient, since they follow superposition. Therefore, for a particle going from s_0 to s_n and passing throughout n number of elements, we can define a single **total** transfer matrix $\mathbb{M}_{\text{Total}}$ as a product of every *single element* transverse matrices, following:

$$\begin{aligned}
\mathbb{M}_{\text{Total}} &= \mathbb{M}\left(s_{n-1} \rightarrow s_n\right) \cdots \mathbb{M}\left(s_{i-1} \rightarrow s_i\right) \cdots \mathbb{M}\left(s_2 \rightarrow s_1\right) \mathbb{M}\left(s_1 \rightarrow s_0\right), \\
\mathbf{X}\left(s_n\right) &= \mathbb{M}_{\text{Total}} \mathbf{X}\left(s_0\right).
\end{aligned} \tag{15}$$

This can be extended to non-linear terms as well [17]. There are also other properties that these single element transfer matrices need to comply with, like unitarity ($\mathbf{det}\mathbb{M} = 1$), or the fact that in static magnetic fields $\Delta P/P_0$ is a constant of motion and independent of $z\left(s\right)$. Then, we can expand Eq. 14 taking this into account, as shown in Eq. 16.

$$\begin{pmatrix} x\left(s_1\right) \\ x'\left(s_1\right) \\ y\left(s_1\right) \\ y'\left(s_1\right) \\ z\left(s_1\right) \\ \Delta P/P_0 \end{pmatrix} = \begin{pmatrix} m_{11} & m_{12} & 0 & 0 & 0 & m_{16} \\ m_{21} & m_{22} & 0 & 0 & 0 & m_{26} \\ 0 & 0 & m_{33} & m_{34} & 0 & 0 \\ 0 & 0 & m_{43} & m_{44} & 0 & 0 \\ m_{51} & m_{52} & 0 & 0 & 1 & m_{56} \\ 0 & 0 & 0 & 0 & 0 & 1 \end{pmatrix} \begin{pmatrix} x\left(s_0\right) \\ x'\left(s_0\right) \\ y\left(s_0\right) \\ y'\left(s_0\right) \\ z\left(s_0\right) \\ \Delta P/P_0 \end{pmatrix}. \tag{16}$$

A **drift** can be considered a *particular* case of a "magnet" without field. Therefore, the only effect it has on the particles is that it will allow the transverse coordinates x and y to evolve though the drift length L by their respective angle x' or y'.

Or in other words, the particle's equations of motion, when going through a drift, is described by Eq. 14 with a transfer matrix described as:

$$\mathbb{M}_{\text{Drift}} \equiv \begin{pmatrix} 1 & \mathrm{L} & 0 & 0 & 0 & 0 \\ 0 & 1 & 0 & 0 & 0 & 0 \\ 0 & 0 & 1 & \mathrm{L} & 0 & 0 \\ 0 & 0 & 0 & 1 & 0 & 0 \\ 0 & 0 & 0 & 0 & 1 & \frac{L}{\gamma} \\ 0 & 0 & 0 & 0 & 0 & 1 \end{pmatrix}, \tag{17}$$

where $\frac{L}{\gamma} \to 0$ in the ultrarelativistic approximation.

A **dipole** without focusing, typically produces a horizontal bending of angle θ_d (see Fig. 7) and represents a drift of length $\rho\theta_d$—for small θ_d-s—in the vertical direction. The corresponding transfer matrix is shown in Eq. 18—without considering dispersion.

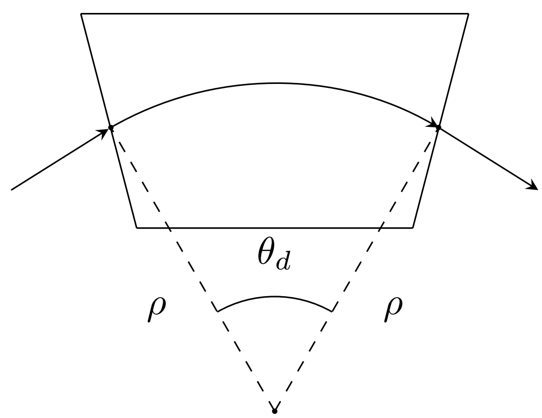

FIG. 7: Change in orbit due to a dipole (sector magnet) to a particle with a fixed momentum.

$$\mathbb{M}_{\text{Dipole}} \equiv \begin{pmatrix} \cos\theta_d & \rho\sin\theta_d & 0 & 0 & 0 & 0 \\ -\frac{1}{\rho}\sin\theta_d & \cos\theta_d & 0 & 0 & 0 & 0 \\ 0 & 0 & 1 & \rho\theta_d & 0 & 0 \\ 0 & 0 & 0 & 1 & 0 & 0 \\ 0 & 0 & 0 & 0 & 1 & 0 \\ 0 & 0 & 0 & 0 & 0 & 1 \end{pmatrix}. \tag{18}$$

For the **quadrupoles** and following Eq. 13—with $B_x \equiv yG$ and $B_y \equiv xG$—then the quadrupole gradient is $G \approx \frac{\partial B_y}{\partial x}$. Then the corresponding horizontal and vertical forces are:

$$\begin{aligned} F_x &= -q\beta_{\text{rel}} c G y\,, \quad \text{and} \\ F_y &= q\beta_{\text{rel}} c G x\,, \end{aligned}$$

with $\beta_{rel}c = v$ the particles velocity in s-direction. Leading to the equations of motion:

$$\frac{d^2x}{ds^2} + kx = 0\,, \tag{19}$$

$$\frac{d^2y}{ds^2} - ky = 0\,, \tag{20}$$

where $s = \beta_{rel}ct$ and $k \equiv \frac{G}{B\rho}$. Then, the horizontal equation of motion is that of a harmonic oscillator—with solutions of sin and cos, while the solution to Eq. 20 is given by cosh and sinh, obtaining then the *thick lens* transfer matrix for the quadrupoles.

$$\mathbb{M}_{\text{Quad}} \equiv \begin{pmatrix} \cos\left(\sqrt{k}l\right) & \frac{1}{\sqrt{k}}\sin\left(\sqrt{k}l\right) & 0 & 0 & 0 & 0 \\ \mp\sqrt{k}\sin\left(\sqrt{k}l\right) & \cos\left(\sqrt{k}l\right) & 0 & 0 & 0 & 0 \\ 0 & 0 & \cosh\left(\sqrt{k}l\right) & \frac{1}{\sqrt{k}}\sinh\left(\sqrt{k}l\right) & 0 & 0 \\ 0 & 0 & \pm\sqrt{k}\sinh\left(\sqrt{k}l\right) & \cosh\left(\sqrt{k}l\right) & 0 & 0 \\ 0 & 0 & 0 & 0 & 1 & 0 \\ 0 & 0 & 0 & 0 & 0 & 1 \end{pmatrix},$$

where l is the length of the quad and the top signs correspond to a quadrupole focusing in x and defocusing in y, while the bottom signs are for a quadrupole defocusing in x and focusing in y. The *thin lens* approximation correspond to $\sqrt{k}l =$ constant $\ll 1$ when $l \to 0$ and, therefore, the above matrix reduces to:

$$\mathbb{M}_{\text{Quad}} \equiv \begin{pmatrix} 1 & 0 & 0 & 0 & 0 & 0 \\ \mp\frac{1}{F} & 1 & 0 & 0 & 0 & 0 \\ 0 & 0 & 1 & 0 & 0 & 0 \\ 0 & 0 & \pm\frac{1}{F} & 1 & 0 & 0 \\ 0 & 0 & 0 & 0 & 1 & 0 \\ 0 & 0 & 0 & 0 & 0 & 1 \end{pmatrix}, \tag{21}$$

with $kl = \frac{1}{F}$ and F is the focal length of the quadrupole. It is important to remember that the *thin lens* approximation is a reasonable approximation, as long as $|F| \gg l$.

2.1.4 STRONG FOCUSING

Having described our basic elements in their simpler representation, now we can start looking at what we can do when combining them, in particular when we alternate focusing (F) or defocusing (D) quadrupoles, also know as **doublets**. Figure 8 shows an optical system with alternating focusing and defocusing gradients.

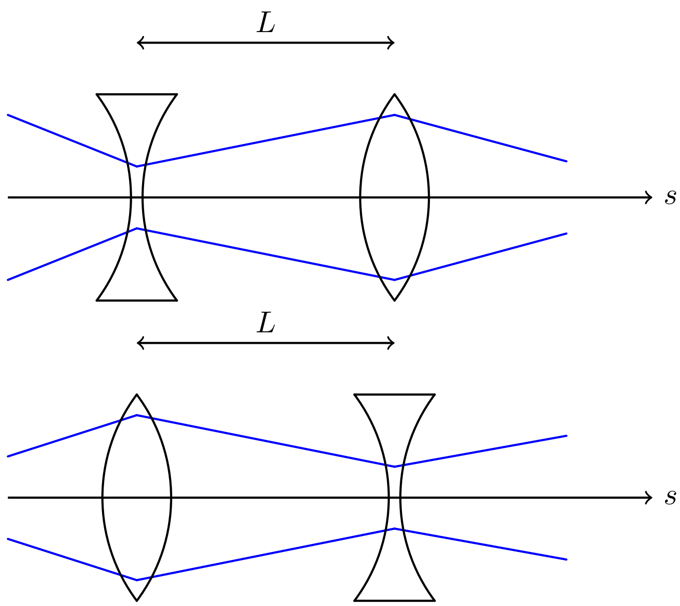

FIG. 8: Alternating gradients systems: F-D (top) and D-F (bottom).

Assuming that both focusing and defocusing quadrupoles in Fig. 8 have the same focal length F, then the 2D transfer matrix of the systems can be calculated as:

$$\mathbb{M}_{\text{doublet}} = \begin{pmatrix} 1 & 0 \\ \pm\frac{1}{F} & 1 \end{pmatrix} \begin{pmatrix} 1 & L \\ 0 & 1 \end{pmatrix} \begin{pmatrix} 1 & 0 \\ \mp\frac{1}{F} & 1 \end{pmatrix} = \begin{pmatrix} 1 \mp \frac{L}{F} & L \\ -\frac{L}{F^2} & 1 \pm \frac{L}{F} \end{pmatrix}. \tag{22}$$

The element m_{21} in Eq. 22 gives the inverse of the effective focal length of the system and its negative sign proves that the alternating gradient provides a net focusing effect, this is the base of the so called **strong focusing**. This idea has been patented since March of 1950 by Nicholas Christofilos (US Patent No. 2,736,799) and is used as one of the building blocks of most of the modern accelerators.

We could make a small parenthesis at this point—before moving towards the description of lattices—to discuss some of the figures of merit used in accelerator physics. To start with, we already talked about the momentum deviation in Section 2.1.3, typically we assign to it the symbol δ, where $\delta \ll 1$.

Now, generalising Eq. 19 and 20, using Eq. 11, we can rewrite the equations of motion in the transverse plane—called **Hill's equations**—for an array of magnets, with a periodic function of the coordinate s and period C, in other words $k_{x/y}(s+C) = k_{x/y}(s)$, then:

$$\begin{aligned} x'' + k_x(s)x &= 0, & (23) \\ y'' - k_y(s)y &= 0. & (24) \end{aligned}$$

The period C could be an entire revolution around the machine, or the length of one repeated cell. For the case of the horizontal plane (i.e. Eq. 23), we use the ansatz of a *quasi-periodic harmonic oscillator*, with an amplitude $w(s)$ that is periodic in C.

$$x(s) = Aw(s)\cos\left[\psi_x(s) + \psi_0\right]. \tag{25}$$

It is important to highlight that $\psi_x(s)$ in Eq. 25 is not periodic. Then, substituting in Eqn.23 the appropriate derivatives of $x(s)$ we obtain:

$$A(w'' - w\psi_x'^2 + k_x w)\cos\left[\psi_x + \psi_0\right] - A(2w'\psi_x' + w\psi_x'')\sin\left[\psi_x + \psi_0\right] = 0, \tag{26}$$

where both the sin and cos coefficients should vanish identically, since both w and ψ_x do not depend on ψ_0. Then—and losing the subindex for x from the nomenclature for simplicity—we have:

$$\begin{aligned} w'' - w\psi'^2 + kw &= 0, & (27) \\ 2w'\psi' + w\psi'' &= 0. & (28) \end{aligned}$$

From Eq. 28 we find the $\psi' = \frac{\kappa}{w^2(s)}$, where κ is a constant. With this and Eq. 27, we obtain that:

$$w^3(w'' + kw) = \kappa^2. \tag{29}$$

Next, we introduce a new set of functions called **Twiss functions** or **Courant-Snyder parameters**, $\beta(s)$, $\alpha(s)$, and $\gamma(s)$, such as:

$$\beta(s) \equiv \frac{w^2(s)}{\kappa}, \tag{30}$$

$$\alpha(s) \equiv -\frac{1}{2}\beta'(s), \tag{31}$$

$$\gamma(s) \equiv \frac{1 + \alpha^2(s)}{\beta(s)}. \tag{32}$$

Using the Twiss functions and Eq. 28, we can rewrite the phase advance as:

$$\psi(s) = \int_s \frac{d\tau}{\beta(\tau)}, \tag{33}$$

and we define as the **betatron** phase advance as:

$$\psi_C = \psi(C) = \int_{s_0}^{s_0+C} \frac{d\tau}{\beta(\tau)}. \tag{34}$$

Then, for Eq. 29, we can express in terms of the Twiss:

$$k\beta = \gamma + \alpha'. \tag{35}$$

Again, it is important to remember that $\beta(s)$, $\alpha(s)$, and $\gamma(s)$ are periodic in C, while $\psi(s)$ is not. We can express then Eq. 25 as:

$$x(s) = A\sqrt{\beta(s)}\cos\psi(s) + B\sqrt{\beta(s)}\sin\psi(s), \tag{36}$$

with $\pm\sqrt{\beta(s)}$ describing the envelope for the beam's transverse oscillations, then:

$$x'(s) = \frac{1}{\sqrt{\beta(s)}}\left\{[B - \alpha(s)A]\cos\psi(s) - [A + \alpha(s)B]\sin\psi(s)\right\}, \tag{37}$$

comparing with the initial conditions (x_0, x_0'), as a result, the constants A and B can be expressed like:

$$\begin{aligned} A &= \frac{x_0}{\sqrt{\beta(s)}}, \\ B &= \frac{1}{\sqrt{\beta(s)}}[\beta(s)x_0'' + \alpha(s)x_0]. \end{aligned}$$

We can now write the transport matrix $\mathbb{M}_C$ of the periodic system as:

$$\begin{pmatrix} x \\ x' \end{pmatrix}_{s_0+C} = \begin{pmatrix} \cos\psi_C + \alpha\sin\psi_C & \beta\sin\psi_C \\ -\gamma\sin\psi_C & \cos\psi_C - \alpha\sin\psi_C \end{pmatrix} \begin{pmatrix} x \\ x' \end{pmatrix}_{s_0}. \tag{38}$$

A transport matrix of a periodic system is always unimodular $det\left\{\mathbb{M}_C\right\} = 1$ and it can be written as:

$$\begin{aligned} \mathbb{M}_C &= \mathbb{I}\cos\psi_C + \mathbb{J}\sin\psi_C, \qquad (39) \\ \text{where} \quad \mathbb{I} &= \begin{pmatrix} 1 & 0 \\ 0 & 1 \end{pmatrix}, \\ \text{and} \quad \mathbb{J} &= \begin{pmatrix} \alpha(s) & \beta(s) \\ -\gamma(s) & -\alpha(s) \end{pmatrix}, \end{aligned}$$

and finally, since $\mathbb{J}^2 = -\mathbb{I}$, the matrix can be also written as $\mathbb{M}_C = e^{\mathbb{J}(s)\psi_C}$ and thus, the transfer matrix, after **n** turns in a periodic system, is just $\mathbb{M}_C^n$, or:

$$\begin{pmatrix} x \\ x' \end{pmatrix} = \mathbb{M}_C^n \begin{pmatrix} x_0 \\ x'_0 \end{pmatrix}. \tag{40}$$

We have described most of the concepts used in this work and there is a fair question one may ask while reading about periodic systems and their transfer matrices, namely: *What happens with non-periodic systems then?* To answer this question, we can write down the transfer matrix $\mathbb{M}_{s,s_0}$ associated to a non-periodic system between two locations, s_0 and s in the machine.

$$\mathbb{M}_{s,s_0} \equiv \begin{pmatrix} \sqrt{\frac{\beta(s)}{\beta(s_0)}}\left[\cos\Delta\psi + \alpha(s_0)\sin\Delta\psi\right] & \sqrt{\beta(s_0)\beta(s)}\sin\Delta\psi \\ -\frac{[\alpha(s)-\alpha(s_0)]\cos\Delta\psi + [1+\alpha(s_0)\alpha(s)]\sin\Delta\psi}{\sqrt{\beta(s_0)\beta(s)}} & \sqrt{\frac{\beta(s)}{\beta(s_0)}}\left[\cos\Delta\psi - \alpha(s_0)\sin\Delta\psi\right] \end{pmatrix}$$

and notice that after one turn it reduces to the transfer matrix of a periodic system.

$$\mathbb{M}_{s_0+C,s_0} \equiv \begin{pmatrix} \cos\mu + \alpha(s_0)\sin\mu & \beta(s_0)\sin\mu \\ -\gamma(s_0)\sin\mu & \cos\mu - \alpha(s_0)\sin\mu \end{pmatrix},$$

where μ is the phase advance accumulated after one turn, also this follows Eq. 38 and 39. Thus, we can write the matrix elements m_{ij} for the transfer matrix, following

$$\begin{pmatrix} x \\ x' \end{pmatrix}_s = \begin{pmatrix} m_{11} & m_{12} \\ m_{21} & m_{22} \end{pmatrix} \begin{pmatrix} x_0 \\ x'_0 \end{pmatrix},$$

as

$$\begin{aligned} m_{11} &= \frac{w(s)}{w_0}\cos\Delta\psi - w(s)w'_0\sin\Delta\psi, & (41) \\ m_{12} &= w(s)w_0\sin\Delta\psi, & (42) \\ m_{21} &= \frac{1 + w(s)w_0w'(s)w'_0}{w(s)w_0}\sin\Delta\psi - \left[\frac{w'_0}{w(s)} - \frac{w'(s)}{w_0}\right]\cos\Delta\psi, & (43) \\ m_{22} &= \frac{w_0}{w(s)}\cos\Delta\psi - w_0w'(s)\sin\Delta\psi. & (44) \end{aligned}$$

All this is very helpful, since if we know the Twiss parameters at any point s_0, we can transport them to any other point s of the machine as follows:

$$\begin{pmatrix} \beta(s) \\ \alpha(s) \\ \gamma(s) \end{pmatrix} = \begin{pmatrix} m_{11}^2 & -2m_{11}m_{12} & m_{12}^2 \\ -m_{11}m_{21} & m_{11}m_{22} + m_{12}m_{21} & -m_{12}m_{22} \\ m_{21}^2 & -2m_{21}m_{22} & m_{22}^2 \end{pmatrix} \begin{pmatrix} \beta(s_0) \\ \alpha(s_0) \\ \gamma(s_0) \end{pmatrix}. \tag{45}$$

2.1.5 FODO LATTICES

Now we can start describing some periodic systems, specifically periodic cells. The standard FODO cell is composed by a doublet of opposite-strength quadrupoles (F and D) separated by drifts (O), or F-O-D-O. Commonly, the periodic structure is separated as: a focusing half quadrupole F/2 followed by a drift O, a full defocusing quadrupole D, a second drift O, and finally a second focusing half-quadrupole F/2. Figure 9 shows the schematics of such cell. An equivalent version for a circular machine will include bending magnets between the quadrupoles, these will introduce a small—but not negligible—focusing in the bending plane, which is not included in Eq. 46. The beam envelopes are sketched with blue lines.

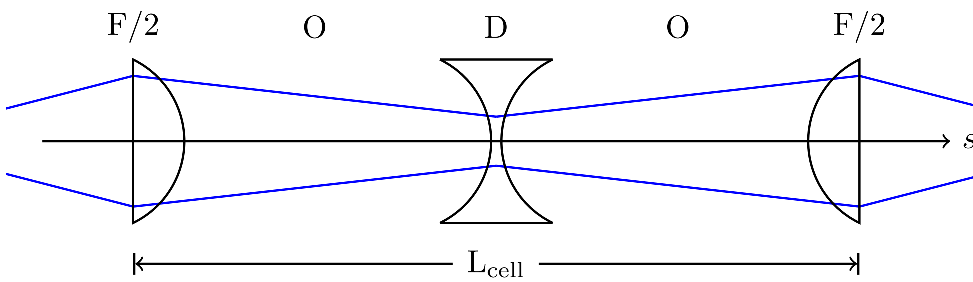

FIG. 9: Schematic of a FODO cell.

Also, we should remember that a FODO cell in one of the transverse coordinates, will look as a DOFO cell in the other transverse coordinate. Therefore, if we consider the cell in the top of Fig. 9 as being in the x-direction, then its transfer matrix would be:

$$\mathbb{M}_{\mathrm{FODO}\binom{x}{y}} \equiv \begin{pmatrix} 1-\frac{L_{\mathrm{cell}}^2}{8F^2} & L_{\mathrm{cell}} \pm \frac{L_{\mathrm{cell}}^2}{4F} \\ \pm\frac{L_{\mathrm{cell}}^2}{16F^3} - \frac{L_{\mathrm{cell}}}{4F^2} & 1-\frac{L_{\mathrm{cell}}^2}{8F^2} \end{pmatrix} \tag{46}$$

and the trace of both matrices (x and y) are:

$$\mathrm{Tr}\left\{\mathbb{M}_{\mathrm{FODO}}\right\} = 2 - \frac{L_{\mathrm{cell}}^2}{4F^2} = 2\cos\left(\psi\right), \tag{47}$$

so we can write the phase advance in a FODO cell as:

$$\psi_{\mathrm{FODO}} = 2\arcsin\left(\pm\frac{L}{4F}\right), \tag{48}$$

with $F > \frac{L}{4}$ as the condition for the phase advance to be real.

The maximum ($^+$) and minimum ($^-$) values of $\beta(s)$—corresponding to $\alpha = 0$—for a FODO cell are located in the center of the focusing and defocusing quadrupoles, respectively. Then, looking at the m_{12} term in Eq. 46 and substituting by ψ from Eq. 48, we find:

$$\beta^{\pm} = \frac{L}{\sin\psi_C}\left(1 \pm \sin\frac{\psi_C}{2}\right). \tag{49}$$

So far, we have always left the dispersion out of all our element's matrices, but the dispersion is an effect that becomes important for a set of particles with a certain momentum distribution in the presence of bending dipoles. The linear dispersion describes how position changes with momentum, or:

$$\eta \equiv dx/d\delta. \tag{50}$$

In the case of a FODO lattice as described in Fig. 9 (bottom), we can express the maximum and minimum dispersion—considering each dipole with length $L_{\text{cell}}/2$—as:

$$\eta_x^{\pm} = \frac{L\theta_d}{4}\left(\frac{1 \pm \frac{1}{2}\sin\frac{\Delta\psi}{2}}{\sin^2\frac{\Delta\psi}{2}}\right). \tag{51}$$

2.1.6 OTHER LATTICES AND INSERTIONS

Up to now, we have spent most of the time leaving the dispersion out of the equations, for simplicity. In the case of the local crab correction—which is ultimately the subject of this dissertation, and will be described in more detail in the following sections—ideally the crab cavities ought to be placed at *zero dispersion* locations in the machine. This is mainly due to the fact that the local crab correction scheme requires the exact cancelation by one crab cavity, of the effects given to the beam by another crab cavity, each placed at opposite sides of the interaction point. For these effects to be cancelled exactly, the energy change due to the beam-beam interaction needs to be cancelled by these two cavities as well, and that does not happen if the dispersion η and its derivative η' do not vanish at the cavities' location [18].

A machine made solely by periodic FODO-like cells, would most likely have non-zero dispersion in the locations we need to place the crab cavities. We then need a special cell or **insertion** to suppress the dispersion at these locations, redundantly, this kind of insertion is called a **dispersion suppressor**. A dispersion suppressor is made by two different FODO lattices, one next to each other (see Fig. 10), that follow the condition:

$$\theta_1 = \left(1 - \frac{1}{4\sin^2\frac{\mu_{\rm cell}}{2}}\right)\theta, \tag{52}$$

$$\theta_2 = \left(\frac{1}{4\sin^2\frac{\mu_{\rm cell}}{2}}\right)\theta, \tag{53}$$

$$\theta = \theta_1 + \theta_2, \tag{54}$$

where $\mu_{\rm cell}$ is the phase advance per cell.

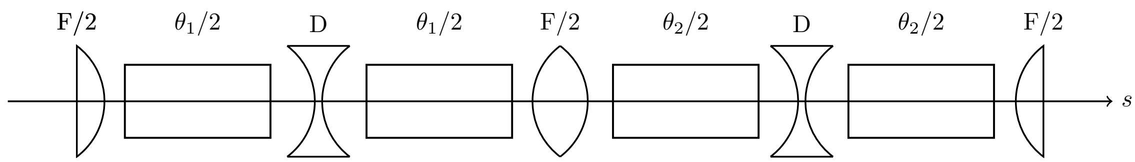

FIG. 10: General schematic of a dispersion suppressor insertion.

Now, let's take the particular case of $\mu_{\rm cell} = \pi/3$, then $4\sin^2\frac{\mu_{\rm cell}}{2} = 1$, so we obtain the insertion called **missing magnet dispersion suppressor**, considering that from Eq. 52 and 53 we have:

$$\theta_1 = 0,$$
$$\theta_2 = \theta.$$

We will not directly treat the dispersion suppressors in the lattice of the electron-ion collider, for which we will be analysing the crabbing systems in this work, but it is important to mention that such insertions in the design are the ones that allow us to treat the location of our cavities as dispersion free. Other insertion, that we will find in the interaction region of all the modern colliders, is called the **low beta** insertion. This insertion reduces the beta functions of the beams with the help of families of quadrupoles called **triplets**, in our particular design, we call these sets of powerful quadrupoles as the **final focusing blocks**. The main goal of the crabbing systems is to increase the luminosity of the machine. Making the beams smaller is one mechanism to achieve this. For the moment, we will not delve deeper in the description of the low beta insertions, we will only show the expression of the beta functions in such insertions and, in fact, any field-free region that contains a minimum beam size (see Eq. 55).

$$\beta(s) = \beta^* + \frac{s^2}{\beta^*}, \tag{55}$$

where β^* is the beta function evaluated at the interaction point in the middle of the insertion and s is the distance from the interaction point (β^*). There will be further discussions of certain complications given by the β^* in the following paragraphs. These are not the only type of insertions, there are double bend achromats, etc. that are very important for the machines but are not relevant for the present work.

2.2 LUMINOSITY

One of the biggest concerns when it comes to collider experiments is achieving a high statistical regime in the analysis of specific physical processes, and since we mainly care about the integrated number of events, we could either increase the running time for the experiment or increase the event rate—number of interactions per second $\left[\frac{dR}{dt}\right]$—where:

$$\frac{dR}{dt} = \mathcal{L} \times \sigma_p \tag{56}$$

and σ_p is the cross section of the specific interaction (erg. Lepton-parton scattering) and $\mathcal{L}$ is the luminosity, which is a relativistic invariant, independent of the interaction, and very important, measurable. We can think as an example the case of the Large Hadron Collider at CERN, where the total cross section for pp is, let's say $\sigma_{pp,\mathrm{tot}} \sim 10^{-25}\,\mathrm{cm}^2$ [19] and the design luminosity of the LHC is $\mathcal{L} = 10^{34}\mathrm{cm}^{-2}\mathrm{s}^{-1}$, then:

$$\left[\frac{dR}{dt}\right]_{pp,\mathrm{LHC}} \sim 10^9 \quad \text{events per second.}$$

For two colliding beams (see Fig. 11), then we have that $\mathcal{L} \propto f n_1 n_2/a$, where f as the bunch frequency, n_1 the number of particles per bunch in the first beam, n_2 the number of particles per bunch in the second beam, and a as the beams transverse profile.

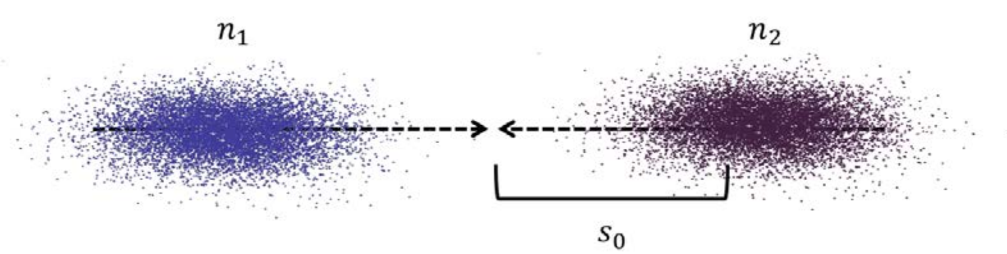

FIG. 11: Gaussian bunch distributions colliding head-on.

Then, we can calculate for each bunch crossing:

$$\mathcal{L} = K n_1 n_2 \iiint_{-\infty}^{\infty} \mathrm{d}x\mathrm{d}y\mathrm{d}s\mathrm{d}s_0 \left[\rho_1\left(x,y,s,-s_0\right)\rho_2\left(x,y,s,s_0\right)\right], \tag{57}$$

where $s_0 = ct$, K is the kinematic factor $K = \sqrt{\left(\vec{v}_1 - \vec{v}_2\right)^2 - \left(\vec{v}_1 \times \vec{v}_2\right)^2/c^2}$, which for head-on collisions (i.e. $\vec{v}_1 = -\vec{v}_2$) reduces to $K = 2$. We will consider for simplicity uncorrelated particle distributions in the bunches, such as:

$$\rho(x,y,s,s_0) = \rho_x(x)\rho_y(y)\rho_s(s \pm s_0). \tag{58}$$

Using this and generalising Eq. 57 to N_b bunches with a bunch repetition rate of f, then:

$$\begin{aligned}\mathcal{L} &= 2Kn_1n_2fN_b \iiint_{-\infty}^{\infty} \mathrm{d}x\mathrm{d}y\mathrm{d}s\mathrm{d}s_0 \times \\ &\quad \left[\rho_{1x}(x)\rho_{1y}(y)\rho_{1s}(s-s_0)\rho_{2x}(x)\rho_{2y}(y)\rho_{2s}(s+s_0)\right] \end{aligned}\tag{59}$$

and

$$\rho_{i,u}(u) = \frac{1}{\sigma_{iu}\sqrt{2\pi}} e^{\left(-\frac{u^2}{2\sigma_{iu}^2}\right)}, \qquad \rho_s(s \pm s_0) = \frac{1}{\sigma_s\sqrt{2\pi}} e^{\left(-\frac{(s\pm s_0)^2}{2\sigma_s^2}\right)}, \tag{60}$$

where u denotes the transverse coordinates x, y, the index i indicates beam 1 or beam 2, and σ_{iu} is the bunch size in the u-dimension. Considering normal distributions is possible as long as we are treating with bunches in equilibrium and is the only way we can perform this calculation analytically, otherwise we require numerical methods.

Now, lets consider the simple case of identical bunches (i.e. $\sigma_{iu} = \sigma_{ju}$), then:

$$\mathcal{L} = \frac{n_1 n_2 f N_b}{4\pi\epsilon\sqrt{\beta_x^*\beta_y^*}} \tag{61}$$

where ϵ is the beams' geometrical emittance, following:

$$\begin{aligned}\sigma_{x,y} &= \sqrt{\epsilon_{x,y}\beta_{x,y}(s)}, &(62)\\ \text{with}\quad \epsilon_{x,y} &= \pi\mathcal{W}_{x,y}, &(63)\\ \text{and}\quad \mathcal{W} &= \gamma x^2 + 2\alpha x x' + \beta x'^2, &(64)\end{aligned}$$

where $\mathcal{W}$ is the **Courant-Snyder Invariant** and represents the area of the ellipse described by the states occupied by the particles of the bunch in the phase space. This volume is invariant under the Liouville's theorem [12].

If we want to go one step further, we can consider small "complications" to the problem, such as beam deformations, non-desired beam offsets, dispersion at the interaction point, strong coupling, and having a crossing angle (we will be back to the latter, since is mostly what concerns the crabbing systems). Then we can write:

$$\mathcal{L} = \frac{n_1 n_2 f N_b}{4\pi\epsilon\sqrt{\beta_x^* \beta_y^*}} \cdot R\left(\theta_c, \epsilon, \beta^*, \sigma_s\right), \tag{65}$$

where we have packed all our contributions to the luminosity degradation in the **reduction factor** $R\left(\theta_c, \epsilon, \beta^*, \sigma_s\right)$.

2.2.1 LUMINOSITY DEGRADATION

We will not spend much time in this dissertation looking into detail at all the mechanisms that contribute to the reducing factor, or simply restrict the luminosity by setting limits (like the tune shift limits given by beam-beam or space-charge effects) [20, 21]. We will simply use as an example of these mechanisms the luminosity degradation due to beam deformations, or the so called **hourglass effect**, and eventually, we will take a more detailed look at the luminosity degradation due to the crossing angle.

In general, the β-functions depend on the position s in the machine. Now, for a field-free region, like near the interaction point—where s is the distance from the interaction point—we can follow:

$$\beta(s) \approx \beta^* \left[1 + \left(\frac{s}{\beta^*}\right)^2\right], \quad \Rightarrow \quad \sigma(s) \approx \sigma^* \left[1 + \left(\frac{s}{\beta^*}\right)^2\right]^{1/2}. \tag{66}$$

For instance, the bunch size is a function of s as well, having a minimum at the interaction point ($s = 0$). Then, when the bunch length is $\sigma_s \geq \beta^*$, the bunch will be deformed at the interaction point (see Fig. 12 [16]), diluting the luminosity following Eq. 67.

$$R_h\left(\beta^*, \sigma_s\right) \equiv \frac{\mathcal{L}(\sigma_s)}{\mathcal{L}(0)} = \sqrt{\pi}\frac{\beta^*}{\sigma_s} e^{\left(\frac{\beta^*}{\sigma_s}\right)^2} \operatorname{erf}\left(\frac{\beta^*}{\sigma_s}\right), \tag{67}$$

which describes the curve shown in Fig. 13 and for example, for the ratio $\beta^*/\sigma_s \approx 1.0$, the luminosity has already been reduced by approximately 25%.

2.2.2 CROSSING ANGLE

Now, let's consider that for reasons like reducing parasitic collisions due to high repetition rate, increasing the detector resolution, or even increasing the physical space for magnets we introduce an angle of collision θ_c between the two beams.

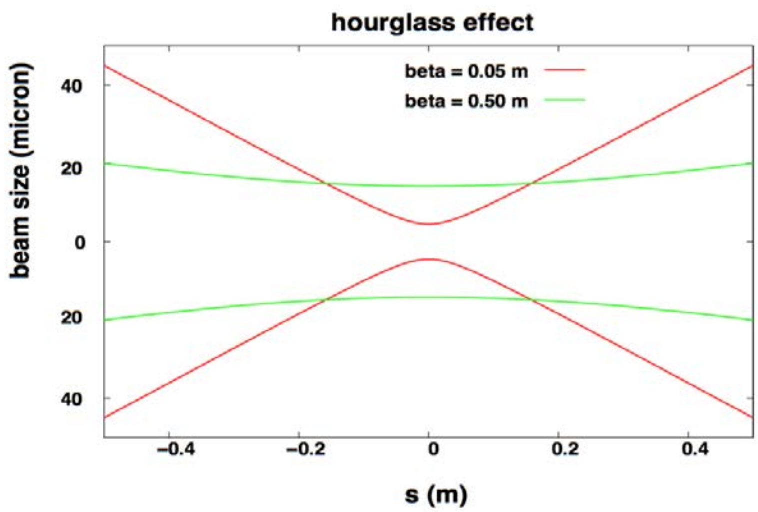

FIG. 12: Graphic description of the beam envelope at the interaction point ($s = 0$) for $\beta^* = 50$ cm (green) and $\beta^* = 5$ cm (red). Image taken from Werner Herr's CAS 2010 lecture.

Fig. 14 shows the particle distributions aligned with trajectories that have a tilt of $\theta_c/2$ with respect to the s-coordinate of the machine. This will effectively reduce the total area of overlap between bunches and, therefore, will reduce the luminosity.

After choosing conveniently two sets of rotated reference frames, aligned each with one of the beams' trajectories, we could then write down their coordinates parameterised with the machine standard coordinates as follows:

$$x_1 = x\cos\tfrac{\theta_c}{2} + s\sin\tfrac{\theta_c}{2}, \qquad s_1 = s\cos\frac{\theta_c}{2} - x\sin\frac{\theta_c}{2}; \tag{68}$$

$$x_2 = -x\cos\tfrac{\theta_c}{2} + s\sin\tfrac{\theta_c}{2}, \qquad s_2 = -s\cos\frac{\theta_c}{2} - x\sin\frac{\theta_c}{2}. \tag{69}$$

So, we rewrite Eq. 59 using these, as:

$$\begin{aligned}\mathcal{L} &= 2Kn_1n_2fN_b\iiint_{-\infty}^{\infty}\mathrm{d}x\mathrm{d}y\mathrm{d}s\mathrm{d}s_0\,\times \\ &\quad [\rho_{1x}(x_1)\rho_{1y}(y_1)\rho_{1s}(s_1-s_0)\rho_{2x}(x_2)\rho_{2y}(y_2)\rho_{2s}(s_2+s_0)]\,,\end{aligned} \tag{70}$$

we can then use the integral:

$$\int_{-\infty}^{\infty}\mathrm{d}te^{-\left(at^2+bt+c\right)} = \sqrt{\frac{\pi}{a}}\cdot e^{\frac{b^2-ac}{a}}$$

and with some approximations for small angles $\theta_c/2 \ll 1$, so $\sin\theta_c/2 \sim \theta_c/2$ and

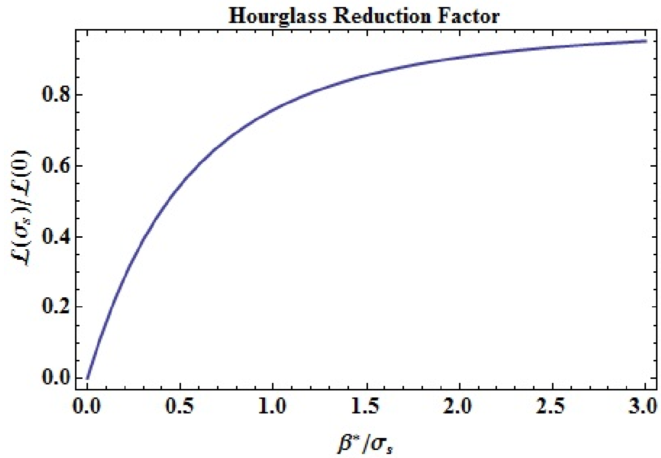

FIG. 13: Percentage of the total luminosity as a function of the ratio between β^* and the bunch length, showing a reduction due to the hourglass effect.

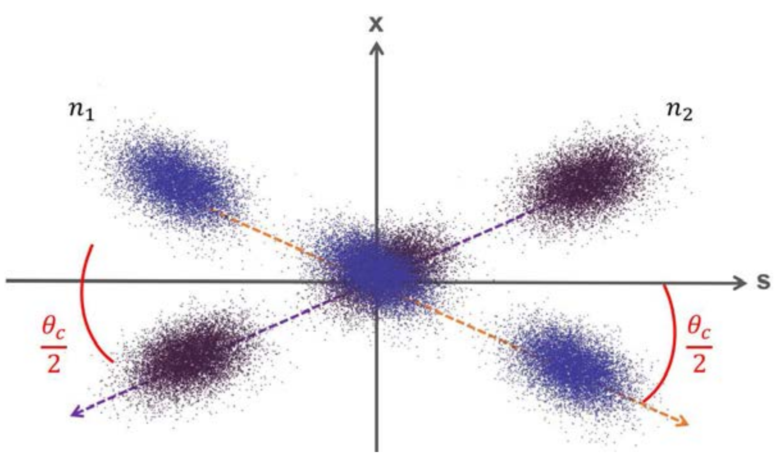

FIG. 14: Colliding beams with a crossing angle θ_c.

discarding all the terms $\sigma_x^k \sin^l \theta_c/2$ and $x^k \sin^l \theta_c/2$, for all $k+l \geq 4$, then:

$$R_c\left(\theta_c, \sigma_s\right) = \frac{1}{\sqrt{1+\left(\frac{\sigma_s}{\sigma_x}\tan\frac{\theta_c}{2}\right)^2}}, \tag{71}$$

is the geometric factor between bunches induced by the crossing angle θ_c and the beam longitudinal size σ_s, while $\beta^*_{x,y} = \sigma^2_{x,y}/\epsilon$ is the relation between the emittance ϵ and the beam transverse sizes at the interaction point. In general, all the above quantities are machine specific, but while the beta functions change along the lattice, also, it is by design that they reach their minimum values at the interaction point.

At the same time, Eq. 71 tells us that at a larger crossing angle, the geometric factor will grow smaller, making the luminosity to decrease as well. Again, why is that we need the crossing angle at the electron-ion then? Principally, for a large crossing angle there is a faster beam separation, reducing spurious signals due to undesired bunch collisions, amongst other benefits.

2.3 CRABBING CONCEPT AND LUMINOSITY RESTORATION

In the late 80's Robert Palmer suggested a very elegant solution to correct the geometric factor due to the crossing angle in colliders [22] and for this, we will need to define what is an rf transverse deflector. An rf transverse deflector is a radio frequency cavity that instead of accelerating the particles of a beam, it imprints a change on the transverse momentum as a function of the particle's position within the bunch, all these by using the electromagnetic fields confined within the resonant cavity. This takes us back to the Lorentz force, Eq. 1, for a charged particle moving on axis (z) through a horizontal (x) deflector, with speed close to the speed of light, it will see a transverse voltage given by:

$$V_T = \int_{-\infty}^{\infty} \mathrm{d}z \left[E_x(s) \cos\frac{\omega z}{c} + cB_y(z) \sin\frac{\omega z}{c} \right], \tag{72}$$

where E_x and B_y are the horizontal electric field and the vertical magnetic field sustained inside the cavity, respectively. While ω represents the angular frequency of the rf signal. Figure 15 shows the general concept of how the transverse voltage of a deflector acts on bunches arriving with different phases—with respect to the rf signal.

In Fig. 15, for the cases of the black and blue bunches that arrive with a **non-zero phase**, they will be "kicked" in one direction or the other—depending on the sign of the fields at the moment they arrive at the cavity location—being able in this way to separate the bunches as needed. For instance, the rf separators (499 MHz) in the CEBAF at Jefferson lab are in charge to separate the bunches to be sent to different magnet kickers that will provide simultaniusly beam to three different experimental halls (A, B, and C). A deflector operating in this mode is commonly called an **rf separator**.

Lets then take a closer look at the bunches arriving at the zero rf crossing (red), for which the net transverse moment given by the rf to the bunch centroid is zero. However, the head and tail of the bunch will see a voltage kicks with opposite signs

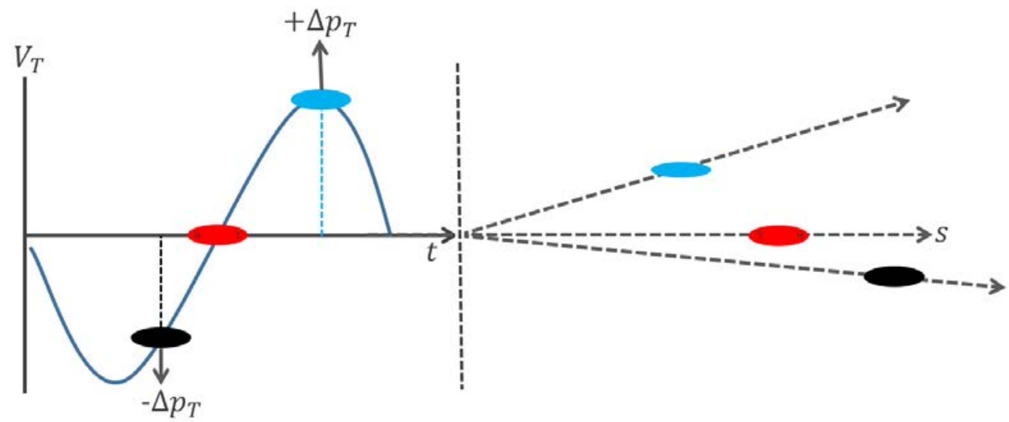

FIG. 15: Sketch of the transverse kick given by an rf deflector to bunches with different arriving times.

(see Fig. 16), in this way the trajectory of the bunch will not be altered, but instead the bunch will rotate.

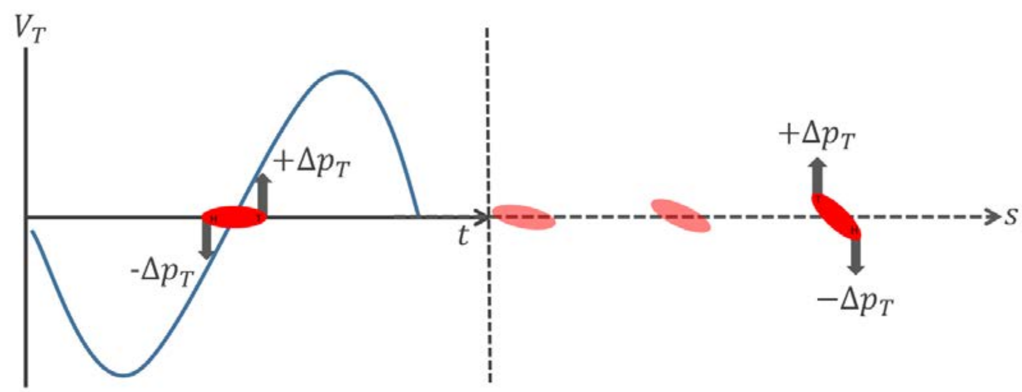

FIG. 16: Sketch of the transverse kick given by an rf crab cavity to the particles within a single bunch.

An rf deflector operated in this mode is known as a **crab cavity**, **crab corrector**, or **rf crabber**. Palmer's idea was to use rf cavities to induce a rotation on the bunches, allowing then the rotation to compensate the effect of the crossing angle, and to recover the head-on case for the bunch collisions (see Fig. 17 as opposed to Fig. 14).

If we work out the transverse crabbing voltage V_T, necessary to correct the geometrical factor due to the crossing angle, we obtain that in the case of a linear kick

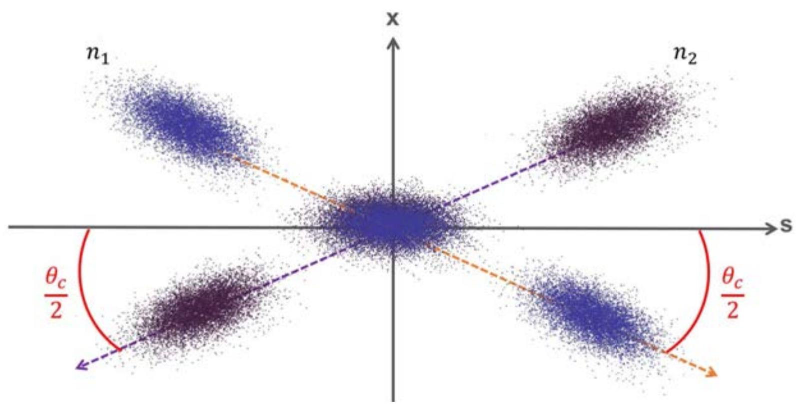

FIG. 17: Colliding beams with a crossing angle θ_c employing full crabbing correction.

without dispersion, it can be written as:

$$V_T = \frac{cE_b \tan \frac{\theta_c}{2}}{2\pi f \sqrt{\beta_x^* \beta_x^C}}, \tag{73}$$

where E_b is the beam energy, $\theta_c/2$ is the angle to be corrected by the crab cavity (per beam), f is still the bunch repetition rate, β^* and β^C the values of the β-function of the beam at the interaction point and at the crab cavity location,independently. The last factors show how for smaller β^* or higher beam energy, the crabbing kick required is higher for the same angle. While for higher frequencies as well as bigger beam envelopes at the crab cavities location, the required transverse kick to correct for the same angle is lower. Later on, Chapter 4 will focus in the crabbing concept and its two main schemes (global and local), as well as the specifics of the case for the Jefferson Lab's electron-ion collider.

CHAPTER 3

SUPERCONDUCTIVITY AND RADIOFREQUENCY

This chapter—similar to Chapter 2—will present a quick overview, this time of the cavity fundamentals and superconductivity, more than anything for completeness. It will also work as a preamble for the discussions later on. Since the main part of a crabbing system are the rf cavities themselves, then, it is only logical to lay down the basics of radiofrequency and—for our particular case—of superconductivity as well. In this way, readers with different backgrounds could easily pick up the main concepts and analyse the ideas developed throughout this dissertation. However, it is a common error in our area of study, to transcribe the most popular review books, like the **Padamsee, Knobloch, and Hays** [23], only because they do a great job explaining the theoretical basis, the timelines, and the empirical experience of superconducting rf. If the reader is interested in having a better understanding or have a wider view of the superconductivity in rf for accelerators, we encourage reading [23] and [24], amongst others. For a nice, short historical recount on superconductivity, read [25].

3.1 CAVITY FUNDAMENTALS

3.1.1 CONDUCTORS AND BOUNDARIES

A cavity is ideally defined as a volume of vacuum enclosed by a conducting surface. Then, lets enlist the boundary conditions for a vacuum/conductor interface, using the definitions described in Fig. 26, as:

$$\begin{aligned} \hat{n}\cdot\vec{D} &= \Sigma, \\ \hat{n}\times\vec{H} &= \vec{K}, \\ \hat{n}\cdot\left(\vec{B}-\vec{B}_c\right) &= 0, \\ \hat{n}\times\left(\vec{E}-\vec{E}_c\right) &= 0, \end{aligned}$$

where $\hat{n}$ is a vector normal to the conductor's surface, Σ is the surface charge density and $\vec{K}$ the surface current. Now, for linear materials without polarization or

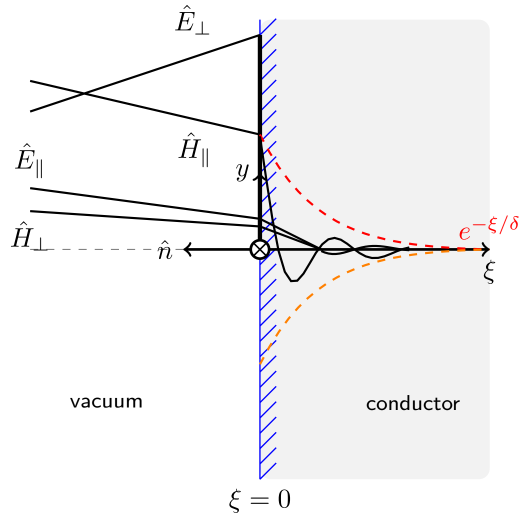

FIG. 18: Boundary conditions diagram for a vacuum/conductor interface.

magnetisation—like vacuum—we can use the definitions:

$$\begin{aligned}\vec{J} &= \sigma\vec{E}\,,\\ \vec{D} &= \epsilon\vec{E}\,,\\ \vec{H} &= \frac{1}{\mu}\vec{B},\end{aligned}$$

and so the Maxwell equation,—in differential form—can be written as:

- Gauss' Law: *the flux of electric field is proportional to the enclosed charge.*

$$\vec{\nabla}\cdot\vec{D} = \rho. \tag{74}$$

- Gauss' Law for magnetism: *the lines of the magnetic field close on themselves, there is no divergence and therefore there is no free magnetic monopoles.*

$$\vec{\nabla}\cdot\vec{B} = 0. \tag{75}$$

- Faraday's Law of Induction: *variations in time of magnetic fields generate electric fields, and vice versa.*

$$\vec{\nabla}\times\vec{E} = -\frac{\partial\vec{B}}{\partial t}. \tag{76}$$

- Ampère's (corrected) Law: *relates the magnetic field to the electrical—and displacement—currents in a circuit.*

$$\vec{\nabla} \times \vec{H} = \left(\vec{J} + \frac{\partial \vec{D}}{\partial t} \right). \tag{77}$$

We can differentiate with respect to time ($\frac{\partial}{\partial t}$) Eq. 77 and since for the vacuum there are no free currents (i.e. $\vec{J} = 0$), then:

$$\begin{aligned} \frac{\partial}{\partial t} \left(\vec{\nabla} \times \vec{H} \right) &= \frac{\partial^2 \vec{D}}{\partial t^2}, \\ \Rightarrow \frac{\partial}{\partial t} \left(\vec{\nabla} \times \vec{B} \right) &= \frac{1}{c^2} \frac{\partial^2 \vec{E}}{\partial t^2}. \end{aligned} \tag{78}$$

Since $c = 1/\sqrt{\epsilon_0 \mu_0}$ and now taking the curl ($\vec{\nabla}\times$) of Eq. 76, then:

$$\begin{aligned} \vec{\nabla} \times \left(\vec{\nabla} \times \vec{E} \right) &= -\vec{\nabla} \times \left(\frac{\partial \vec{B}}{\partial t} \right), \\ \vec{\nabla} \left(\vec{\nabla} \cdot \vec{E} \right) - \nabla^2 \vec{E} &= -\frac{\partial}{\partial t} \left(\vec{\nabla} \times \vec{B} \right). \end{aligned} \tag{79}$$

If we are in the vacuum, there is no free charges either ($\rho = 0$). Then, from Eq. 74 and 78, we can simplify Eq. 79 to:

$$\begin{aligned} \nabla^2 \vec{E} = \frac{\partial}{\partial t} \left(\vec{\nabla} \times \vec{B} \right) &= \frac{1}{c^2} \frac{\partial^2 \vec{E}}{\partial t^2}, \\ \Rightarrow \nabla^2 \vec{E} - \frac{1}{c^2} \frac{\partial^2 \vec{E}}{\partial t^2} &= 0, \\ \therefore \left(\nabla^2 + \frac{\omega^2}{c^2} \right) \vec{E} &= 0, \end{aligned} \tag{80}$$

which is the well known wave equation with planar waves as solutions ($E \propto e^{i\left(\vec{k}\cdot\vec{x} - \omega t\right)}$). Now, if we do a similar procedure, but this time taking the derivative with respect to time ($\frac{\partial}{\partial t}$) of Eq. 76 and the curl ($\vec{\nabla}\times$) of Eq. 77 instead, then:

$$\frac{\partial}{\partial t} \left(\vec{\nabla} \times \vec{E} \right) = -\frac{\partial^2 \vec{B}}{\partial t^2}, \tag{81}$$

$$\begin{aligned} \vec{\nabla} \times \left(\vec{\nabla} \times \vec{H} \right) &= \frac{\partial}{\partial t} \left(\vec{\nabla} \times \vec{D} \right), \\ \Rightarrow \vec{\nabla} \left(\vec{\nabla} \cdot \vec{B} \right) - \nabla^2 \vec{B} &= \frac{1}{c^2} \left(\vec{\nabla} \times \vec{E} \right), \\ \Rightarrow \nabla^2 \vec{B} &= -\frac{1}{c^2} \left(\vec{\nabla} \times \vec{E} \right), \end{aligned} \tag{82}$$

mixing then Eq. 81 and 82:

$$\begin{aligned}\nabla^2\vec{B} = \frac{\partial}{\partial t}\left(\vec{\nabla}\times\vec{E}\right) &= \frac{1}{c^2}\frac{\partial^2\vec{B}}{\partial t^2},\\ \Rightarrow\ \nabla^2\vec{B} - \frac{1}{c^2}\frac{\partial^2\vec{B}}{\partial t^2} &= 0,\\ \therefore\ \left(\nabla^2 + \frac{\omega^2}{c^2}\right)\vec{B} &= 0. \qquad (83)\end{aligned}$$

Defining then the wave number as $k = \omega/c$, then Eq. 80 and 83, can be written as:

$$\left(\nabla^2 + k^2\right)\left\{\begin{array}{c}\vec{E}\\ \vec{B}\end{array}\right\} = 0. \qquad (84)$$

3.1.2 PILLBOX CAVITY AND CAVITY MODES

If we consider a cylindrical conducting boundary, then Eq. 84 has solutions of the form:

$$\vec{E}\left(x,y,z;t\right) = \vec{E}(x,y)e^{i(kz-\omega t)}, \qquad (85)$$

$$\vec{B}\left(x,y,z;t\right) = \vec{B}(x,y)e^{i(kz-\omega t)}. \qquad (86)$$

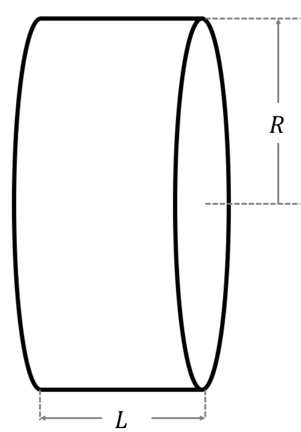

FIG. 19: Pillbox cavity with cylindrical symmetry.

For this cylindrical symmetric cavity, there are two sets of solutions for Eq. 83, which correspond to propagating waves with a transverse magnetic (TM) and with transverse electric fields (TE) with zero longitudinal electric field on axis. Considering the **pillbox** cavity, as depicted in Fig. 19, then the solutions for the TM modes are:

$$\begin{aligned}
E_z &= E_0 \cos\left(k_p z\right) J_m\left(k_{r,mn} r\right) \cos\left(m\phi\right), &(87)\\
E_r &= -E_0 \left(\frac{k_p}{k_{r,mn}}\right) \sin\left(k_p z\right) J_m'\left(k_{r,mn} r\right) \cos\left(m\phi\right), &(88)\\
E_\phi &= E_0 \left(\frac{k_p}{k_{r,mn}^2 r}\right) \sin\left(k_p z\right) J_m\left(k_{r,mn} r\right) \cos\left(m\phi\right), &(89)\\
B_z &= 0, &(90)\\
B_r &= iE_0 \left(\frac{m\omega}{c^2 r k_{r,mn}^2}\right) \cos\left(k_p z\right) J_m\left(k_{r,mn} r\right) \cos\left(m\phi\right), &(91)\\
B_\phi &= iE_0 \left(\frac{m\omega}{c^2 k_{r,mn}}\right) \cos\left(k_p z\right) J_m'\left(k_{r,mn} r\right) \cos\left(m\phi\right), &(92)
\end{aligned}$$

while for the TE modes we have:

$$\begin{aligned}
E_z &= 0, &(93)\\
E_r &= iB_0 \left(\frac{m\omega}{r\left(k_{r,mn}'\right)^2}\right) \sin\left(k_p z\right) J_m\left(k_{r,mn}' r\right) \sin\left(m\phi\right), &(94)\\
E_\phi &= iB_0 \left(\frac{\omega}{k_{r,mn}'}\right) \sin\left(k_p z\right) J_m'\left(k_{r,mn}' r\right) \sin\left(m\phi\right), &(95)\\
B_z &= B_0 \sin\left(k_p z\right) J_m\left(k_{r,mn}' r\right) \cos\left(m\phi\right), &(96)\\
B_r &= B_0 \left(\frac{k_p}{k_{r,mn}'}\right) \cos\left(k_p z\right) J_m'\left(k_{r,mn}' r\right) \cos\left(m\phi\right), &(97)\\
B_\phi &= -B_0 \left(\frac{m k_p}{r\left(k_{r,mn}'\right)^2}\right) \cos\left(k_p z\right) J_m'\left(k_{r,mn} r\right) \sin\left(m\phi\right), &(98)
\end{aligned}$$

where R is the cavity radius, L its length, J_m are the first kind Bessel function of m-th order, J_m' its derivative, with m as the number of half cycles variation in the radial direction, x_{mn} and x_{mn}' are the zeroes of the Bessel functions ($J_m(x_{mn}) = 0$) and its derivative, ($J_m'(x_{mn}') = 0$) respectively. Also, $k_p = p\pi/L$ is the wave number in the longitudinal modes and $p = 0, 1, 2, \ldots$ is the number of half cycles of variation in the z-direction, $k_{r,mn} = x_{mn}/R$ and $k_{r,mn}' = x_{mn}'/R$ are the wave numbers in the radial modes, and finally n is the number of complete cycles of variation in the angular dimension. Next, we can describe the resonant modes using the values of m, n, and p, expressing the modes' wave numbers as:

$$\text{For the TM modes:} \quad \omega_{mnp,TM} = c\sqrt{\left(\frac{x_{mn}}{R}\right)^2 + k_p^2}, \tag{99}$$

$$\text{For the TE modes:} \quad \omega_{mnp,TE} = c\sqrt{\left(\frac{x_{mn}'}{R}\right)^2 + k_p^2}. \tag{100}$$

The lowest mode of the TE modes is the TE_{111} mode and of the TM modes is the TM_{010} mode, the latter—as long as $R/L \geq 0.5$—is the fundamental mode of the elliptical cavities and is the most commonly used mode to accelerate charged beams in the machines (see Fig. 20). This type of cavities are known as **TM-class** cavities and is important to notice that the frequency of the TM_{010} mode depends only on the cavity radius.

$$\omega_{010} = \frac{x_{010}c}{R}. \tag{101}$$

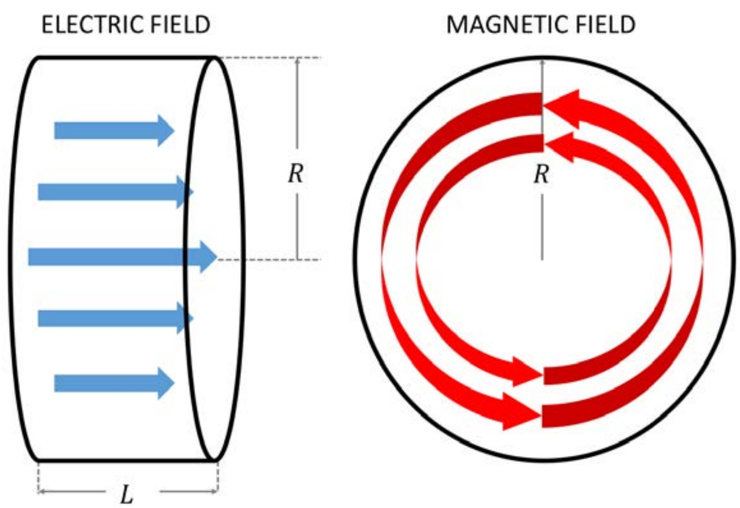

FIG. 20: Pillbox cavity showing the field configuration for the TM_{010} accelerating mode.

3.2 TM_{110} VS TEM DEFLECTORS

Since the interest of this work in rf cavities is for deflecting (crabbing), rather than accelerating applications, we will take a look at the TM_{110} mode of elliptical cavities. As previously mentioned, TM modes have zero longitudinal electric field on axis ($E_z(r = 0) = 0$) and the transverse mode has two polarizations, as long as the cylindrical geometry is conserved. It is for this reason that the deflecting and crab cavities operating in the TM_{110} have a **squashed elliptical** geometry that breaks the symmetry and separates the degenerated modes in frequency (see Fig. 21).

There are other type of cavities based in coaxial resonant lines, which are known as **TEM** resonators (see Fig. 22). A TEM resonator sustains its fields between the outer and an inner conductor. However, they differ from the TM resonators, mentioned

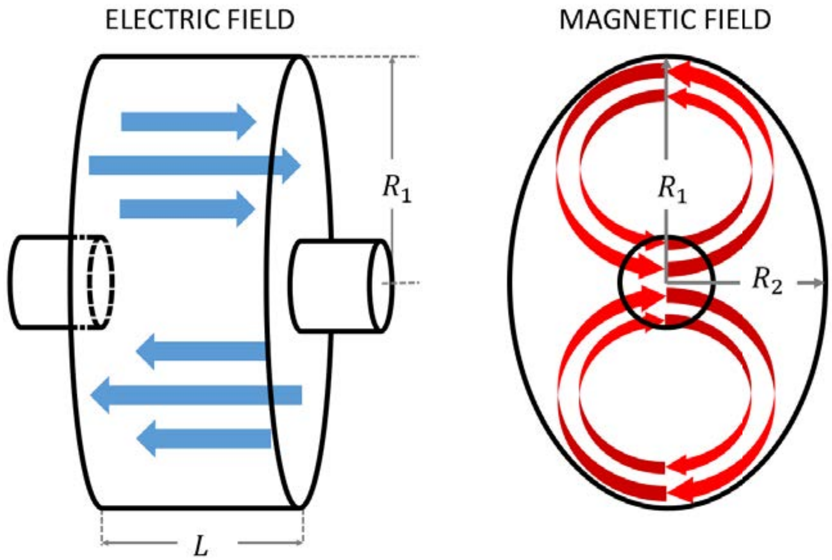

FIG. 21: Squashed elliptical cavity showing the field configuration for the TM_{110} deflecting mode.

before, because in the TM modes the frequency is related to the transverse boundary conditions due to the conducting walls of the resonator, while for the TEM modes, the mode frequency is determined by its length (half wave length $\lambda/2$) and not by its transverse dimensions. This is particularly helpful for low frequencies, when a TEM resonator can be roughly half the size of a TM cavity at the same frequencies.

We can consider the half wave resonator as a two gap accelerating structure, there are **multi-gap** TEM structures, such as the multi-spoke cavities [2] that are multi connected geometries. Delayen and Huang developed, in 2009, the compact geometry of a TEM class deflecting cavity for high-β particles called the **parallel rod** cavity [26]. Figure 23 shows a diagram of the parallel rod cavity concept. In this case, just as for the accelerating modes, TEM deflectors reduce considerably the dimensions of the resonators, making them more suitable for applications in which the physical space is constraint by the machine.

3.3 TE-LIKE DEFLECTORS: *THE RF DIPOLE*

Other mode of the elliptical cavities that is important to mention is the TE_{111} mode, because it has a transverse electric field on axis that could also be thought to be used as a deflecting mode (see Fig. 24). However, since the contributions of the

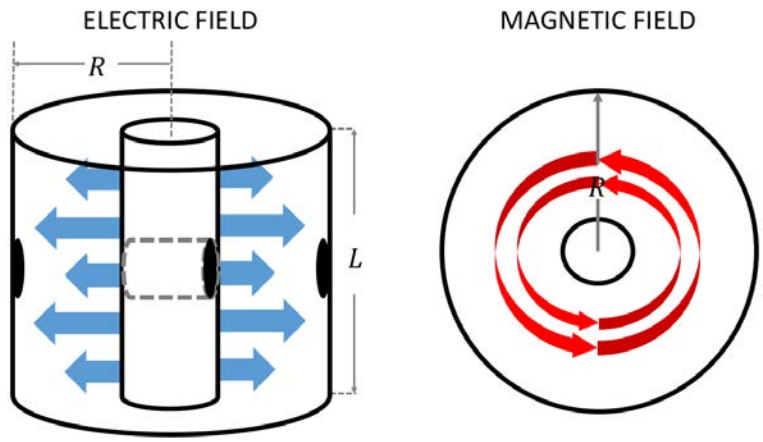

FIG. 22: Field configuration of a TEM class (half wave) accelerator cavity.

electric and the magnetic fields cancel each other exactly, there is no net deflection of the beam.

The case of the TE_{111} mode is relevant for this discussion as there are a series of compact rf cavity designs, for deflecting and crabbing applications, which evolved from TEM class to **TE-like** resonators, such as the Brookhaven National Lab's **Double Quarter Wave** [27] and the Old Dominion University's **RF Dipole** [28]. The reason why they are TE-like and not simply TE resonators is because the contribution to the deflection given by the electric field is not fully cancelled out by the magnetic field contribution. This is achieved by cleverly optimising the geometry to ensure that the electric field is concentrated along the beam axis region, while the magnetic field density in the same region is considerably smaller, as a result a net transverse kick is given to the bunches. Figure 25 (top) shows the electric (a) and magnetic (b) fields of the TE_{111} mode of a specific cylindrical cavity. If we add two loading elements on the sides of the same cylindrical cavity, we obtain the basic rf dipole geometry. Depicted in Fig. 25 (bottom) the electric (c) and magnetic (d) field distribution, very similar to the ones of the TE_{111} mode, with the difference that the electric field density is higher along the beam axis, while the magnetic field density is roughly the same as before in that region.

There are other interesting compact designs for crabbing applications, such as the Lancaster Univeristy's **Four Rod** cavity [29], but now on we will focus on the rf dipole, since it is the geometry we found to be more suitable for the electron-ion crabbing applications at 750 MHz, that are the subject of this dissertation.

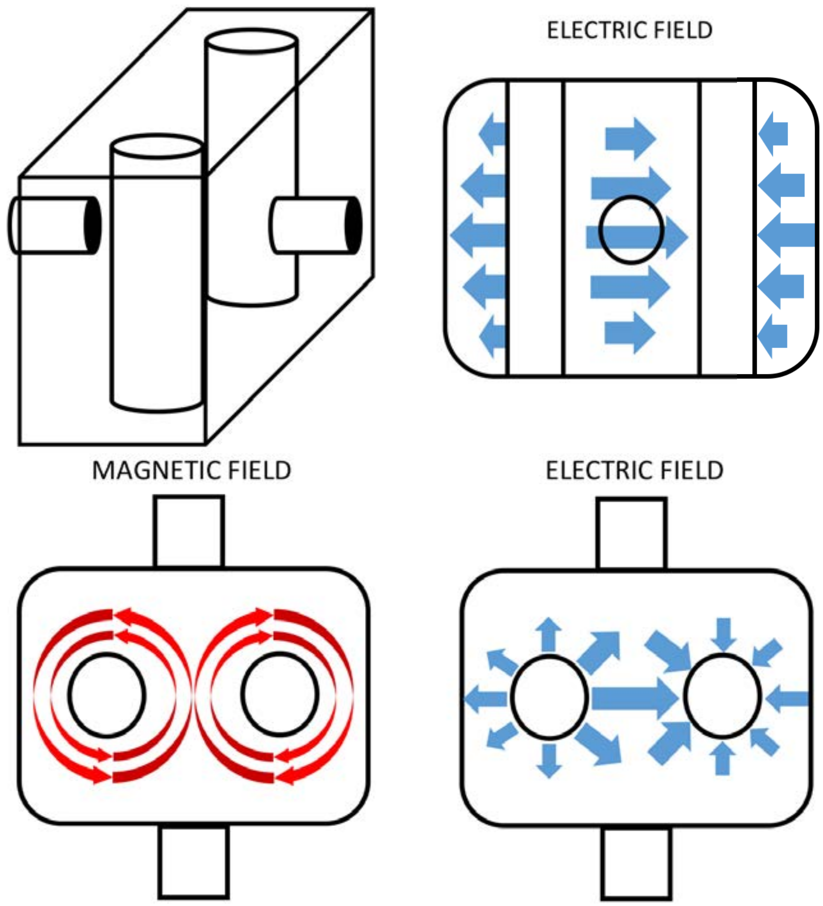

FIG. 23: TEM class (parallel rod) deflecting/crabbing cavity and its fields distribution.

3.4 FIGURES OF MERIT

The transverse momentum imprinted on a particle of charge q, traversing a deflecting cavity—like the ones described above—on axis, can be defined as $\vec{p}_T = \int_{-\infty}^{\infty} \mathrm{d}t \vec{F}_T$, where $\vec{F}_T$ is the transverse force derived from Eq. 1. Then, considering that $z = vt$, with v as the particles velocity, we can write:

$$\vec{p}_T = \frac{q}{v} \int_{-\infty}^{\infty} \mathrm{d}z \left[\vec{E}_T + \left(\vec{v} \times \vec{B}_T \right) \right], \tag{102}$$

where $\vec{E}_T$ and $\vec{B}_T$ denote the transverse components of the on axis cavity fields.

At this point, it is convenient to mention the Panofsky-Wenzel theorem, that relates the transverse gradient of the accelerating voltage and its resulting transverse momentum kick. Joachim Tückmantel gives a short but nice derivation of this

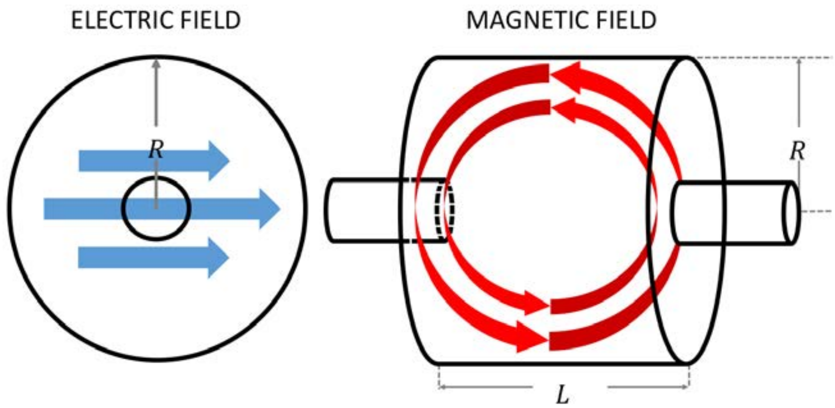

FIG. 24: Elliptical cavity showing the field configuration for the TE_{111} mode.

theorem in his technical note [30]. Considering this and for a particle traveling at constant velocity $\vec{v}$ but with an offset r_0—instead of on axis—we can write Eq. 102 as:

$$\begin{aligned}\vec{p}_T &= -\frac{iq}{\omega}\int_{-\infty}^{\infty} \mathrm{d}z \vec{\nabla}_T E_z, \\ &= -\lim_{r_0\to 0}\left(\frac{iq}{r_0\omega}\int_{-\infty}^{\infty} \mathrm{d}z \left[E_z\left(r_0, z\right) - E_z\left(0, z\right)\right]\right), \end{aligned} \tag{103}$$

with ω as the frequency of the mode.

For the rf dipole crab cavity studied in this dissertation as a horizontal (x) crab cavity, the transverse fields correspond to $\vec{E}_T = E_x(z)\cos(\omega t)\,\hat{x}$ and $\vec{B}_T = B_y(z)\sin(\omega t)\,\hat{y}$. Then, for $\beta = 1$ particles, the transverse voltage is:

$$V_T = \int_{-\infty}^{\infty} \mathrm{d}z \left[E_x\left(z\right)\cos\left(\frac{\omega z}{c}\right) + cB_y\left(z\right)\sin\left(\frac{\omega z}{c}\right)\right]. \tag{104}$$

Since we are treating with particles traveling with $\beta = 1$, we define our reference length, in order to establish the total transverse voltage seen by the particle inside the cavity fields V_T, as half rf wavelength ($\lambda/2$), such as:

$$E_T = \frac{V_T}{(\lambda/2)}, \tag{105}$$

we will also refer to V_T^* as the transverse voltage at 1 MV/m of transverse field, defined as:

$$V_T^* = (\lambda/2) \times 1\mathrm{MV/m}. \tag{106}$$

Later on, in the chapter dedicated to design and optimization, we will discuss the importance of the peak surface fields for superconducting cavities. These fields

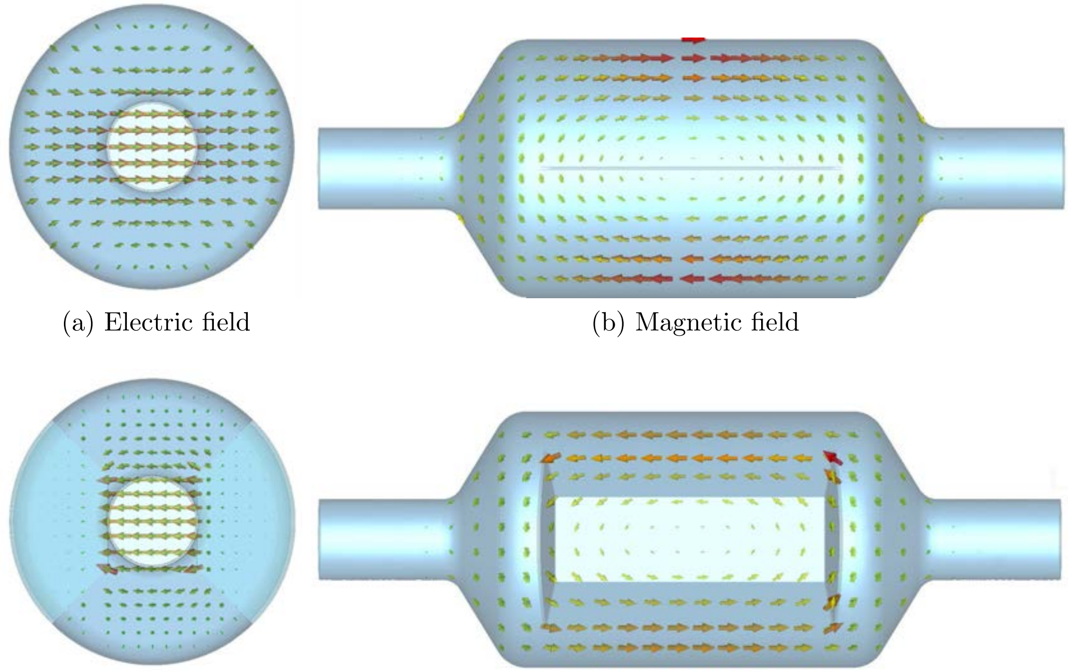

(a) Electric field (b) Magnetic field

(c) Electric field (d) Magnetic field

FIG. 25: TE_{111} and TE-like modes on a cylindrical (top) and rf dipole (bottom) geometries, respectively.

(E_p and B_p) will set the limit to the operational gradients in any superconducting cavity, since for the peak electric surface field E_p there is a field emission limit and for the peak magnetic surface field B_p there is a critical field H_c, after which, it is not possible for the materials to maintain the superconducting state. We will better define these fields by normalising them to the transverse gradient as:

$$E_p^* = \frac{E_p}{E_T}, \tag{107}$$

$$B_p^* = \frac{B_p}{E_T}. \tag{108}$$

In order to sustain the fields, currents must flow on the cavity surfaces. Even for superconductors, there is a small resistance at rf frequencies, this resistance, even when small—in the order of tens of nΩ for clean Nb—generates losses and dissipates energy. This dissipation of energy is still smaller than for the case of normal conductors, for instance, the surface resistance for Cu is typically in the order of mΩ. We characterise these losses by the surface resistance R_s, which is defined in terms of the power dissipated per unit area on the cavity surface due to the Joule's effect ($\mathrm{d}P_{\text{loss}}/\mathrm{d}S$). Using this, we can write the total power dissipated by the cavity walls as:

$$P_{\text{loss}} = \frac{R_s}{2}\int_S \mathrm{d}S|\vec{H}|^2, \tag{109}$$

where S is the total rf surface of the cavity walls.

We will present another important cavity parameter, the **quality factor** Q_0, which roughly gives 2π times the number of rf cycles needed to dissipate the total energy U contained by the fields inside the cavity (see Eq. 110).

$$Q_0 = \frac{\omega U}{P_{\text{loss}}}. \tag{110}$$

Since the rf fields inside a cavity are alternating between each other, in a way that when the electric field is maximum, then the magnetic field is zero, and vice versa, the total stored energy on the fields can be calculated using the maximum value of either field ($|\vec{E}|$ or $|\vec{H}|$), as a result:

$$U = \frac{\epsilon_0}{2}\int_V \mathrm{d}V|\vec{E}|^2 = \frac{\mu_0}{2}\int_V \mathrm{d}V|\vec{H}|^2 \tag{111}$$

and V denotes the full vacuum volume inside the resonator.

If we assume that R_S is homogeneous over the entire rf surface, then we can simplify the **geometric factor** G as:

$$G = \frac{\omega\mu_0\int_V \mathrm{d}V|\vec{H}|^2}{\int_S \mathrm{d}S|\vec{H}|^2} = Q_0 R_s. \tag{112}$$

This quantity is a constant of each geometry and is invariant under linear scaling of the cavity, thus, it is independent of the frequency. This definition will be used in the section related to the cavity testing to estimate the surface resistance at different temperatures, using the values of G calculated from numerical simulations for the 750 MHz rf dipole crab cavity developed as part of this work.

The losses in the cavity can also be characterised using the definition of the shunt impedance R_{sh}, which expresses the ratio between the square of the voltage V sustained by the cavity and the power dissipated through the cavity walls. Then, the greater the shunt impedance is, the lesser dissipated power for a given cavity voltage, or:

$$R_{\text{sh}} = \frac{V^2}{P_{\text{loss}}} \tag{113}$$

and for transverse deflectors:

$$R_T = \frac{V_T^2}{P_{\text{loss}}}, \tag{114}$$

where R_T is the transverse shunt impedance. This definition is in the linac-Ω convention—lepton machines—since for the circuit-Ω convention—hadron machines—there is an extra factor of 1/2.

There is a quantity that describes how does the rf mode couples to the charges in the beam, named R/Q. The R/Q is both independent on the surface resistance and the cavity size, making it handy to use as a figure of merit and an optimising parameter. In our case, since we are interested in deflecting cavities, we will define the **transverse**

$$\left[\frac{R}{Q}\right]_T = \frac{V_T^2}{\omega U}. \tag{115}$$

One would like to maximise the R/Q value for the operating mode to ensure effective acceleration (or deflection), while reducing it for undesired modes. In the case of superconducting cavities, the loss power dissipation will sustain the fields—including undesired modes—for long enough time to interact again with the beam. Since a high R/Q value means strong interactions between the beam and the rf fields, undesired modes that strongly couple to the beam will degrade its quality and in extreme cases produce full loss of the beam. Higher order mode damping becomes a more important issue in superconducting cavities than for normal conducting ones.

Finally, we define one last parameter as the product of the transverse shunt impedance and the surface resistance, which relates the cavity's geometrical factor with the transverse R/Q, as:

$$R_T R_s = \left[\frac{R}{Q}\right]_T G. \tag{116}$$

This parameter is useful during the geometry design phase, since typically both G and the transverse R/Q compete with each other when varying the geometrical parameters of the cavity, making $R_T R_s$ a suitable parameter to optimize both the geometrical factor and the $[R/Q]_T$.

3.5 HIGHER ORDER MODES

We have seen that the wave equation (Eq. 84) allows several eigenfrequencies, which in the case of TM and TE modes correspond to Eq. 99 and Eq. 100, respectively. This means that we can have different modes excited in a single structure, even when these modes are undesired. Parasitic modes can be excited by diverse sources, such as beam currents, noise in the rf sources, and mechanical modes of the cavity systems.

There are three main classifications to these undesired modes: those with frequencies bellow the operating frequency known as **lower order modes** or LOMs; those with frequencies close to the operating frequency but with different field configuration called **similar order modes** or SOMs; and finally the most abundant type, those with frequencies above the operating frequency, the so called **higher order modes** or HOMs.

For example, let's consider that we want to use an elliptical cavity as a deflector in the TM_{110} mode. Then, it will have as a LOM the accelerating mode TM_{010}, since—following Eq. 99—$\omega_{110} \sim 1.59\,\omega_{010}$ and is highly likely that we will have to design a low pass or notch coupler to be able to extract such mode from the cavity to operate at the desired deflecting mode without problems. It is very important to remark, at this point, that another advantage of TEM and TE-like over TM deflectors, is the absence of LOMs, since the deflecting mode is the fundamental—lowest frequency—mode.

It is said that a good accelerator is also a good decelerator. For the case of an accelerating cavity this means that a resonator is as capable to transfer energy from its fields to a charged beam, as it is to transfer energy from a charged beam to its own fields. This can be extended to transverse deflectors and in general to any resonant cavity. The time structure of the beam bunches will dictate the frequencies to be excited inside the cavity, then the geometry of the cavity itself will determine which ones of those frequencies will correspond to resonant modes that can be sustained inside. The R/Q—transverse and longitudinal— determines the intensity of each of the n-excited modes and each one of these n-modes will have their own natural decay time $\tau_n = Q_{0,n}/\omega_n$, with their own quality factor $Q_{0,n}$ and frequency ω_n. The modes will be classified, depending on their field configuration, in deflecting or accelerating. We will talk more about the higher order modes in Chapter 5, when we analyse the HOMs of the 750 MHz rf dipole.

The fields generated by the charged bunches traversing the cavities are compared to the wakes that a sailing boat leaves behind in the water and are called precisely for this reason **wakefields**. The study of wakefields becomes more important in machines with high currents and short bunches. A good design will include couplers that will strongly couple and extract the power of high R/Q parasitic modes, without disrupting the operating mode. To design such couplers or dampers, one needs first to understand which ones are the dangerous modes. This comes from the analysis of the cavity design itself. Secondly one needs to work with an impedance budget, this comes from analysis that the beam dynamics and impedance groups perform, not only for the rf systems, but for the entire machine. At this point, for the case of the electron-ion collider at Jefferson Lab, the early stages of the machine design—at which we started to develop the crabbing systems—have not allowed to have an impedance budget yet, making the design of HOM damping schemes a problem that will have to be reassessed later on, once the impedance budget has been laid out.

3.6 MULTIPOLE COMPONENTS

We remember for the case of the magnets studied already in Chapter 2 that Eq. 11 expresses the magnetic field in terms of its multipole components, if we rewrite Eq. 11 in cylindrical coordinates, we have:

$$B(r,\phi) = B_{\text{ref}} \sum_{n=0}^{\infty} (a_n - ib_n) \left(\frac{r}{r_{\text{ref}}}\right)^n e^{in\phi}, \tag{117}$$

where B_{ref} corresponds to the field at a given radius r_{ref} and ϕ is just the phase between the normal and skew $2(n+1)$-pole components.

The importance of studying the multipole components in rf structures—similar to the case of the magnets—is based on the fact that azimuthal asymmetries in the geometry will create non-uniformities in the fields across the beam aperture. In a deflector, these non-uniformities in the transverse field could degrade the emittance of the beam due to the undesired components generated in the transverse momentum of its particles. Different from the static case of the magnets, the multipole components in rf structures have a time dependence and particles arriving at different times—different phases—will experience them in different ways, in general we can represent these time dependent multipoles as:

$$E_z(r,\phi,z)e^{i\omega t} = \sum_{n=0}^{\infty} E_z^{(n)}(z) r^n e^{i(n\phi+\omega t)}, \tag{118}$$

and by a Fourier series expansion:

$$\begin{aligned} E_z^{(n)}(z) &= \frac{1}{2\pi}\frac{1}{r^n}\int_0^{2\pi} \mathrm{d}\phi E_z(r,\phi,z)e^{i\omega t}, & (119)\\ &= \frac{1}{2\pi}\frac{1}{r^n}\int_0^{2\pi} \mathrm{d}\phi E_z(r,\phi,z)\left[\cos(n\phi) + i\sin(n\phi)\right], & (120) \end{aligned}$$

where the cos and sin terms in Eq. 120 define the normal and skew multipole components—respectively—for an rf cavity. We can write the time dependent multipole component simply by adding the $e^{i\omega t}$ factor to Eq. 120. We will use these definitions in Chapter 5 to present a general method to tailor the multipole components in the 750 MHz rf dipole. This will allow us to customise the fields according to the multipole specifications for virtually any given application.

3.7 SUPERCONDUCTIVITY

As a preamble to this section, we would like to recommend the lecture of [31], where Van Delft and Kes tell the story of how the Dutch physicist H. Kamerlingh-Onnes discovered superconductivity back in the first decade of the 1900's. Also, we would like to highlight that all the formulas presented here have been taken from literature and, with the intention of not over extending this review, we will not fully derive them or remark all the considerations taken in their derivations. Again, this section presents only a sufficient set of superconductivity concepts to allow any reader, unfamiliar with the subject, to follow the content of this dissertation.

We have previously mentioned that one of the characteristics of the superconducting materials, that makes them so attractive for the construction of rf cavities, is their notably low electrical resistance—in the order of tens of nΩ—in contrast to the normal conductors—in the order of mΩ, for the same frequency ranges. This "perfect conductivity" characteristic is reached around a critical temperature T_c that is material specific, for example: 7.2 K for lead, 9.2 K for Niobium, 18.1 K for Nb_3Sn, etc. [32]. However, in 1933 Meissner and Ochsenfeld discovered a second signature of the superconductors, perfect diamagnetism [33]. The expulsion of the magnetic field from the bulk material, as the temperature goes bellow T_c, is known as the Meissner effect and it suggests that at a critical magnetic field $B_c(T)$, superconductivity will break down. The temperature dependance of B_c can be approximated by the empirical relation:

$$B_c(T) = B_0(0)\left[1 - \left(\frac{T}{T_c}\right)^2\right]. \tag{121}$$

Figure 26 shows the behavior of the critical field with temperature.

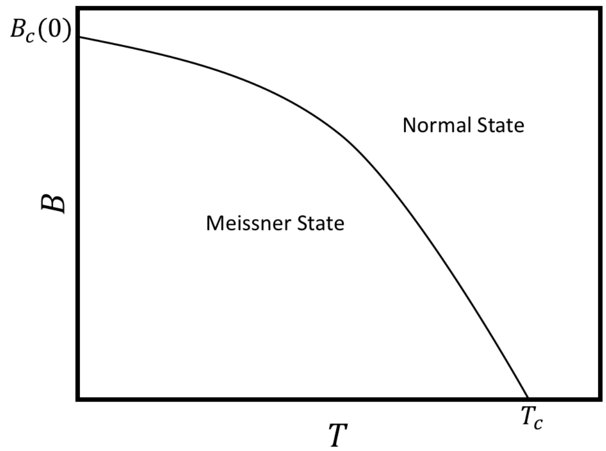

FIG. 26: Temperature dependance of the critical field for a Type-I superconductor.

3.7.1 THE TWO-FLUID MODEL

The idea behind the two-fluid model is that in a superconductor, there is a current carried by the normal free electrons, while there is a super-current carried by what behaves like a superfluid condensate of "super-electrons". Without going into any details of the super-current carriers, we can use a sub-index n to denote the normal carriers and the sub-index s to denote the superconducting carriers. Therefore, we write the equations that describe the microscopic fields due to this super-current $\vec{J}_s$, as:

$$\frac{\partial \vec{J}_s}{\partial t} = \frac{n_s e^2}{m_s}\vec{E}, \tag{122}$$

$$\vec{\nabla} \times \vec{J}_s = -\frac{n_s e^2}{m_s}\vec{B}, \tag{123}$$

where m_s and n_s are the mass and the density of super-electrons, respectively, e is the natural charge, and $\vec{J}_s = -en_s\vec{v}_s$. Equations 122 and 125 are commonly known as the **London equations**. While for the normal conducting carriers:

$$\vec{J}_n = \sigma_n \vec{E} \quad \text{and} \quad \vec{J}_n = -en_n\vec{v}_n. \tag{124}$$

Equations 122 and 125 imply that the total density of carriers is the mix between the n- and the s-carriers: $n = n_n + n_s$.

Now, to describe the screening behavior of superconductors in the Meissner state, we assume an external field B_0, applied in the z-direction to the surface of the

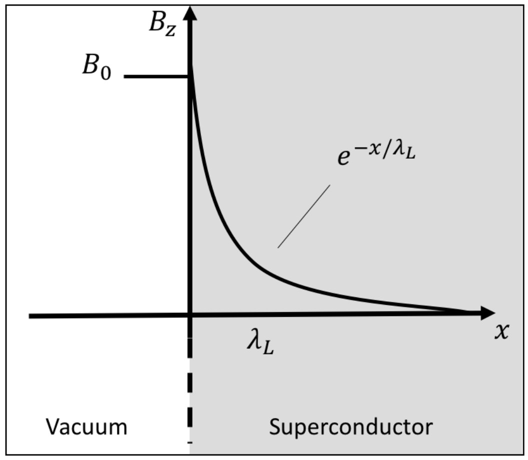

FIG. 27: Magnetic field's exponential decay inside a superconductor.

superconductor (see Fig. 27). We then apply Eq. 76 to Eq. 125 and considering there are no displacement currents, we can write:

$$\begin{aligned} \vec{\nabla} \times \left(\vec{\nabla} \times \vec{B}\right) &= -\frac{\mu_0 n_s e^2}{m_s} \quad \vec{B}, \\ \Rightarrow \quad \frac{\mathrm{d}^2 B_z(x)}{\mathrm{d}x^2} - \frac{\mu_0 n_s e^2}{m_s} B_z(x) &= \quad 0. \end{aligned} \tag{125}$$

The solution to Eq. 125 is $B_z(x) = B_0 e^{-x/\lambda_L}$, with the **London penetration depth** λ_L given by

$$\lambda_L = \sqrt{\frac{m_s}{\mu_0 n_s e_s^2}} \tag{126}$$

and thus $j_{s,y}(x) = j_{s,0} e^{-x/\lambda_L}$. Consequently, both the field and the current density exponentially decrease with the characteristic length λ_L, and it is the penetration depth that ultimately explains the external magnetic field expulsion by superconductors.

One problem that the London equations have, is that they describe only a local phenomenon, while superconductivity involves the coherent behavior of the superconducting carriers at a non-local level. For this reason, A. Pippard introduced the concept of the **coherence length** ξ, at which the coherent behavior operates in the presence of scattering [34]. Considering ξ_0 as the coherence length of the pure material, then:

$$\frac{1}{\xi} = \frac{1}{\xi_0} + \frac{1}{\ell}\,, \tag{127}$$

with $\ell = v_F \tau = 2\pi v_F/\omega_D$, as the electrons' mean free path, v_F is the Fermi velocity and ω_D is the Debye frequency [35]. All this permitted to have a phenomenological generalised expression for the supercurrent, as:

$$\vec{J}_s = -\frac{3n_s e^2}{4\pi m_s c\xi_0} \int \mathrm{d}^3 r' \frac{\vec{\rho}\left(\vec{\rho}\cdot\vec{A}\left(\vec{r'}\right)\right)}{\rho^4} e^{-\rho/\xi}, \tag{128}$$

where $\vec{\rho} = \vec{r} - \vec{r'}$ and $\vec{A}$ is the vector potential.

Using $\nabla^2 \vec{B} = \vec{B}/\lambda^2$, we find the penetration depth to be dependent of the parameters ξ_0, λ_L, and ℓ. Three important regimes can be defined, depending on the relative magnitudes of λ, ξ_0, and ℓ, as:

$$\begin{aligned}
\lambda,\, \ell \gg \xi_0 \quad &\Rightarrow \quad \lambda = \lambda_L, \quad \text{the } \textit{London limit}, \\
\ell \gg \xi_0 \gg \lambda \quad &\Rightarrow \quad \lambda \gg \lambda_L, \quad \text{the } \textit{Pippard limit}, \\
\text{and} \quad \lambda \gg \ell \quad &\Rightarrow \quad \lambda = \lambda_L \sqrt{1 + \xi_0/\ell}, \quad \text{the } \textit{dirty limit}.
\end{aligned}$$

3.7.2 THE GINZBURG-LANDAU THEORY

In 1950 Ginzburg and Landau described the transition between the normal and superconducting phases. They proposed a macroscopic wave function of the superconducting carriers $\psi(x)$ that serves as an order parameter, where:

$$\psi(x) = |\psi| e^{i\phi(x)} \tag{129}$$

and $|\psi_0|^2 = n_s$ is the density of superconducting carriers, with $\psi \neq 0$ for $T < T_c$ and $\psi = 0$ otherwise [36].

By expanding the Gibbs free energy in powers of ψ and $\vec{\nabla}\psi$, we get an equation of ψ, analogous to the Schrödinger equation for a free particle [37], as:

$$\frac{1}{2m}\left(-i\hbar\vec{\nabla} + 2e\vec{A}\right)^2 \psi + \beta|\psi|^2\psi + \alpha\psi = 0, \tag{130}$$

where α and β are the expansion coefficients, m is the electronic mass, and $\vec{A}$ the vector potential. This accounted for the spatial variation of density of super electrons n_s, plus the nonlinear effects on it due to strong fields, features that were not explained before by the London theory. The penetration depth and the coherence length—as given by the Ginzburg-Landau theory—are:

$$\lambda = \sqrt{\frac{m\beta}{4\mu_0 e^2 |\alpha|}} \quad \text{and} \quad \xi_{\mathrm{GL}} = \frac{\hbar}{\sqrt{2m|\alpha|}}. \tag{131}$$

Finally, the so-called **Ginzburg-Landau parameter** is defined as the ratio of both $\kappa = \lambda/\xi_{\mathrm{GL}}$ and is the parameter that makes the distinction between the superconductors of Type-I ($\kappa \leq 1/\sqrt{2}$) and Type-II ($\kappa > 1/\sqrt{2}$).

$$\kappa = \sqrt{\frac{m^2\beta}{2\mu_0\hbar^2 e^2}}. \tag{132}$$

In Type-I superconductors, there is a critical field H_c, at which superconductivity can't be sustained and ψ quickly drops to zero in a first-order transition. In Type-II superconductors, instead of having a spontaneous breakdown of superconductivity, there is a continuos increase in the penetration of the magnetic field in the material, forming flux vortices. Then, for Type-II superconductors there are two critical fields B_{c1} and B_{c2}. Once B_{c1} has been reached, flux vortices start to form, the number of these vortices increases linearly with the external applied field, until B_{c2} is reached, then superconductivity abruptly breaks down.

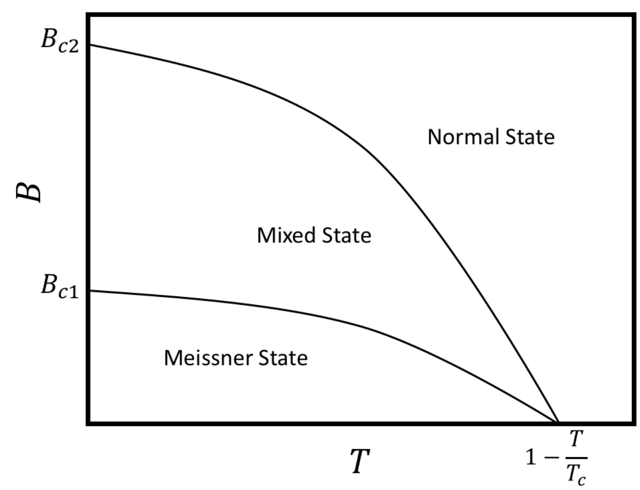

FIG. 28: Temperature dependance of the critical fields for a Type-II superconductor.

Figure 28 shows a relevant diagram for the discussion that will be presented in the experimental results section, since in this dissertation we will be referring particularly to bulk niobium cavities, being Nb a Type-II superconductor.

3.7.3 THE BARDEEN-COOPER-SCHRIEFFER THEORY

In 1955, John Bardeen suggested that, while in a superconducting state, $k_{\mathrm{B}}T_c$ was the necessary energy to excite an electron from the surface of the Fermi sea and that the excited electrons behave similarly to the electrons in the normal state [38]. In

1956, Leon Cooper described how the electrons could overcome the Coulomb's potential by interacting with phonons in the lattice to form weakly bounded pairs, known as **Cooper pairs**. The Cooper pairs, at low temperature, have lower energy than the two individual electrons that conform them [39]. One year after that, Bardeen, Cooper, and Schrieffer developed their (BCS) theory, assuming that the supercurrent was carried by the Cooper pairs rather than by single electrons. The Cooper pairs behave like a condensate (since they are boson-like quasiparticles, rather than fermions). Hence, all occupy a single quantum state, the **BCS ground state** [40].

The energy of the ground state is separated by the energy gap $E_g = 2\Delta(T)$ from the single electron states. Then, the critical temperature T_c is related to the zero temperature energy gap $\Delta(0)$ by the relation

$$1.76 k_B T_c = \Delta(0), \tag{133}$$

where k_{B} is the Boltzmann constant.

A handy way to characterise a conductor is by its surface impedance, in terms of the resistance R and the reactance X, it can be expressed as:

$$Z = R + iX, \tag{134}$$

with $R, X \in \Re$. Next, we can redefine the surface impedance in terms of the tangent fields at the surface as:

$$Z = i\frac{4\pi\omega}{c^2}\left[\frac{E_x}{(\partial E_x/\partial z)}\right]_{z=0}, \tag{135}$$

and following Ohm's law, we know that the normal current density is $J_n = \sigma E_0 e^{-i\omega t}$. The acceleration that the pairs receive, gives raise to a supercurrent density of

$$J_s = i\frac{2n_s e^2}{m\omega}E_0 e^{-i\omega t}, \tag{136}$$

and from this expression we can write the conductivity of the superconducting carriers as $\sigma_s = 1/(\lambda^2\omega\mu_0)$.

In this scheme, and explained before by the two fluids theory, DC currents flowing in the superconductor do not prevent the currents generated by normal electrons or the Cooper pairs. However, magnetic fields will penetrate the superconducting surface by λ and their time derivative will generate an electric field that will make the normal electrons oscillate, generating small currents that produce dissipation, contributing in this way to the overall surface resistance. Now, the total current density will be the sum of J_n and J_s, whereas the associated complex conductivity would be:

$$\sigma = \sigma_n + \sigma_s. \tag{137}$$

We can write the conductivity of a normal metal, following the Drude model, as:

$$\sigma_n = \frac{n_n e^2 \tau_n}{m} = \frac{n_n e^2 \ell}{m v_{\mathrm{F}}}, \tag{138}$$

where τ_n is the relaxation time of the electrons and v_{F} is the Fermi velocity. And, for normal conductors is true that $\tau_n \ll 1/\omega$, i. e. the relaxation time between collision is smaller than the rf period.

Then, from Eq. 134 we can write:

$$R_s = \frac{1}{2}\sigma_n \omega^2 \mu_0^2 \lambda_L^3 \tag{139}$$

and

$$X_s = \omega \mu_0 \lambda_L. \tag{140}$$

Thus, the conductivity of a normal metal depends on the energy gap $\Delta(T)$ and the thermal energy $k_B T$ [23] as:

$$\sigma_n \propto n_n \ell \propto \ell e^{-(\Delta(T)/k_B T)}. \tag{141}$$

Since the surface resistance is the real part of the complex surface impedance, we find that: $R_s = \frac{1}{\lambda} \cdot \frac{\sigma_n}{\sigma_n^2 + \sigma_s^2}$. As mentioned before, we will focus exclusively on bulk Nb cavities in this dissertation. Therefore, we can write an approximated expression of the BCS surface resistance for niobium as:

$$Rs \propto \lambda_L \left(1 + \frac{\xi}{\ell}\right)^{3/2} \omega^2 \ell e^{-(\Delta(T)/k_{\mathrm{B}} T)}. \tag{142}$$

Finally, the expression we will use is an approximation for $T < Tc/2$ and $\Delta \gg \hbar\omega$. Which, including a temperature independent parameter that depends on the surface preparation, called the residual surface resistance R_{res}, can be written as:

$$Rs \approx \frac{A}{T}\omega^2 e^{-\left(\frac{\Delta(T)}{k_{\mathrm{B}}}\right)} + R_{\mathrm{res}} = R_{\mathrm{BCS}} + R_{\mathrm{res}}. \tag{143}$$

There are many subtleties on the development of the different superconductivity theories mentioned above, as well as many important results that we did not mention. After all, superconductivity and its applications are growing fields with lots of problems that remain to be robustly modelled. We consider that this is a good point to finish with our brief theoretical review and to continue the discussion on other aspects of this dissertation.

CHAPTER 4

BEAM DYNAMICS

From the view point of beam dynamics, the implementation of crab cavities involves different challenges with complexities that depend (among other things) on the machine's lattice. There are different approaches one can take on the crossing angle correction using crab cavities. For instance, a **global** scheme uses crabbing at a single point of the machine (see Fig.29(a)), and the total crabbing angle can be built up turn by turn, allowing to lower the voltage per cavity as well as the total number of cavities. However, this scheme can considerably reduce the beam lifetime if it builds up resonant instabilities induced by harmonic excitations [20]. Further complications can derive from the fact that the global scheme requires that the bunches perform transverse oscillations, following the ring's betatron function on the crabbing plane along the machine. Careful studies of the dynamic beam-beam effects are necessary to avoid beam losses due to the crab cavities' physical apertures [41]. In contrast, a **local** crabbing scheme employs a set of crab cavities at each side of the interaction point, one set [before the interaction point] to induce the transverse bunch momentum and a second set [after the IP] to remove the induced transverse momentum after the collisions, locally confining the crabbing effects within the interaction region (see Fig.29(b)). However, a local scheme requires $n\pi/2$ horizontal betatron phase advances from the interaction point to the crab cavities on each side.

The present dissertation only considers the study of local crabbing, since it is the baseline scheme for the MEIC. In Section 4.1, the single turn maps for both the proton and the electron rings are presented, these descriptions include the interaction region as a section independent from the rest of the ring. Realistic phase advances, generated by sets of quadrupoles or Final Focusing Blocks [FFBs], between the crab cavities located in the expanded beam regions and the interaction point, are shown to differ slightly from $\pi/2$ in Section 4.2. To understand the effect of crabbing on the beam dynamics for the MEIC, propagation of Gaussian distributions of both electron and proton bunches were studied over multiple turns (1000 passes). In Section 4.3, this model was applied to determine linear-order dynamical effects of the synchro-betatron coupling induced by crabbing and phase advance "slipping". Section 4.4

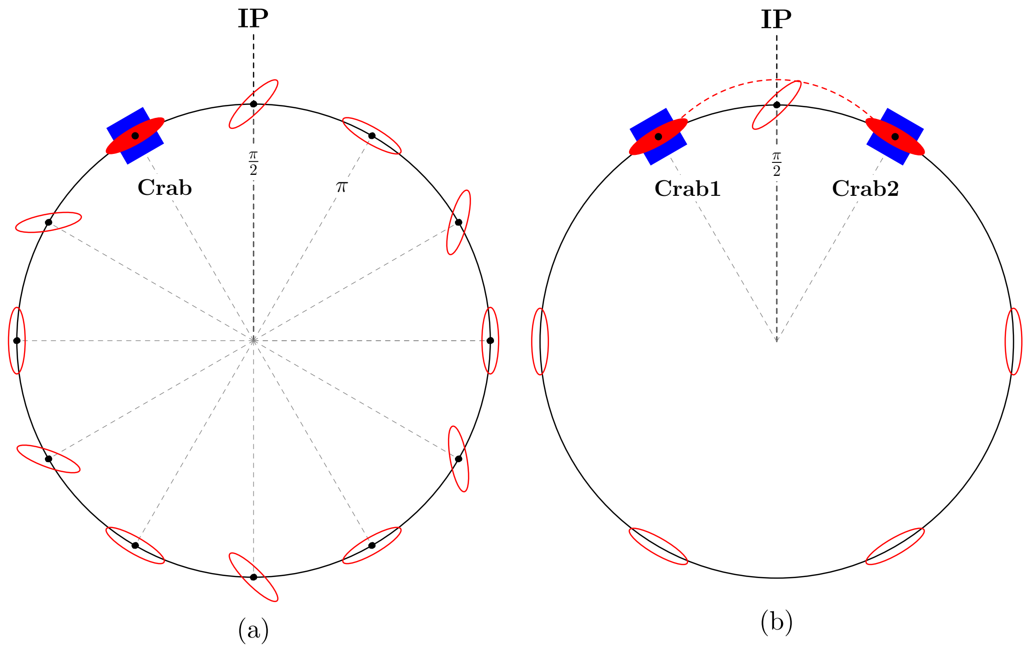

FIG. 29: *Cartoon* schematic of angle oscillations performed by the bunch for global (a) and local (b) crabbing correction in a ring.

presents studies, for the simplified case of a symmetric interaction region, the case in which the transverse coupling introduced to the bunches by the detector's solenoid is not locally compensated. In Section 4.4.1, the rotated vector basis parametrised to the solenoid strength is described. While Section 4.4.3 compares the simple horizontal crabbing kick with the effect of a crabbing kick rotated by the coupling [mixing] angle, set by the solenoid strength. Also, a general scheme for crabbing in an arbitrary direction is sketched in Section 4.4.4, using *twin* crab cavities optimized to compensate for the transverse coupling in the solenoid strength's range, this scheme could be particularly useful for machines with non-symmetrical interaction regions.

Lastly, Section 4.5 describes the considerations for modelling the lattice (using the proton ring as *case of study*) for particle tracking in `Elegant`, setting the crabbing kicks as thin multipole elements [42], and starting the simulations only with the pure dipole contributions and finally considering different non-zero values for the sextupole components as well, to infer limits of the higher order multipole content in the cavity fields that preserve the beam's lifetime.

4.1 LINEAR MODEL

Commonly in ring design studies, the equilibrium or closed orbit around the accelerator is approximated to a circle with a fixed radius, or in other words, only considers a machine made fully with pure dipoles and quadrupoles, then the transverse motion is treated as a perturbation expansion around the equilibrium orbit. That is to say, it uses a completely linear model. After this is done, it is possible to look into non-linear effects by adding higher contributions systematically. Analysing non-linear contributions is important, for example, to avoid higher order resonances that may raise undesirable dynamic conditions for the machine operations (i.e. beam filamentation, beam breakup, etc.). In a similar fashion in this section, the entire electron and proton storage rings 6D dynamics have been reduced to a simple linear map representation [21], separating the interaction region from the rest of the lattice (see Fig. 30). For this setup, we neglected any other higher order contribution in the lattice, to only have non-linearities from the crab cavities, further studies will have to consider the chromatic sextupoles, since they are the most important non-linear sources in a typical synchrotron lattice. Due to the high luminosity requirements imposed on the MEIC [8], stable beam operation while using crabbing correctors, is of a major importance, and for this reason we will add the next order (sextupolar) contribution of the crab cavities in a later section.

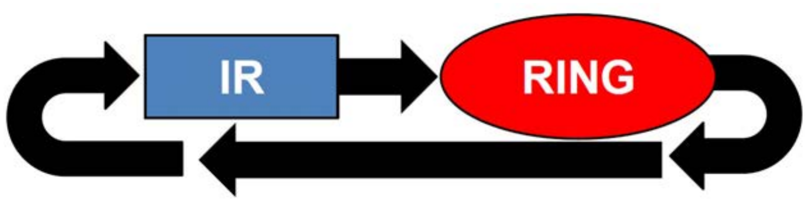

FIG. 30: Conceptual sketch of the interaction region (blue) connected on its extremes by a linear map of the ring (red).

The motion both transverse and longitudinal are—up to first order—decoupled, thus the ring's one turn map, without dispersion, is a block diagonal matrix as can be seen in Eq. 144. In the real lattice, due to local dispersion suppression at the interaction point, the crab cavity downstream will indeed see no dispersion, while the cavity upstream may see a dispersion up to the order of -0.04 m.

$$\mathbb{M}_{\mathrm{RING}} \equiv \begin{pmatrix} \left(\mathbb{M}_{\mathrm{x}}\right) & 0 & 0 \\ 0 & \left(\mathbb{M}_{\mathrm{y}}\right) & 0 \\ 0 & 0 & \left(\mathbb{M}_{\mathrm{z}}\right) \end{pmatrix}; \tag{144}$$

where, the transverse motion maps $\mathbb{M}_{\mathrm{x,y}}$ and the longitudinal motion map $\mathbb{M}_{\mathrm{z}}$ in terms of the Twiss parameters ($\alpha_{x/y}$ and $\beta_{x/y}$) and the phase advances ($\psi_{x/y} = 2\pi\nu_{x/y}$) are:

$$\mathbb{M}_{\mathrm{x}} \equiv \begin{pmatrix} \alpha_x \sin(\psi_x) + \cos(\psi_x) & \beta_x \sin(\psi_x) \\ \frac{(2\alpha_x)\cos(\psi_x)}{\beta_x} - \frac{\left(1-\alpha_x^2\right)\sin(\psi_x)}{\beta_x} & \alpha_x \sin(\psi_x) + \cos(\psi_x) \end{pmatrix}, \tag{145}$$

$$\mathbb{M}_{\mathrm{y}} \equiv \begin{pmatrix} \alpha_y \sin(\psi_y) + \cos(\psi_y) & \beta_y \sin(\psi_y) \\ \frac{(2\alpha_y)\cos(\psi_y)}{\beta_y} - \frac{\left(1-\alpha_y^2\right)\sin(\psi_y)}{\beta_y} & \alpha_y \sin(\psi_y) + \cos(\psi_y) \end{pmatrix}, \tag{146}$$

$$\mathbb{M}_{\mathrm{z}} \equiv \begin{pmatrix} \cos(2\pi\nu_s) & \frac{\sigma_z \sin(2\pi\nu_s)}{\sigma_{\delta p}} \\ -\frac{\sigma_{\delta p}\sin(2\pi\nu_s)}{\sigma_z} & \cos(2\pi\nu_s) \end{pmatrix}. \tag{147}$$

A simplified model, of a symmetric interaction region using linear elements in the thin lens approximation [14], such as *horizontal crab kickers*, *the quadrupole triplets known as "final focusing block" FFBs*, and *drifts*, was implemented for both electron and proton bunches (see Fig. 31(a)). A more realistic layout of the current MEIC interaction region can be seen in Fig. 31(b) [10], a highly non-symmetric interaction region like this could increase the complexity of certain calculations, for example in the presence of transverse coupling, but would not significantly change the general concepts presented.

4.1.1 BUNCH DISTRIBUTIONS

Analytical calculations, for the propagation of 6D Gaussian bunch distributions through the linear maps, were performed for 1000 passes using *Wolfram Mathematica®*, as a first step to study the linear effects on the beams due to implementation of zero-length linear crabbing kicks to account for a 50 mrad of total crossing angle (25 mrad per beam), in a local correction scheme. The parameters of the Gaussian distributions used for this calculations are listed in Table 1, while the lattice parameters are presented in Table 2.

(a)

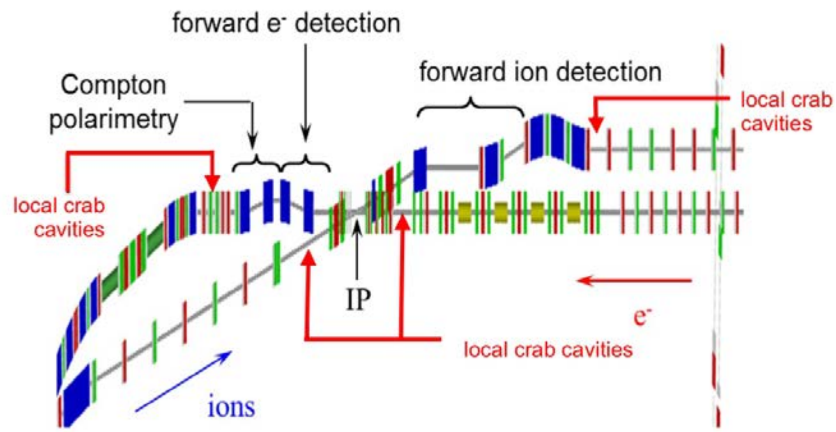

(b)

FIG. 31: Schematic drawings of the symmetric IR showing the 1st (**C1**) and 2nd (**C2**) crab cavity locations in red, the FFBs in blue, the connecting drifts, and the IP in yellow (a). Layout of the current MEIC IR (b).

4.2 RELATIVE PHASE ADVANCE

The relative phase advance ($\Delta\psi_{x,12}$) constraint for the crab cavities, in a local scheme, states that the bunch should describe an integer number of betatron half oscillations between the crab cavity locations (corresponding to C1 and C2 in Fig. 31) to ensure a complete cancellation of the transverse kick imprinted across the bunch by the first crab cavity (i.e. local crabbing). Any difference from $n\pi$ in this relative phase advance will cause mismatched conditions for the ring's optics and will contribute to other effects caused by errors on the crab cavities' voltages, rf phase noise, and particles' time of flight errors, among others.

In the present analysis, any effects induced by voltage, phase noise, or time of flight errors, are neglected by using a linear zero-length kick at the location of the first crab (C1) that would produce the desired crabbed angle at the interaction point, independently of the particle's momentum, and a similar kick at the location

TABLE 1: Parameters used for the particle's distributions

Parameter	**Electrons**	**Protons**	**Units**
Energy	5	60	GeV
Number of particles	10^5	10^5	–
$\epsilon_{N,x}$	54	0.35	μm
$\epsilon_{N,y}$	11	0.07	μm
$\sigma_{\Delta p/p}$	7.1	3.0	$\times 10^{-4}$
σ_z	0.75	1	cm

TABLE 2: Lattice parameters

Parameter	**Electrons**	**Units**
Horizontal fractional tune ν_x	0.73	–
Vertical fractional tune ν_y	0.32	–
Synchotron fractional tune ν_z	0.01	–
Crossing angle [per beam] $\theta_c/2$	25	mrad
Drift length D	7	m
FFB focal length F	7	m

of the second crab (C2) to cancel the crabbing effect. This linear kick will only accounts for the individual particle's longitudinal and horizontal positions with respect to the centroid of the bunch. The corresponding transfer matrix -in the base $(x,\ x',\ y,\ y', \Delta t,\ \Delta p/p)$- is shown in Eq. 148.

$$\mathbb{M}_{\text{Crab}} = \begin{pmatrix} 1 & 0 & 0 & 0 & 0 & 0 \\ 0 & 1 & 0 & 0 & \frac{V_c \tan\left(\frac{\theta_c}{2}\right)}{D} & 0 \\ 0 & 0 & 1 & 0 & 0 & 0 \\ 0 & 0 & 0 & 1 & 0 & 0 \\ 0 & 0 & 0 & 0 & 1 & 0 \\ \frac{V_c \tan\left(\frac{\theta_c}{2}\right)}{D} & 0 & 0 & 0 & 0 & 1 \end{pmatrix}, \tag{148}$$

where V_c is the crabbing voltage, θ_c the total crossing angle (50 mrad in this case), and D is the length of the drift placed between the crab cavity location and the IP (see Fig. 31(a)).

Remembering the standard algebra operations with matrices, we can calculate the total transfer matrix in the horizontal direction, from one crab cavity to the other, using:

$$\mathbb{M}_{\mathrm{x}} = \mathbb{M}_{\mathrm{FFB}} \cdot \mathbb{M}_{\mathrm{Drift}} \cdot \mathbb{M}_{\mathrm{Drift}} \cdot \mathbb{M}_{\mathrm{FFB}} = \begin{pmatrix} -\frac{D}{F} & 2D \\ 0 & -\frac{D}{F} \end{pmatrix}, \tag{149}$$

keeping in mind that $F = D$, according to Table 2.

Once having the total transfer matrix we can make a comparison element by element with the equivalent transfer matrix constructed by the standard Courant-Snyder parametrisation [14]. For example, the m_{12} element of Eq. 45, then:

$$\begin{aligned} m_{12} &= 2D \\ &= \sqrt{\beta_x^{C1}\beta_x^{C2}}\sin\left(\Delta\psi_{x,12}\right), \end{aligned} \tag{150}$$

where β_x^{C1} and β_x^{C2} are the horizontal β values at the first and second crab cavity locations (respectively), while D refers to the drifts' length as indicated in Fig. 31(a). Taking into account that the optimal location to place the cavities is as close to the FFBs as possible, the only way that Eq. 149 accounts for an exact value of $\Delta\psi_{x,12} = n\pi$ is for $\sqrt{\beta_x^{C1}\beta_x^{C2}} \to \infty$, for a desirable set-up of the crab cavities. Therefore, these relative phase advance differences are reduced as the length of the drifts is reduced or the $\sqrt{\beta_x}$ values are increased at the crab cavities' location. The calculations performed, using the lattice design for the MEIC proton storage ring [43], show a relative phase advance difference, between the two cavities, of $\sim 1\%$ with respect to π.

4.3 SYNCHRO-BETATRON COUPLING

A simple recurrent loop was implemented (using Wolfram Mathematica®) to propagate the 6D distributions described in Table 1 through the proper matrices' sequence (see Eq. 144). Special care was taken to store the evolution at several locations within the interaction region for each turn to monitor for the evolution of different effects. Figure 32(a) shows the electron bunch distributions at the interaction point for the uncrabbed initial distribution (blue), the distribution after 1000 turns without implementing the crabbing correctors (orange), and finally the bunch after 1000 turns with local crabbing on (green). Also, Fig. 32(b) shows the calculated crabbed angle per turn for the proton bunch with the crabbing correctors turned off (blue), and when the local crabbing correction is turned on (orange). The crabbed angle for the distribution is calculated using Eq. 151, taking the approximation for small angles.

$$\tan(\phi_{\text{crabbed}}) \sim \phi_{\text{crabbed}} = \frac{\langle \mathbf{xz} \rangle}{\langle \mathbf{z}^2 \rangle}, \tag{151}$$

where $\langle \cdots \rangle$ is the mean value of the distribution coordinates or their product in this case.

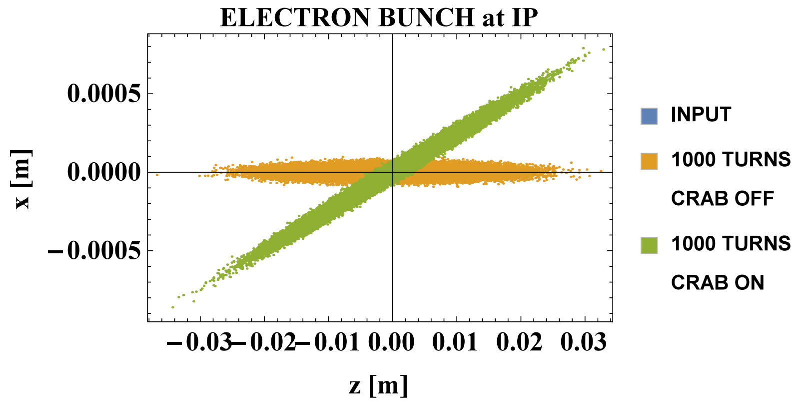

(a)

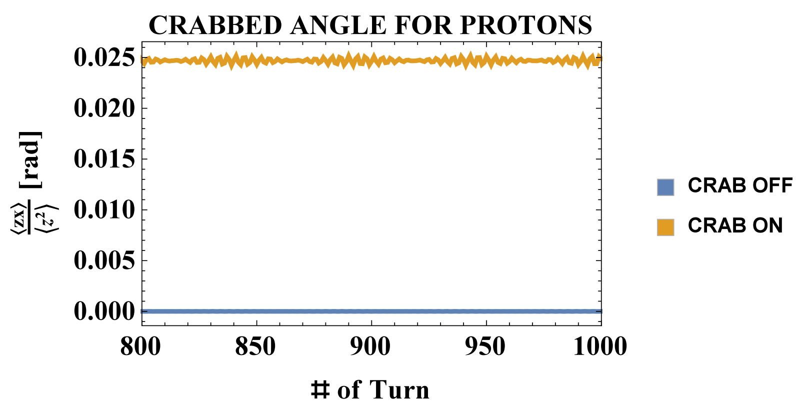

(b)

FIG. 32: Electron bunch at the IP (a), for the initial condition (blue), after 1000 turns without crabbing (orange), and after 1000 turns with crabbing (green). Calculated proton crabbed angle at IP (b) without crabbing (blue) and with crabbing (orange).

The noticeable periodicity of the effective crabbed angle is consistent with both the synchrotron and betatron oscillations. This effect is induced by a mismatching, given by the phase advance differences with respect to π between the crabs. Figure 33(a) shows the electron distribution at the C1 location, for the initial condition (blue), that is identical to—and therefore hidden by—the distribution after 1000 turns with the crabbing correctors off (orange), and after 1000 turns when the crabbing correctors are turned on (green). In a similar fashion Fig. 33(b) shows the same for the proton distribution at the C2 location, as a comparison of the similar effects induced by the phase advance differences with respect to π on the bunch orientations for both species. These effects do not show indications of resonances that consistently increase the beam sizes, at least at the linear order and for the small number of turns used to track the distributions, but they do produce synchro-betatron coupled oscillations due to the induced beam mismatch.

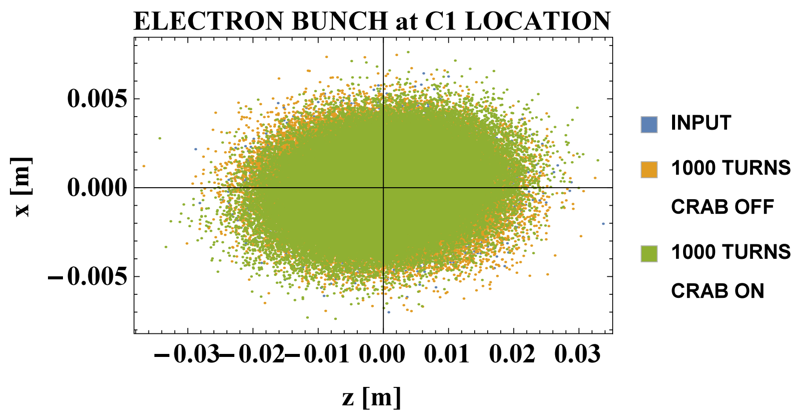

(a)

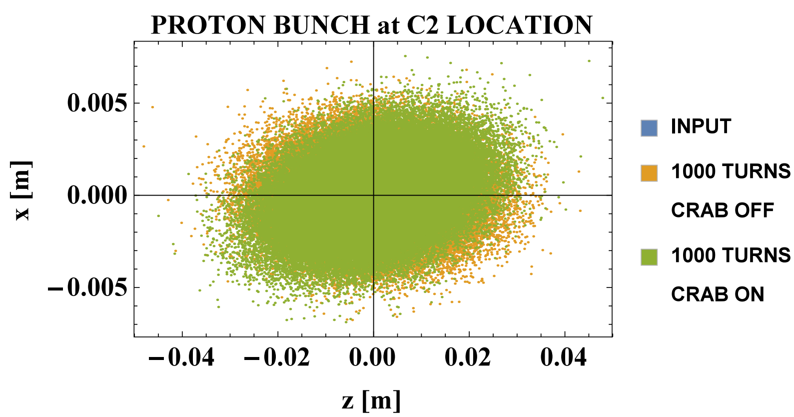

(b)

FIG. 33: Electron (a) and proton (b) distributions for the initial conditions (blue), after 1000 turns with no crabbing (orange), and after 1000 turns with the crabbing correctors turned on (green). The blue distributions are identical and therefore hidden under the orange ones.

The "snapshots" of the bunch distributions presented in Fig. 33 show the initial and final conditions after 1000 turns for the mentioned cases. However, the computed turn-by-turn beam sizes at different locations show the expected correspondence with the betatron oscillations for the case when the crabbing correctors are turned off.

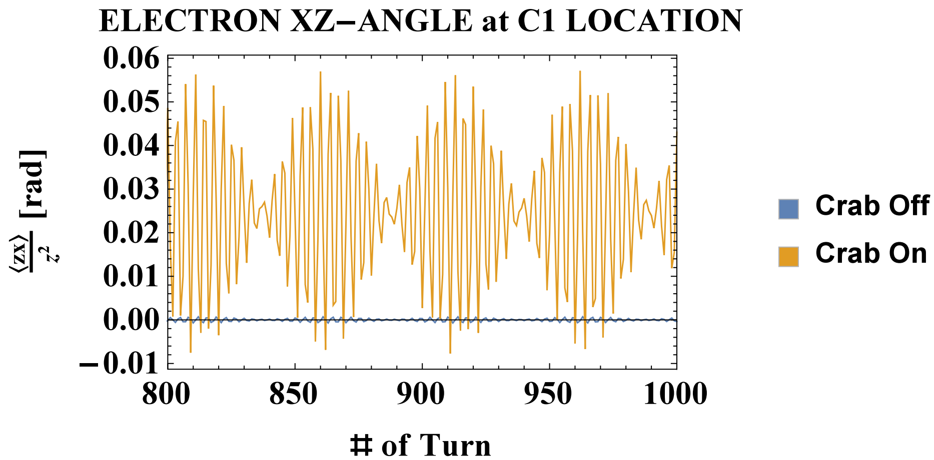

(a)

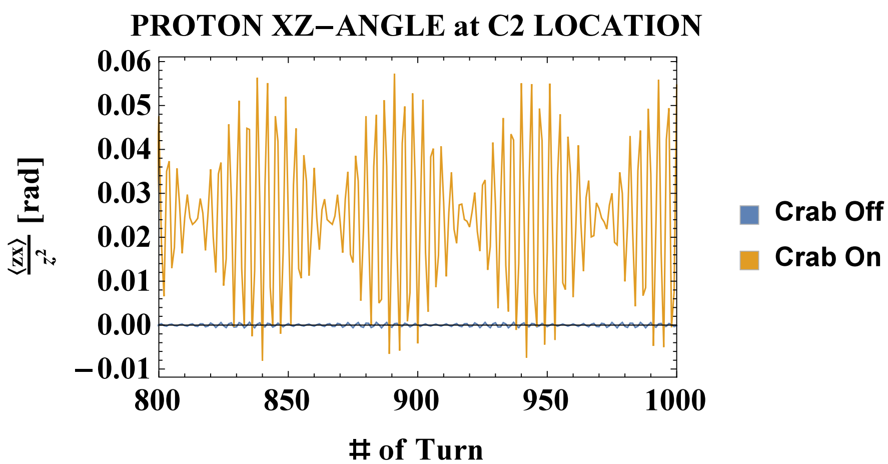

(b)

FIG. 34: Electron (a) and proton (b) x-z angle after 1000 turns, with no crabbing (blue) and after 1000 turns with the crabbing correctors turned on (orange).

Whereas for the case when the crabbing correctors are turned on, synchro-betatron coupling can be observed. Figure 34 shows the correlation of the the horizontal and longitudinal degrees of freedom for the bunch, when the crab cavities are turned off (in blue) and when the crab cavities are turned on (in orange). We can see that even with the crab cavities off, there is a small oscillation around zero on the blue lines, that corresponds to the fractional betatron tune. This oscillation is accentuated and convoluted with the synchrotron fractional tune when the crab cavities are turned on as described by the orange lines.

The transverse and longitudinal fractional tunes of the whole system are: $\nu_x =$

0.73, $\nu_y = 0.32$, and $\nu_z = 0.01$, respectively. A Fourier analysis of the beam size oscillations is presented in Fig. 35 as a function of the tune fraction, since the tunes used in the linear maps for both the electron and proton rings were the same, the Fourier analysis for each case gives the same result, with only slight differences in the amplitudes of the peaks and for this reason we do not make a special distinction between the results for electrons and protons, as the physical meaning of this phenomenon is independent from the bunch species (see Fig. 35(a) and (b)). We

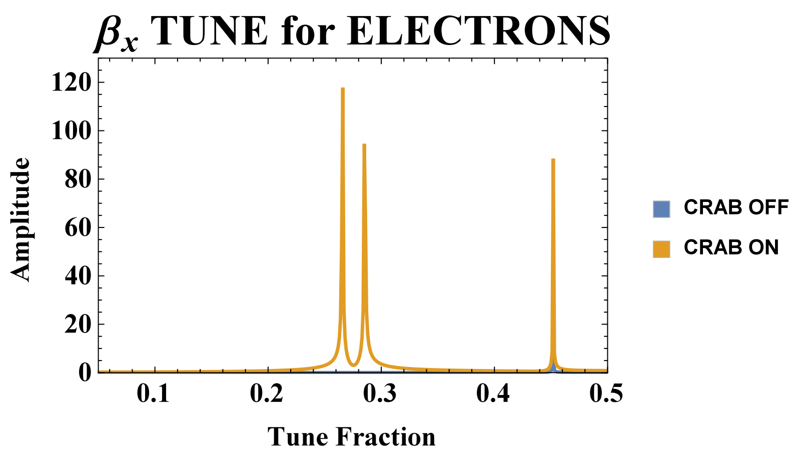

(a)

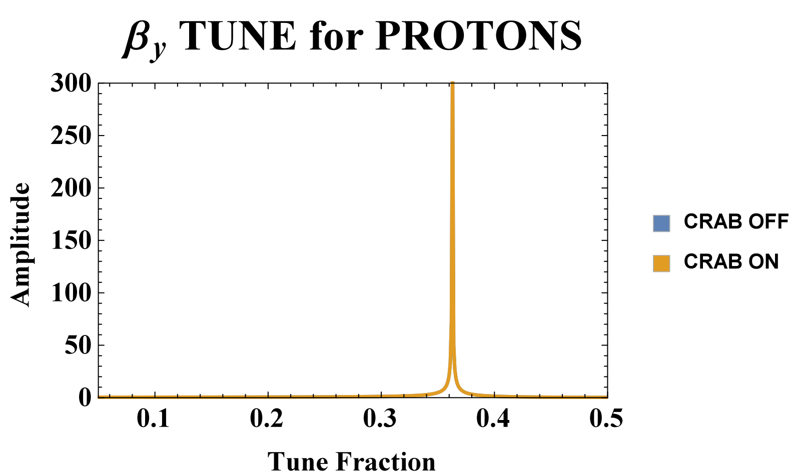

(b)

FIG. 35: Fourier analysis of the beams' horizontal (a) and vertical (b) β-functions, with the crabbing correctors off (blue) and on (orange).

can see in Fig. 35(b) a perfect match of the vertical fraction tune ν_y (actually shown as $2\nu_y - 1$ on the graph), for when the crabs are on or off, the blue line is exactly covered by the orange line. While in Fig. 35(a) we can distinguish, on the right, the horizontal fractional tune ν_x (actually shown as $2\nu_x - 1$ on the graph) with a smaller amplitude for when the crab cavities are off (first peak on the right), consistent to what is shown in Fig. 34 and, on the center, two side bands corresponding to $(\nu_x \mp \nu_z) - 1$. Also, there is a peak corresponding to the synchrotron fractional tune ν_z, too small to be appreciated on the plot. Figure 36 shows a close up of the graph when we can appreciate a peak at exactly $2\nu_z$, only for the case on which the crab cavities are turned on, showing again, a clear synchro-betatron coupling. The blue line is perfectly at a constant zero value, since there is no coupling with the synchrotron tune when the crab cavities are off.

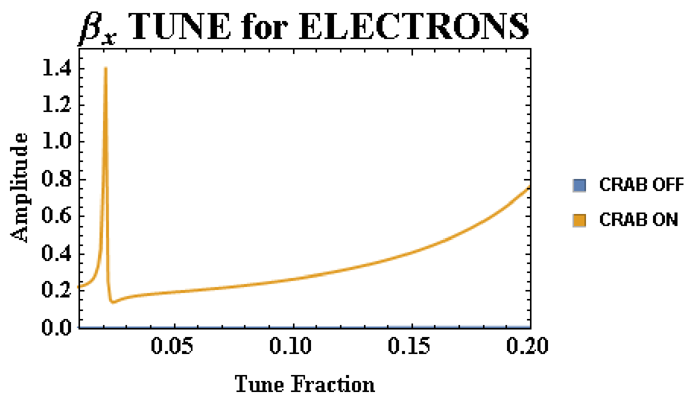

FIG. 36: Close up of the Fourier analysis of the β_x-functions, with the crabbing correctors off (blue) and on (orange).

4.3.1 ANALYTICAL APPROACH

The analytical linear models described in Section 4.1, were used to compare the beam dynamics in an electron-ion collider for the cases when perfect crabbing correctors are set to restore geometrical degradation of the luminosity due to a 50 mrad total crossing angle at the IP. Remember that Section 4.2 described the intrinsic difference of the relative horizontal phase advance [from π] between the crab cavities, which depends only on the interaction region's optics and the physical distance between the crab cavities [for the linear case]. Despite this difference being small, it can induce synchro-betatron coupling, showing 2 new sidebands $(\nu_x \pm \nu_z)$ in the horizontal betatron motion spectrum, as a result of a typical second order intermodulation between both x and z tunes (see Eq. 152 and 153). These effects do not give indications of resonances or emittance dilution for the range of (1000) turns studied. Further studies of this effects for longer number of turns are recommended to ensure stable operation conditions for the beams and to identify possible resonances.

$$\nu_{\text{signal}} = \mathcal{A}_x \nu_x + \mathcal{A}_z \nu_z \tag{152}$$

$$|\mathcal{A}_x| + |\mathcal{A}_z| = \mathcal{O}, \tag{153}$$

with $\mathcal{O} = 2$ in this case. It should be pointed out that other studies of coupling between transverse and longitudinal motion due to the action of crab cavities in the lattice, have been very recently carried out by other groups [44] in great mathematical depth, but with fundamental motivations that constitute a big difference with respect to case hereby discussed.

4.4 BUNCH TRANSVERSE COUPLING AND CRAB TWINNING

Due to spatial and technical restrictions of the MEIC lattice, high β regions with transverse coupled beams are being considered as locations for the crabbing cavity correctors [22]. In this section, simple analytical methods, similar to those previously described in the chapter, are used to evaluate the effects of a non-compensated solenoid field in the interaction region. By backtracking the bunches to the crabbing cavity locations, the proper kick's angle needed to produce the desired horizontal crossing orientation of the colliding bunches at the interaction point has been determined. A basic setup to account for the variable coupling in the crossing correction scheme to restore luminosity degradation in the machine is proposed. This setup involves the use of double (*twin*) crabbing cavities that can provide an effective variable angle kick within the needed range to compensate for the beam energy dependent transverse coupling. In other words, it is a system that could provide a crabbing kick in an arbitrary transverse direction.

4.4.1 TRANSVERSE BASIS ROTATION

For this part, only the linear effects of the solenoids [45], crabbing cavities and of the quadrupoles composing the final focusing blocks [46] are considered. We use the following notation in the transfer matrix [14]: with F as the final focusing block's focal length, D the drift length, $C \equiv \cos(KL)$, $S \equiv \sin(KL)$, $K \equiv \frac{qB_{Sol}}{2P}$, where q is the particle's charge, B_{Sol} the solenoid magnetic induction, P the particle's momentum, and L the solenoid length.

The transfer matrix correspondent to the *first-half* of the interaction region (IR1), this is to say, from the crabbing cavity location towards the interaction point with the crabbing kicker off, can be written as in Eq. 173:

$$\mathbb{M}_{\mathrm{IR1}} = \mathbb{M}_{\mathrm{SOL}} \cdot \mathbb{M}_{\mathrm{L}} \cdot \mathbb{M}_{\mathrm{FFB}}; \tag{154}$$

where $\mathbb{M}_{\mathrm{SOL}}$, $\mathbb{M}_{\mathrm{L}}$, and $\mathbb{M}_{\mathrm{FFB}}$ represent the thin-like lens transfer matrices for the solenoid, drift, and final focusing block respectively. With the basis of the transverse coordinates at the interaction point given by: $\hat{x}^T = (1, 0, 0, 0, 0, 0)$ and $\hat{y}^T = (0, 0, 1, 0, 0, 0)$.

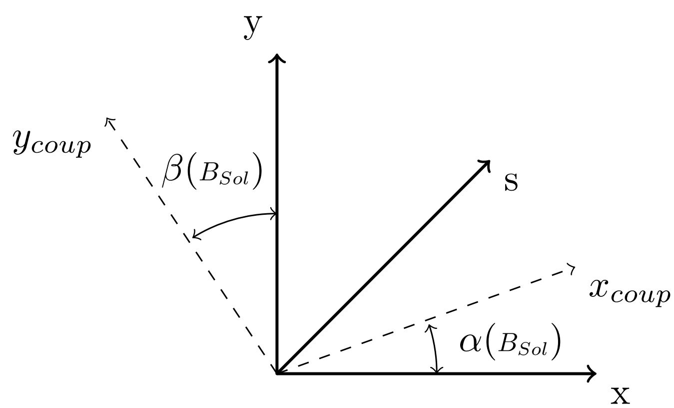

FIG. 37: Transverse coordinate basis at the IP (solid) and coupled transverse coordinate basis at the crabbing cavity position (dashed), where B_{Sol} is the solenoid field strength.

Strictly speaking, to split the solenoid, one would have to take into account the up and down fringe field contributions—$\mathbb{M}_{\mathrm{up}}$ and $\mathbb{M}_{\mathrm{dn}}$, repectively—following Conte and MacKay's Eq. 4.75 to 4.77 in [12]. Alternatively, we can also obtain a section of the interaction region, up to the first part of the solenoid, by multiplying $\mathbb{M}_{\mathrm{S}} = \mathbb{M}_{\mathrm{up}} \cdot \mathbb{M}_{\mathrm{IR1}}$) since the fringe field contributions at the end of the section—$\mathbb{M}_{\mathrm{up}}$ and $\mathbb{M}_{\mathrm{dn}}$—will cancel each other out. Then, to back propagate the IP's transverse coordinate basis towards the crabbing cavity position, a new set of transverse coordinates at the location of the crabbing cavity ($\hat{x}_{coup}$, $\hat{y}_{coup}$) was defined as a linear transformation of the original transverse basis at the interaction point (See Fig. 37). The longitudinal coordinates were treated as fully independent.

$$\begin{Bmatrix} \hat{x}_{coup} \\ \hat{y}_{coup} \end{Bmatrix} = \mathbb{M}_{\mathrm{IR1}}^{-1} \cdot \mathbb{M}_{\mathrm{up}} \begin{Bmatrix} \hat{x} \\ \hat{y} \end{Bmatrix}, \tag{155}$$

While the transfer matrix—considering a full solenoid—can be written as:

$$\mathbb{M}_{\mathrm{IR1}}^{-1} =$$

$$\begin{pmatrix} C(C-DKS) & -\frac{C^2(DK+T)}{K} & S(DKS-C) & \frac{S(DKC+S)}{K} & 0 & 0 \\ \frac{C(C+(F-D)KS)}{F} & -\frac{C^2((D-F)K+T)}{FK} & -\frac{S(C+(F-D)KS)}{F} & \frac{S((D-F)KC+S)}{FK} & 0 & 0 \\ S(C-DKS) & -\frac{S(DKC+S)}{K} & C(C-DKS) & -\frac{C^2(DK+T)}{K} & 0 & 0 \\ \frac{S(C+(F-D)KS)}{F} & -\frac{S((D-F)KC+S)}{FK} & \frac{C(C+(F-D)KS)}{F} & -\frac{C^2((D-F)K+T)}{FK} & 0 & 0 \\ 0 & 0 & 0 & 0 & 1 & 0 \\ 0 & 0 & 0 & 0 & 0 & 1 \end{pmatrix},$$

where with $T \equiv \tan(KL)$. Plugging this into Eq. 155, we get:

$$\begin{aligned} \hat{x}_{coup}^T &= (C(C-DKS), x'_x, S(C-DKS), y'_x, 0, 0), \\ \hat{y}_{coup}^T &= \big(-S(C-DKS), x'_y, C(C-DKS), y'_y, 0, 0\big). \end{aligned}$$

Once again using this result and the diagram of Fig. 37, the horizontal and vertical angles can be written as in Eq. 156.

$$\begin{aligned} \tan\left(\alpha\left(B_{Sol}\right)\right) &= \frac{S(C-DKS)}{C(C-DKS)} = \tan\left(\beta\left(B_{Sol}\right)\right) = T. \\ \therefore \alpha\left(B_{Sol}\right) &= \beta\left(B_{Sol}\right) = \phi_{Sol} = KL. \end{aligned} \tag{156}$$

4.4.2 MIXING ANGLE (ϕ_{SOL})

As mentioned previously, in this section (Section 4.4), a slightly more complex scheme is taken into account, where the interaction region includes a solenoid that is part of the detection system and the upstream/downstream regions are asymmetrical for both the electrons and protons, as can be noted in the diagrams of Fig. 38.

One could use as a way to visualize the effects of the coupling induced to the bunches by the solenoid, calculating the mixing angle at the location of the crab cavities by back-propagating the distributions as explained early in this section in Eq. 155. Figure 39 shows the analysis of the behavior of this mixing angle $\phi_{Sol} = KL$, both for the electrons (with parameters: $P_e = 5$ GeV, $D_e = 4$ m, $F_e = 7$ m, and $L_e = 3$ m) and protons (with parameters: $P_p = 60$ GeV, $D_p = 5$ m, $F_p = 7$ m, and $L_p = 2$ m), as a function of the solenoid's field B_{Sol} and taking into account the upstream and downstream asymmetry of the interaction point [46] as previously discussed.

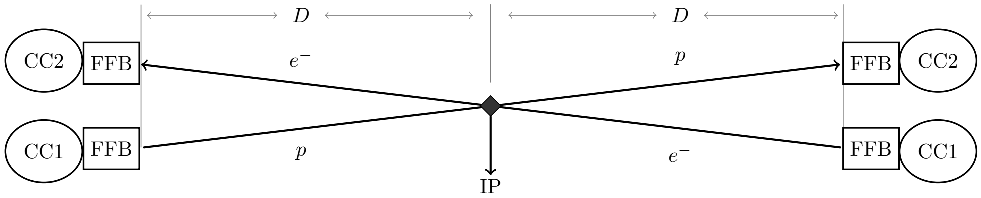

(a)

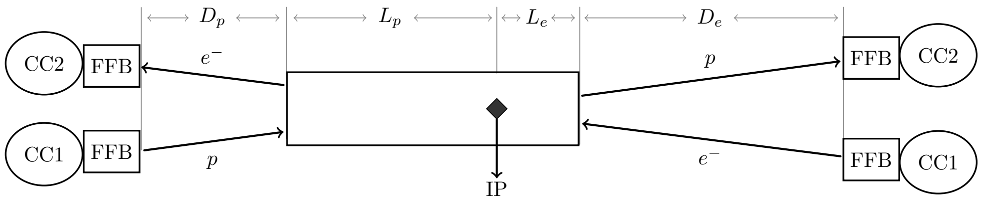

(b)

FIG. 38: Comparison of the symmetrical IR without solenoid (a), and the asymmetrical IR with a solenoid of length $L_{Sol} = L_e + L_p$ (b).

Examples of the coupled transverse distributions both for electrons and protons for several values of B_{Sol} are presented in Fig. 40 and 41 respectively.

4.4.3 ROTATED CRABBING CAVITY SOLUTION

Since the experiments would like to run at different solenoid strengths, to reduce systematic errors, only a crabbing cavity rotated by KL about the z axis ($\mathbb{M}_{\mathrm{C},\Sigma}$) [14], could always give a kick in the “correct” direction at the crabbing cavity location to produce the desired crabbed distributions at the interaction point. The transfer matrix for such a rotated crabber can be seen in Eq. 157.

$$\begin{aligned} &\mathbb{M}_{\mathrm{C},\Sigma} = \mathbb{R}(-KL)\,\mathbb{M}_{\mathrm{C}}\,\mathbb{R}(KL)\,, \\ \Rightarrow\ &\mathbb{M}_{\mathrm{C},\Sigma} = \begin{pmatrix} 1 & 0 & 0 & 0 & 0 & 0 \\ 0 & 1 & 0 & 0 & \frac{C\tan(\phi)}{F} & 0 \\ 0 & 0 & 1 & 0 & 0 & 0 \\ 0 & 0 & 0 & 1 & \frac{S\tan(\phi)}{F} & 0 \\ 0 & 0 & 0 & 0 & 1 & 0 \\ \frac{C\tan(\phi)}{F} & 0 & \frac{S\tan(\phi)}{F} & 0 & 0 & 1 \end{pmatrix}, \end{aligned} \tag{157}$$

where the crabbing angle [per beam] in the MEIC is $\phi = \theta_{\mathrm{C}}/2 = 25$ mrad. Then, we used this and Eq. 173 and 157 to find the total transfer matrix as $\mathbb{M}_{\mathrm{C\Sigma T}} = \mathbb{M}_{\mathrm{IR1}}\mathbb{M}_{\mathrm{C},\Sigma}$.

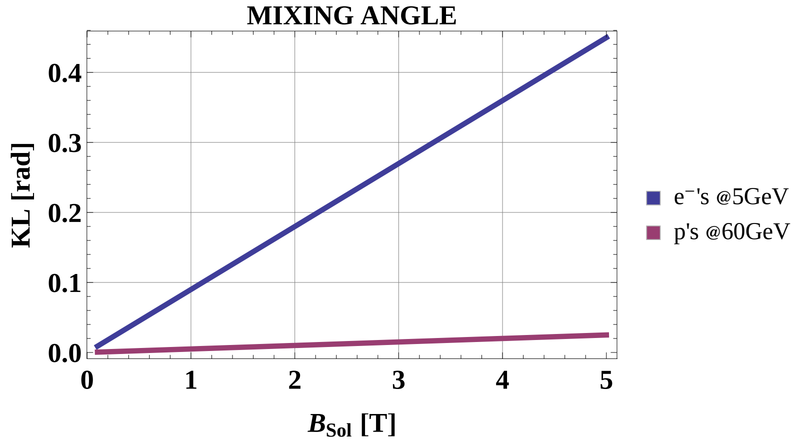

FIG. 39: Magnitude of KL in radians for electrons (blue) and protons (purple) at the position of the crabber.

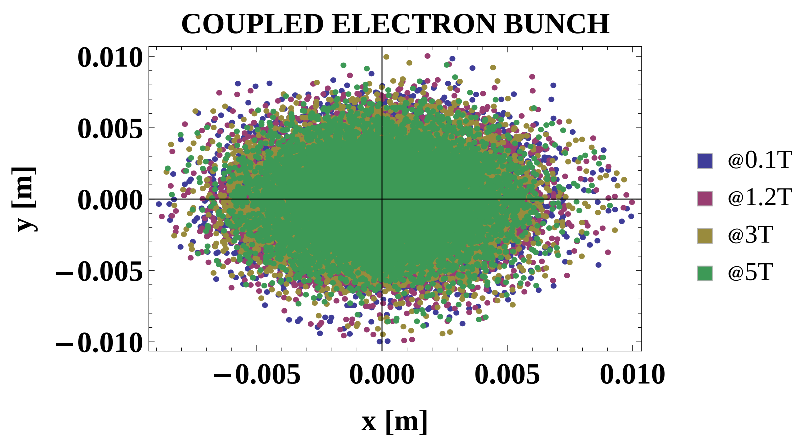

FIG. 40: Electron distributions at the crabber location for different B_{Sol} at 5 GeV.

In order to compare the solutions given by the rotated crabbing cavity—for different solenoid strengths B_{Sol}—with the case with no solenoid and fully horizontal crabbing, the distributions propagated through $\mathbb{M}_{\mathrm{C\Sigma T}}$ to the interaction point are presented in Fig. 42(a) and (b), for electrons and protons respectively.

Using for the electrons: $P_e = 5$ GeV, $D_e = 4$ m, and $L_e = 3$ m; and for protons: $P_p = 60$ GeV, $D_p = 5$ m, and $L_p = 2$ m, with $F = 7$ m—in both cases—as shown in Fig. 38. By plotting the crabbing angle as a function of B_{Sol} (see Fig. 43), it is possible to evaluate the maximum error in the crabbing angle due to additional solenoid focusing as $\sim 7\%$ for electrons and $< 0.1\%$ for protons in the studied range

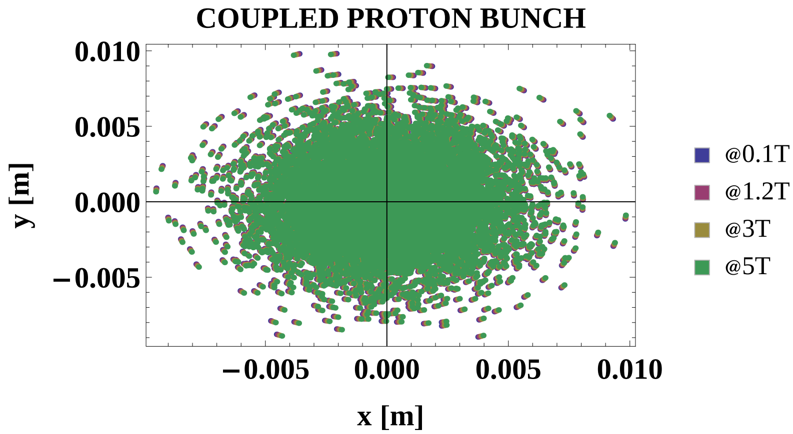

FIG. 41: Proton distributions at the crabber location for different B_{Sol} at 60 GeV.

for B_{Sol}. This extra focusing will be compensated by graduating the currents in the FFB's quadrupoles.

4.4.4 TWINNING THE CRABBERS

As a final step for this section, an array of 2 *twin* cavities ($\vec{C}_{x1}$ and $\vec{C}_{x2}$) was studied. The superposition of these *twin* cavities simulates a crabbing kick $\vec{C}_{\Sigma} = \vec{C}_{x1} + \vec{C}_{x2}$, with a variable angle (ϕ_{Sol}) that will account for the transverse coupling of the beams. Then, using Fig. 44 and the law of cosines [47] we can write down the effective kick as:

$$\begin{aligned}\vec{\mathrm{C}}_{\Sigma} =& [C_{x1}\cos(\phi_{Sol} - \alpha_{x1}) + C_{x2}\cos(\alpha_{x2} - \phi_{Sol})] \\ & \times [\cos(\phi_{Sol})\hat{x} + \sin(\phi_{Sol})\hat{y}],\end{aligned} \tag{158}$$

Fig. 45 shows how when optimising to lower the individual voltage needed from the *twins* C_{x1} and C_{x2} (Fig. 45 l.h.s.) to obtain the desired kick, the *twins* are found to be parallel, thus the angular coverage collapses to a single coupling angle ϕ_{Sol}, which corresponds to the traditional crabbing concept. And, when optimising for a maximum angular coverage (Fig. 45 r.h.s.), we lose balance of the voltage contribution for the cavities. This trade off needs to be considered to find the optimal angle θ_{twin} that balances the *twins*' voltage contributions for the needed angular range ($\phi_{Sol} = KL$) in the machine.

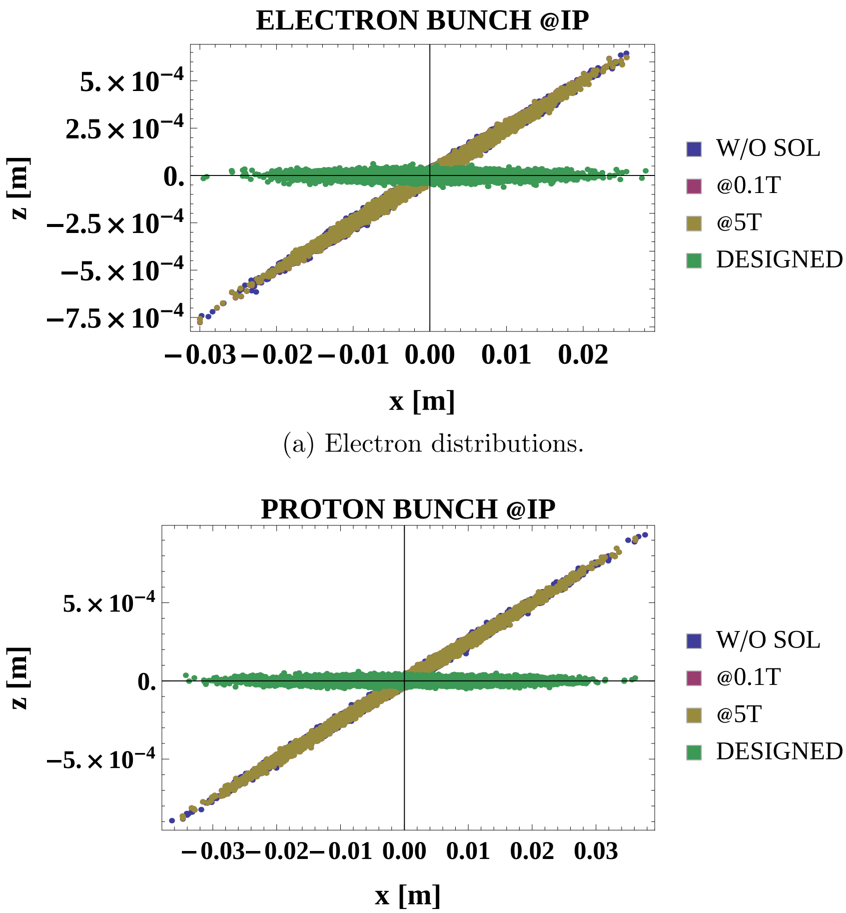

(a) Electron distributions.

(b) Proton distributions.

FIG. 42: Distributions at the IP for different B_{Sol}, using a crabber rotated by an angle of KL, compared to the case w/o solenoid (blue) and w/o both the crabbing cavity or solenoid (green).

4.5 PARTICLE TRACKING

The studies performed in the present dissertation use the former MEIC baseline frequency of 750 MHz to analyse the effects of the sextupole component of the rf kick given by such a cavity on the proton bunches at 60 GeV as a case study, even when the baseline frequency of collision has changed [10], the methods developed here can be easily implemented for different beam energies and frequencies without major difficulties, once the proper lattice updates have been done.

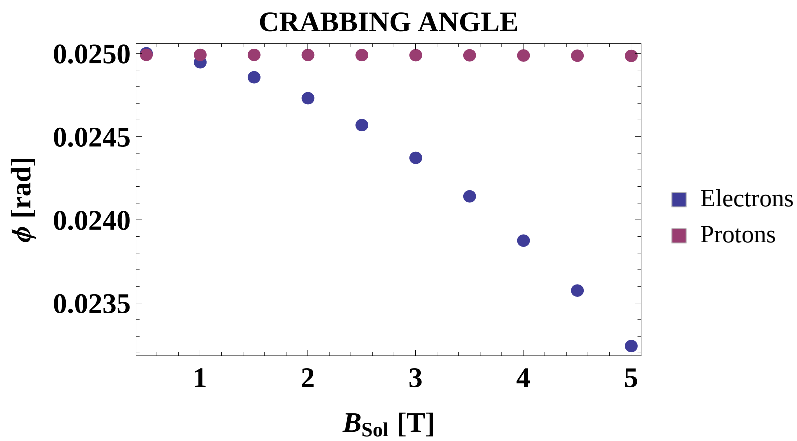

FIG. 43: Total crabbing angle at the IP (ϕ) for electrons (blue) and protons (purple) as a function of the B_{Sol}.

4.5.1 MULTIPOLES AND EMITTANCE

By treating the horizontal crabbing of the bunch as a *chirp* in x, it is possible to express the change in emittance due to this *chirp* [3] as:

$$\frac{\Delta\epsilon_x}{\epsilon_x} = \frac{\sqrt{\sigma_{x'}^2 + \sigma_{\Delta x'}^2}}{\sigma_{x'}^2} - 1. \tag{159}$$

Using a definition of the thin-lens rf multipole transverse kick, such as:

$$\begin{aligned} \Delta x' &= \frac{\Delta p_x}{p_z} \\ &\approx \mathcal{V}_0 \left(b_1 + b_3 \left(x^2 - y^2\right) + ...\right) \cos(\phi_{\rm rf}), \end{aligned} \tag{160}$$

where x is the horizontal coordinate, $\mathcal{V}_0 \equiv \frac{eV_x}{p_z mc^2 k}$: with V_x as the total crabbing voltage, p_z the particle momentum, the wave number $k = \frac{\omega_{rf}}{\beta c}$, b_1 and b_3 are the dipole and sextupole coefficients respectively and $\phi_{\rm rf} = 270^o$ as the rf phase with respect to the bunch centroid.

Then, one can write in these terms:

$$\sigma_{\Delta x'} \approx \frac{\mathcal{V}_0 b_3}{2}\sqrt{\sigma_{x^2}^2 + \sigma_{y^2}^2}, \tag{161}$$

thus, using Eq. 159 and 161 in this notation, the change of emittance per turn can be expressed as follows:

$$\frac{\Delta\epsilon_x}{\epsilon_x} = \frac{\sqrt{\sigma_{x'}^2 + \frac{\mathcal{V}_0^2 b_3^2}{4}\left(\sigma_{x^2}^2 + \sigma_{y^2}^2\right)}}{\sigma_{x'}} - 1. \tag{162}$$

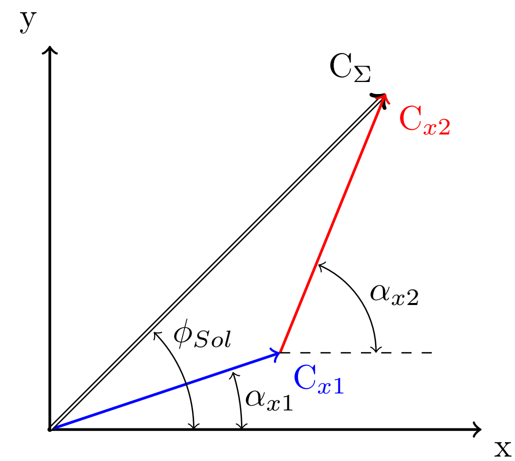

FIG. 44: *Twin* crabbing kicks $\vec{C}_{x1}$ (blue), and $\vec{C}_{x2}$ (red) with α_{x1} and α_{x2}, respectively, and the total kick $\vec{C}_\Sigma = \vec{C}_{x1} + \vec{C}_{x2}$ (double lined), with a variable angle ϕ_{Sol}.

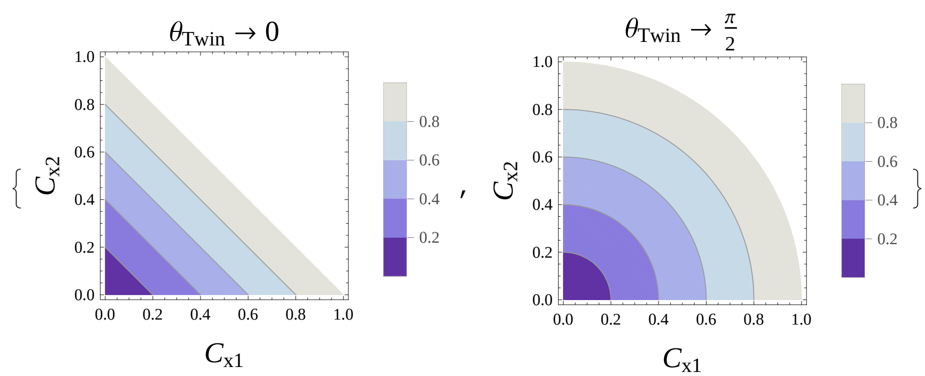

FIG. 45: $|\hat{C}_\Sigma|$ as a function of both *twins*' normalised amplitudes C_{x1} and C_{x2}, for the two extreme values of their relative angle $\theta_{twin} \equiv \alpha_{x2} - \alpha_{x1} = 0$ and $\theta_{twin} = \frac{\pi}{2}$.

This shows that the change in the emittance will depend on the transverse second momenta of the bunches and the sextupole component. In other words, Eq. 162 tells how geometrically the sextupole content on the crabbing kicks may have repercussions on the beam luminosity or even limit the beam lifetime. For this reason, in this section the case with a pure dipole kick is compared to the case, where there is also a sextupole component to the rf kick, in order to look for possible resonances or relative stability conditions for the crab cavities' operation.

4.5.2 TRACKING METHODS

We first describe the simplifications made to the lattice to focus our numerical studies on the interaction region, proposing a linear map for the proton storage ring that properly accounts for the transverse and longitudinal dynamics of the machine, leaving the full description of the interaction region as a separate block. Secondly, we present a discussion of the tracking elements and basic calculations performed at different locations of the interaction region.

As previously mentioned, linear maps were used for the 6D dynamics of the entire proton storage ring, excluding the interaction region, as seen in the schematic drawing on Fig. 30, while the elements that conform the interaction region and its associated transverse Twiss functions are described in Fig. 46. A small script was written in PYTHON to translate the rings lattice from the MAD-X files created by V. Morozov, as part of the MEIC design studies, to a transfer matrix with a suitable format for `Elegant`.

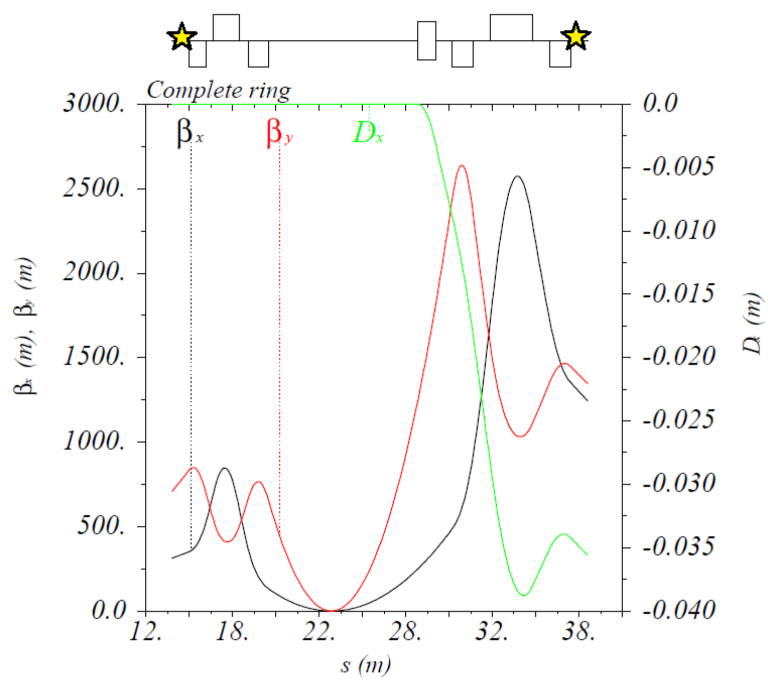

FIG. 46: Interaction region optics of the proton ring, where the yellow stars represent the crab cavity locations.

All the 6D phase space tracking was done using `Elegant`, the linear map was placed at the end of the interaction region as described in Fig. 30 and 46. The final focusing blocks at each side of the interaction point were described using elements such as QUAD, CSBEND, and DRIFT [42]. While for the crab cavities, zero-length multipole rf kicker (MRFDF) elements at zero crossing phase ($\phi_{\text{rf}} = 270^o$) were implemented. In this way and for the purpose of the present study, the number of non-linear contributions was reduced to isolate the effects of the higher order multipole contents of the cavities.

A uniform ellipse distribution of protons with the parameters described in Table. 3 were tracked for 1000 turns.

TABLE 3: Parameters of the employed proton distribution

Parameter	**Value**	**Units**
Central momentum	60	GeV
Number of particles	10^4	–
$\epsilon_{N,x}$	0.35	mm-mrad
$\epsilon_{N,y}$	0.07	mm-mrad
$\sigma_{\Delta p/p}$	3.0×10^{-4}	–
σ_s	10^{-2}	m

The linear map for the longitudinal dynamics was constructed by following [21], with a fractional synchrotron tune of $\nu_s = 0.01$. Fig. 47(a) shows the longitudinal phase space coming out of the interaction region for the last 20 of 1000 turns of the lattice without the crab cavities being turned on.

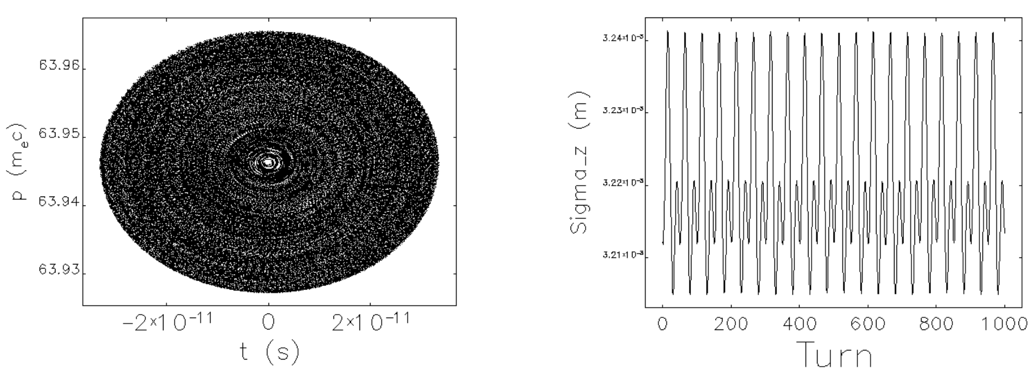

(a) (b)

FIG. 47: Longitudinal phase space, plotted for the last 20 of a 1000 turns without crab cavities (a) and longitudinal beam size showing oscillations in the order of the numerical errors (b).

4.5.3 PURE DIPOLE CASE

To analyse the effects on the bunches due to the higher order contents of the crab cavity fields, the present study started by setting the corresponding value of the normalised voltage amplitude $\mathcal{V}_{0,C1}$, for the zero-length dipole kick at the first cavity location to crab horizontally the bunch at the interaction point by 25 mrad, without any higher order multipole contribution. Another zero-length dipole kick was set at the second crab cavity location with a normalised amplitude of $\mathcal{V}_{0,C2} = \sqrt{\frac{\beta_x^{C1}}{\beta_x^{C2}}}\mathcal{V}_{0,C1}$ [14], which would completely cancel the effects of the first crab on the bunch, only for the case of bunches arriving with an exact $n\pi$ phase advance between the crab cavities. In this case, β_x^{C1} and β_x^{C2} are the horizontal beta functions at the locations of the first and second crab cavities, respectively. Any multipole contribution, higher than the dipole, was set to zero for this first step of the work.

After ensuring the conditions above described, the particles were tracked for 1000 turns, Fig. 48(a) shows the crabbed bunch at the interaction point location for the last 3 of the 1000 turns. While Fig. 48(b) shows the effective crabbed angle for each of the 1000 turns, calculated using Eq. 163,

$$\tan(\theta_c) \approx \theta_c = \frac{\langle xz \rangle}{\langle z^2 \rangle} = \frac{\langle xt \rangle}{\beta c \langle t^2 \rangle}. \tag{163}$$

It can be noted from Fig. 48(b) how the effective crabbed angle of the bunches at

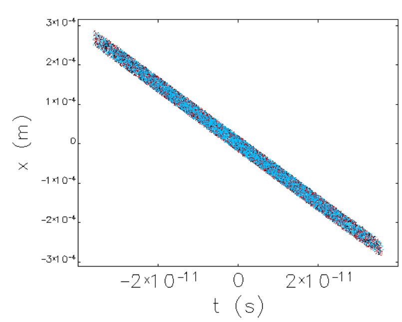

(a)

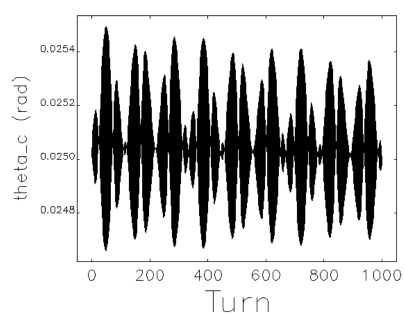

(b)

FIG. 48: Crabbed 60 GeV proton bunches at IP (a) and calculated crabbed angle (b), using a pure dipole contribution from the rf cavities.

the interaction point (tagged as "*theta_c*" on the plot) oscillates around the desired value turn-by-turn, by roughly ± 0.5 mrad with different convoluted frequencies. This is due to both synchro-betatron motions and small relative phase advance errors between the crab cavities, as discussed in Section 4.3 and Section 4.2.

The behavior of the transverse and longitudinal beam sizes as a function of the number of turns, gives an insight to the ϕ [or *theta_c*] variations at the interaction point. From Fig. 49(a), (b), and (c) can be noted the associated betatron and synchrotron oscillations of the bunch, and from (d) one could observe how a residual x-z angle at the location of the first crab will translate in an error of the total crabbed angle at the interaction point, this residual error appears to be stable for the studied range (1000 turns) for the case of pure dipole rf kick and could presumably be accounted for an exchange of horizontal and longitudinal emittances (compared with Fig. 47(b)). However, more detailed studies need to be performed to determine the real scope of these effects and their range of stability, which would establish important criteria for the high luminosity operation of the machine and eventually for the beam lifetime as well.

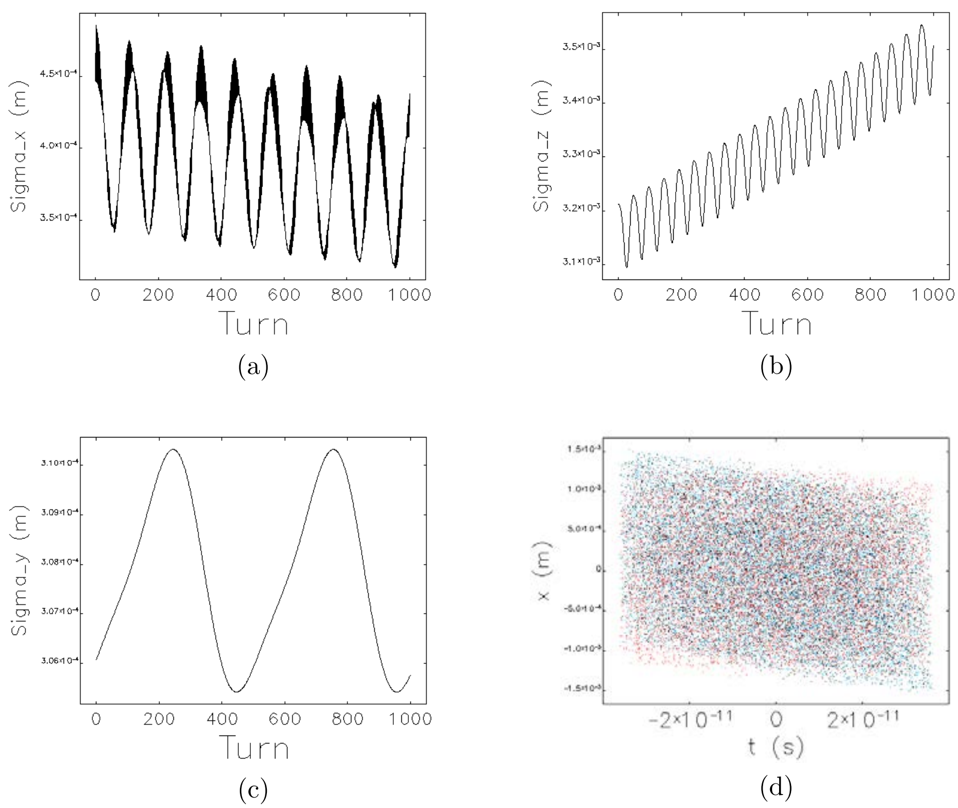

FIG. 49: Beam sizes for x (a), z (b), and y (c) for the case of a pure dipole rf kick. (d) shows a residual x-z angle of the bunch at the entrance of the first cavity.

4.5.4 ADDING A SEXTUPOLE CONTRIBUTION

For this case, a contribution consistent with the characteristic range of the sextupole strength for the 750 MHz rf dipole [at the operating voltage] was added to the thin multipole [48] and then calculated the crabbed angle at the interaction point, along with the beam sizes at the first crab cavity location for 1000 turns (see Fig. 50).

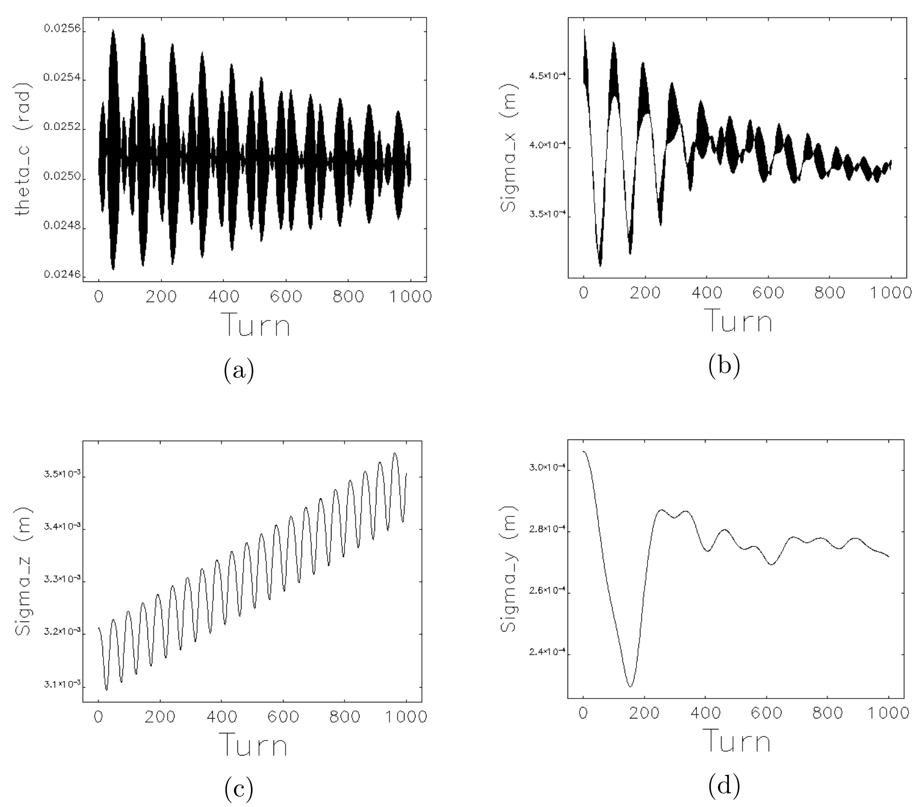

FIG. 50: For the case of a small sextupole contribution: the crabbed angle at IP (a), the longitudinal beam size (growing at similar rate than for the pure dipole case) (c), and both horizontal and vertical beam sizes (b) and (d), respectively.

From Fig. 50(a), a noticeable damping of the amplitude of the crabbed angle variation after 1000 turns compared to Fig. 48(b) can be observed, as well as variations of the transverse and longitudinal beam sizes (b), (c), and (d) with the difference that with the introduction of a non-linear (sextupole) contribution, both transverse beam sizes seem to be involved in the emittance exchange process. It is apparent that the relative stability for the case of pure dipole contributions and the case of including a small sextupole contribution to the crabbing rf kicks, for the range studied (1000 turns), does not change radically. However, it is important to perform detailed studies of these effects to avoid resonances that could compromise the beam emittances. We can see that in Fig. 50(b), σ_z has not yet completed even one slow oscillation, therefore it is difficult to understand its periodicity, there is the underline of the importance of tracking during many synchrotron periods, but such studies are considered to be out of the scope of the present dissertation.

CHAPTER 5

DESIGN, OPTIMISATION, AND CHARACTERISATION

5.1 ELECTROMAGNETIC DESIGN

When designing an rf structure, normally one can start with an "*educated guess*", according to the electromagnetic configuration that suits best the application. In our case, for example, we have parted from the parallel bar cavity [49]. Once the electromagnetic configuration has been set—up to a first order—one could approach the optimisation strategy on several ways, depending on the final goals. In the case of the rf dipole, we decided to increase the cavity's shunt impedance, while lowering the peak surface fields but aiming for a B_P/E_P ratio of 2. Several geometrical and characteristic constrains will be fixed by the machine design, the beam characteristics at the cavity location, and the performance required. Beside the geometrical constraints, during the process of studying a geometry, one develops a sensibility of the effects on the electromagnetic properties of the resonator as a function of the change in its principal geometric parameters.

5.1.1 PRINCIPAL GEOMETRIC PARAMETERS

As previously mentioned, there are many important applications for rf cavities in particle accelerators, besides the acceleration of charged beams, even when the latter remains as the principal one. For velocity-of-light applications TEM accelerating structures have peak surface fields larger than TM010 structures [50]. Even for deflecting cavities the simulations demonstrate that this is not the case and the peak surface fields are comparable for both the TEM and TM010 structures. Also, previous prototypes of the rf dipole have already proven to be very attractive for crabbing and deflecting applications at low frequencies (400 MHz and 499 MHz for the LHC in CERN and CEBAF in Jefferson Lab respectively [28, 6]), due to their considerable small transverse size and dependency of their rf properties on few parameters, which makes the rf dipole geometry not just compact but efficient as well. The present chapter, focuses on the design studies performed to develop a 750 MHz rf dipole, proof-of-principle (PoP) crab cavity for applications in electron-ion colliders.

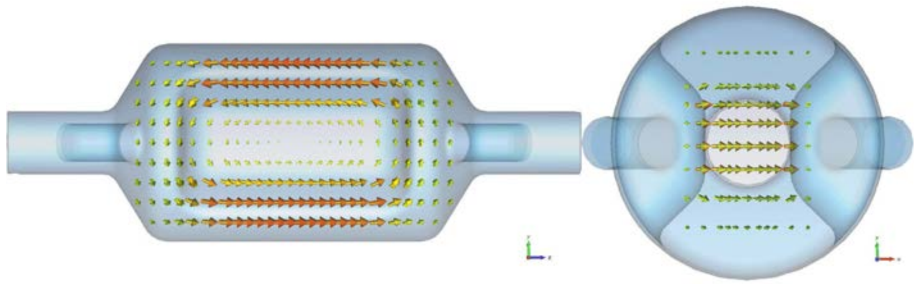

FIG. 51: 3D visualization of the fields: magnetic (left) and electric (right), for the deflecting/crabbing mode.

Figure 51 shows the crabbing mode for the 750 MHz rf dipole cavity final electromagnetic design. De Silva and Delayen presented already a thorough discussion of the basic aspects and the design evolution of parallel bar deflectors in [28]. However, it is important to take a look at the specifics of the design and optimisation processes for the 750 MHz rf dipole to understand which are the key factors from the viewpoint of rf performance, fabrication, and machine operations, all these will help us to understand why the cavity geometry and the fabrication design are the way they are. The cavity radius is the main knob used to keep the rf dipole at the desired frequency, in this section we will not describe in detail the effects on the cavity's properties due to the change of the cavity radius, until Chapter 8, when we lay down the notion of other frequencies and future work for the Jefferson Lab's Electron-Ion Collider crabbing system. In this section, we will focus on the effects of the other key parameters in our design. Graphic descriptions of these geometrical parameters are given in Fig. 52(a), (b), (c), (d), and (e).

We used as a reference length, for all the calculations, the value of a half wavelength of the rf fields, this is for example $\lambda/2 = 200$ mm for 750 MHz. Since the electric field, being the main responsible for the bunch deflection [crabbing], is located in between and along the two parallel bars, it is only natural to optimise the length of these bars for the longest interaction of the beam with the desired part of the rf wave, or in other words, the effective "deflecting length" for our cavity is set to $\lambda/2$. This principle would work for any rf dipole structure, no matter the frequency or the specifics of its geometry. For instance, the bar's length is one of the parameters that define the total cavity length, along with the beam pipes' length (driven by the electromagnetic decay in a circular waveguide), and the slope of the end-caps, also

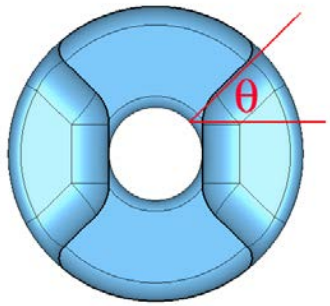

(a) Bar vertical slope (b) Bar width (c) Beam aperture

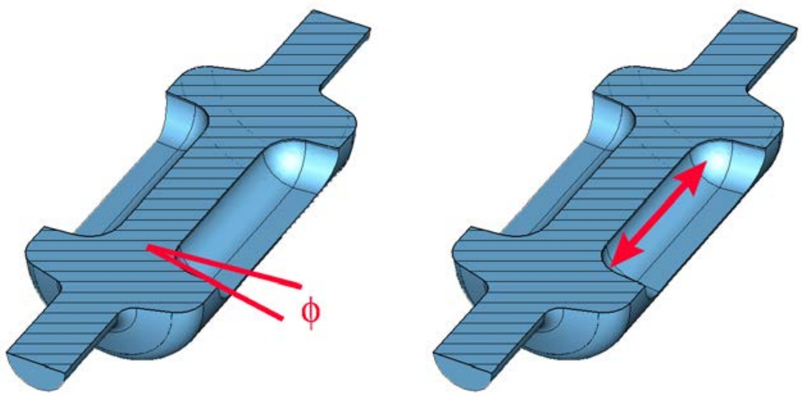

(d) Bar horizontal slope (e) Bar length

FIG. 52: Graphic description of the principal geometric parameters of the 750 MHz rf dipole.

used to optimise multipacting [51], the latter will be discussed later in Section 5.2. Once the bar length was set to $\lambda/2$, we started with the bar vertical angle fixed at 45° and then varied the beam pipe diameter, while letting the width of the bars be 5% wider than the beam pipe diameter in each case (see Fig. 52).

Results of simulations using CST Microwave Studio® are shown in Fig. 53. From this graph, we can observe that as the beam pipe diameter—or more generally—the ratio of the beam pipe to the half wavelength $[d/(\lambda/2)]$ increases, then the R/Q decreases, thus the transverse shunt impedance $[R_t R_S]$ decreases and the peak surface field ratio B_p/E_p increases as well. Therefore, when optimising rf dipole structures like this, the parameter $d/(\lambda/2)$ has to be minimised. At this point, the down selection of the beam pipe diameter was not made based on the optimisation of the rf properties, but on the machine's beam dynamics and more concretely, the expected transverse size of the bunches at the crab cavity location. Therefore the beam pipe aperture diameter was set to be 60 mm.

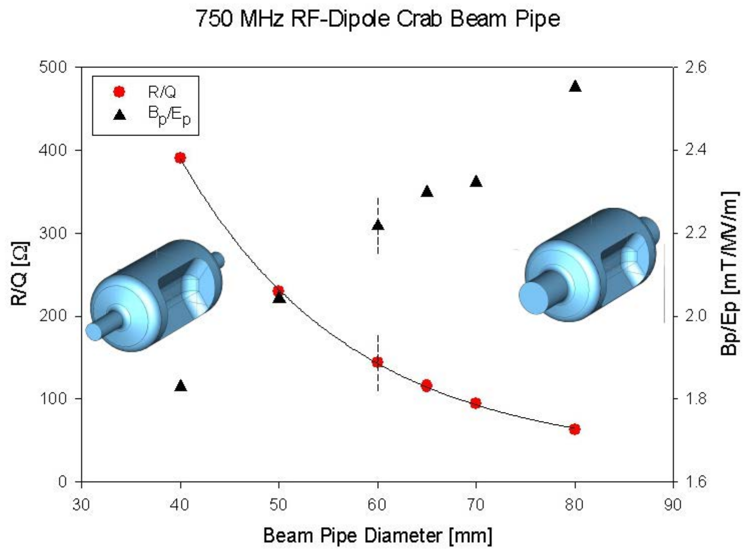

FIG. 53: R/Q and peak surface fields' ratio, as a function of the beam aperture.

Some important properties of a preliminary design of the 750 MHz deflecting structure, obtained from CST Microwave Studio® simulations, are compared to the KEK elliptical crab cavity [52, 53] in Table 4. It can be noted that—for the rf dipole—the deflecting π-mode is the lowest frequency mode, which would simplify the damping of the undesired modes, especially in the case of high current applications.

Keeping all the parameters fixed and for a beam pipe radius of 60 mm, we then optimised the rf properties by varying the bar width (see Fig. 53). The results of the simulations can be seen in Fig. 54. In this case, we can synthesise the optimisation process as maximising R/Q, while we are aiming for a balance peak field surface ratio B_p/E_p as close as possible to 2. However, other practical considerations needed to be taken into account when optimising the electromagnetic design, in terms of requirements on the homogeneity of the fields along the beam pipe, as illustrated in Fig. 55, so that the particles can perceive a more uniform kick inside the cavity for different transverse offset positions in the bunches, this field uniformity is relative to the stability and emittance dilution requirements for both the electron and proton bunches. Based on these considerations and the simulation results presented in Fig. 54, we set the bar width to be at least 5% wider than the beam pipe diameter, choosing the optimal parameter to 63 cm and reaching values of $R/Q \sim 130\ \Omega$ for

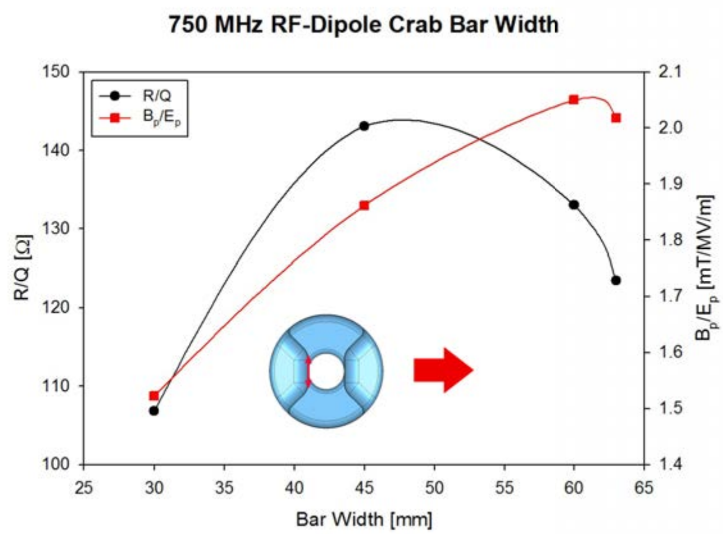

FIG. 54: R/Q and peak surface fields' ratio, as a function of the bar width.

$B_p/E_p \sim 2$ mT/MV/m.

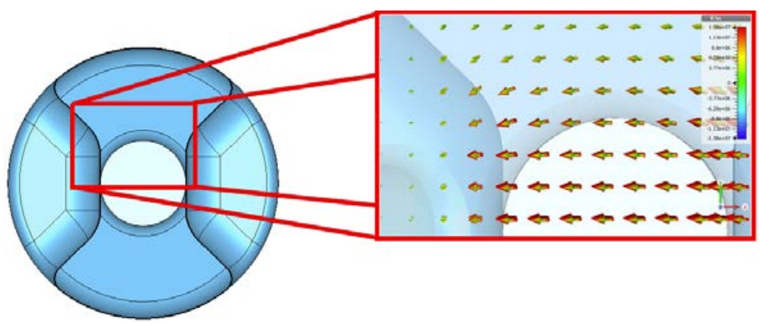

FIG. 55: Visualization's close up of the electric field in the vicinity of the parallel loading elements.

Another important fact to highlight is that, as the bar width is increased, then the peak electric surface field decreases while the magnetic increases, this feature allows the surface peak field ratio to describe the curve presented in Fig. 54 (red line). We can see from Fig. 54, that the width that maximises R/Q is between 45 and 50 mm. While we find our optimal region to be slightly above 60 mm of beam aperture, with a close value of B_p/E_p to 2 mT/MV/m.

As a final optimisation stage, having fixed both the bar width to 63 cm and the bar length to 200 mm, we then varied for different bar horizontal slopes (ϕ) several values of the bar vertical slope (θ), as described in Fig. 54. The resulting peak surface field values—as found from CST Microwave Studio® simulations—and the corresponding line for the $B_p/E_p = 2$ mT/MV/m are shown in Fig. 56 and 57 . In this case, an optimal design is one that keeps the desired balance ratio of the peak surface fields while minimises the value of each one of them.

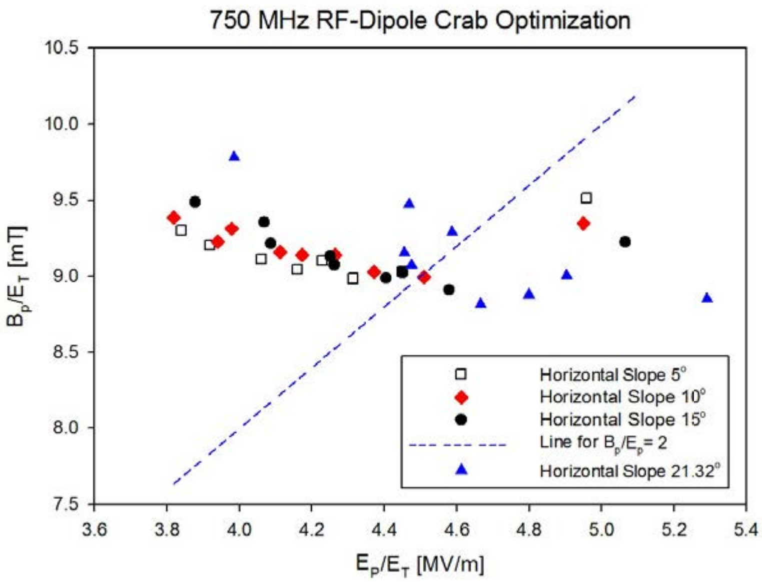

FIG. 56: Normalised peak surface fields for the 750 MHz rf dipole optimisation.

From the graphics in Fig. 56 and 57, we observe how the surface peak fields' ratio increases as the slopes increases but, at about a vertical angle of 70°, the horizontal angle does not make a big difference (see Fig. 57(a)), while for the R/Q, the horizontal slope represents a bigger change; the bigger the horizontal angle is, the smaller the R/Q gets. Therefore, we would like to keep small angles for the bar horizontal slopes.

After the electromagnetic optimisation studies, the geometrical parameters were proposed—and after a couple of iterations with the engineering department in charge of the construction of the cavity at Niowave, Inc.—it was determined as convenient, from the construction point of view, to keep a wide enough external bar length that allowed the blending radius of the bars to meet the blending radius of the cavity's end-caps (circled in red in Fig. 58). Therefore, adjusting the end-caps' slope was needed to keep the bar length at $\lambda/2$ and finally, the model that better accomplished the electromagnetic and production requirements in the most efficient manner was finalised. The principal parameters for the final design are presented in

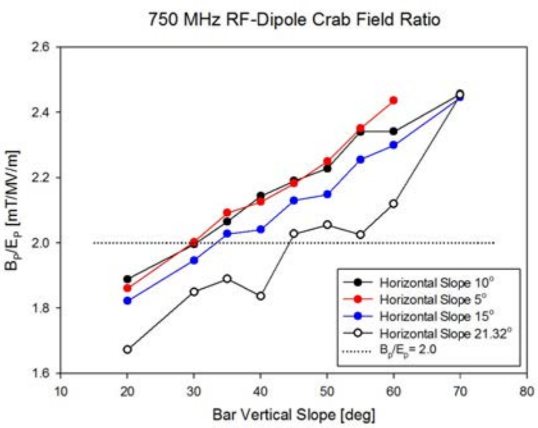

(a) Peak surface fields' ratio

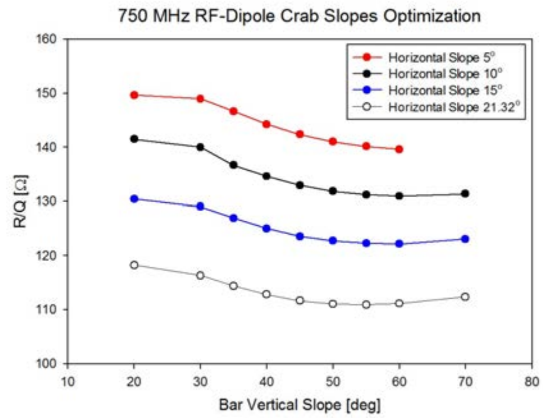

(b) Behavior of the R/Q

FIG. 57: Peak surface fields and R/Q, as functions of the bar slopes for the 750 MHz rf dipole.

Table 4. The four side ports were placed in a region of low surface magnetic field to minimise possible ohmic losses in the non-superconducting flanges and could be used for chemistry, cleaning, as input, output and possible HOM damping couplers location for a next iteration of the design. The angle described by these ports (31.58°) is necessary to make them perpendicular to the face of the end cap, where they are placed on. The distance between the load elements is fixed to be 60 mm, following the same criteria employed to the beam pipe diameter in terms of the σ for the bunches at the location of the crab cavities.

The TEM-like configuration for the crabbing mode of the final 750 MHz rf dipole design is illustrated in Fig. 59, where the transverse electric field can be seen between the oscillating load elements on the top left figure (a). Also, at 90° out of phase with the electric field, the transverse magnetic field can be seen looping around the same load elements on the top right figure (b). The momentum transfer for the crabbing of the bunches, is given almost fully by the transverse electric field of the operating mode. The surface electric field is concentrated in the bars as shown in the bottom left figure (c), while the surface magnetic field is distributed all around the outer conductor of the cavity but located with more intensity in the top and bottom walls of it as observed in the bottom right figure (d). The side ports on the cavity have been placed in the faces of the end-caps where the surface magnetic field is lower—as

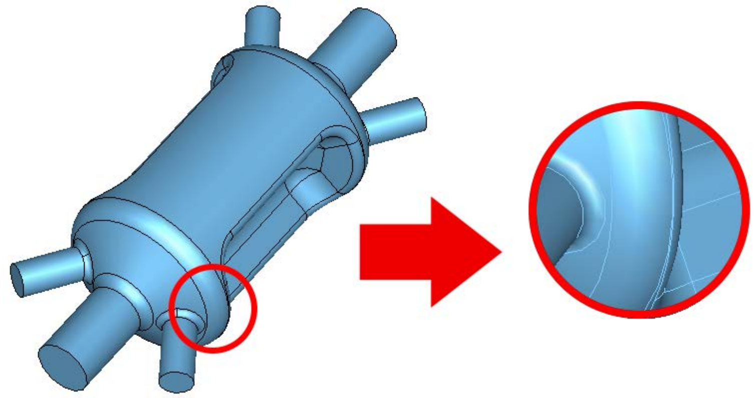

FIG. 58: End cap's blending radio meets curvature of loading element's external blending radius.

mentioned before—nevertheless it is not zero at these points and as a consequence of this, we have ohmic losses on the ports' flanges, the analysis of these losses will be presented later in Section 6.5.

To understand the operation of the rf dipole as a crab cavity, we need to understand Fig. 59(a) and (b). While for understanding the rf properties optimisation process, we need to study how both Fig. 59(c) and (d), change as variations in the geometrical parameters are performed.

As final design step, a tuning stack parameter per side ($\mathrm{d}f/\mathrm{d}z$ in MHz/mm) was determined to estimate the change of the frequency due to the change of the length of the cavity's outer conductor. In this way, symmetrical trimming at the ends of the outer conductor could be employed to tune up the cavity frequency during its construction before the final electron beam welding.

5.2 MULTIPACTING ANALYSIS

Multipacting is one of the principal limitations of performance in rf structures. It occurs when electrons, produced by field emission—or any other means—are accelerated and smashed against the resonator's walls, secondary electrons then can be emitted and accelerated once again towards the walls, creating new electrons. This process can lead to localised and resonant trajectories, reaching impact energies correspondent to a secondary emission yield (SEY) greater than unit, resulting in a cascading effect that can cause problems, such as low achievable gradients in the structure, bunch instabilities, and quenches by thermal breakdown in the case

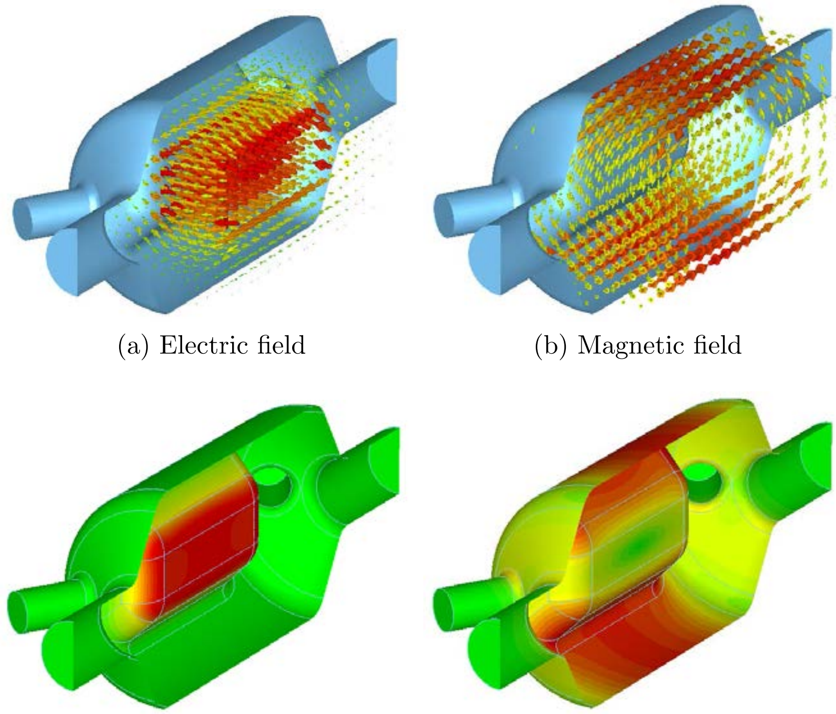

(a) Electric field (b) Magnetic field

(c) Surface electric field (d) Surface magnetic field

FIG. 59: Fields configuration in the rf dipole for the deflecting/crabbing mode.

of superconducting structures [54]. Due to its complexity and random nature, this non-relativistic phenomenon has been for a long time an important case of study that needs to be assessed in order to further improve the operation and performance of current and future particle accelerators.

The SEY, as a function of the impact energy ($\delta\left(E\right)$), changes for different materials and is surface condition dependent [55], therefore the impact energy *bandwidth* ($E_{II} - E_I$)—to have a multipacting condition (i. e. $\delta > 1$)—varies from case to case. Figure 60 shows the general SEY function curve for an arbitrary surface. In the case of pure and clean Nb, the range of impact energies for the multipacting condition is $E_I > 150$ eV, and $E_{II} < 2000$ eV. The multipacting barriers are known to be either soft and easily processed and cleaned, or hard multipacting barriers that cannot be removed by processing and may need redesigning of the cavity geometry in order to properly operate.

TABLE 4: Properties of two crab cavity designs

Parameter	**750 MHz RFD**	**KEK Cavity**	**Units**
Freq. of π mode	750.1	501.7	MHz
$\lambda/2$ of π mode	200.0	299.8	mm
Freq. of 0 mode	1350.6	$\sim$700.0	MHz
Freq. of nearest mode	1055.9	413.3	MHz
Freq. of lower order mode	-	413.3	MHz
Cavity length	300.0	299.8	mm
Cavity width	187.4	866.0	mm
Cavity height	187.4	483.0	mm
Bars width	63.0	-	mm
Bars length	200.0	-	mm
Bar Vertical Slope	45	-	deg
Aperture diameter	60.0	130.0	mm
Deflecting Voltage (V_T^*)	0.2	0.3	MV
Peak electric field (E_P^*)	4.45	4.36	MV/m
Peak magnetic field (B_P^*)	9.31	12.45	mT
B_P^*/E_P^*	2.09	2.85	$\frac{\text{mT}}{\text{MV/m}}$
Geometrical factor	131.4	227	Ω
$[R/Q]_T$	124.15	48.90	Ω
$R_T R_S$	1.65	1.11	$\times 10^4 \Omega^2$

At E_T^*= 1 MV/m

5.2.1 REDUCING MULTIPACTING BY DESIGN

We used the extrusion length of the end-caps (see Fig. 61) as a varying parameter to study the optimisation of the multipacting conditions for the 750 MHz rf dipole, keeping all the other geometrical parameters fixed with exception of the cavity radius, this was used as a free knob to correct the resonant frequency of the fundamental mode. The extrusion of the end-caps results in the change of the total cavity length, this is not relevant from the design point of view, as long as we keep the parallel bars' length constant to the effective length of $\lambda/2 = 200$ mm.

Once a set of models with different extrusion lengths from $l_{min} = 20$ mm to $l_{max} = 50$ mm were generated, we used the Omega3P and the Track3P modules from the "Advanced Computational Electromagnetic Simulation" (ACE3P) Suite [56] developed by SLAC, running in the NERSC [57] super cluster at Berkeley, to obtain

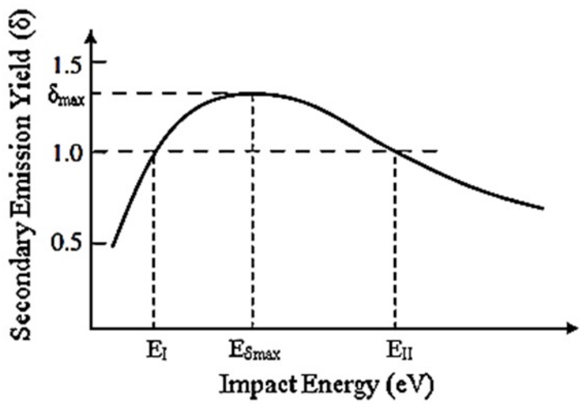

FIG. 60: Secondary emission yield as a function of the particles' impact energy.

the eigenmodes and the multipacting conditions respectively.

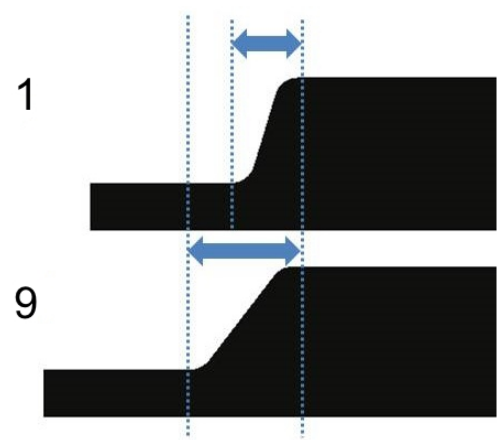

FIG. 61: Variation of the extrusion length of the end-caps, starting at 20 mm (model 1) and finishing at 50 mm (model 9).

The resulting 3D locations and impact energies (in color code) of the multipacting conditions for 9 of the studied models are presented in Fig. 62, where the value of the extrusion length is increasing (from right to left and top to bottom, respectively). The particles' resonant locations are considerably cleared out from the top of the external conductor to populate slightly more the end-caps, where both the electric and magnetic fields are lower. This places them closer to the auxiliary ports, thus making it easier for the vacuum systems to help with the evacuation and therefore reducing the sustainability of the resonant conditions.

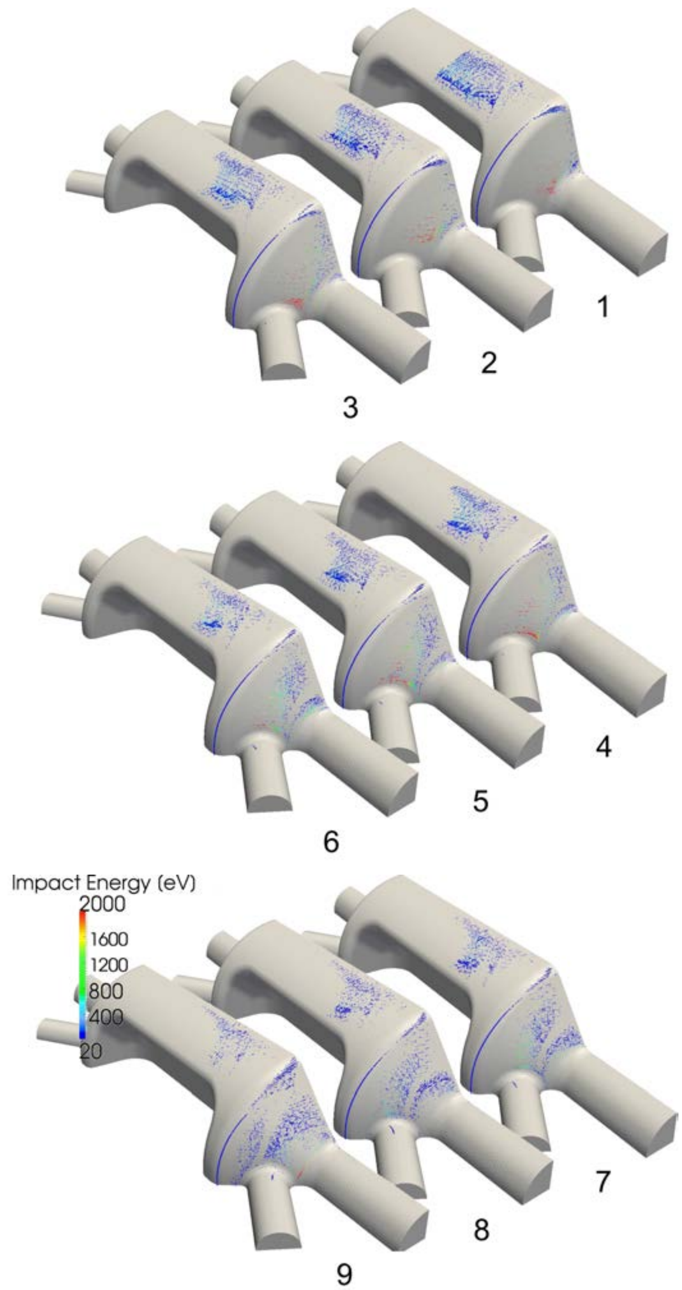

FIG. 62: Comparison of the multipacting impact energy and resonant locations for increasing values of the extrusion length of the end-caps, from 20 mm (in 1) to 50 mm (in 9).

We used the two extremal values of our optimisation parameter (i. e. l_{min} = 20 mm, and l_{max} = 50 mm) to compare the multipacting levels obtained by the simulations as seen in Fig. 63. It can be observed that the multipacting barriers do not appear to have great differences between each other, despite the fact that for the model with smaller end-cap's extrusion (i. e. l_{min} = 20 mm, in the top-right most model (1) of Fig. 63) higher impact energies are reached, which is not necessarily an important feature since particles with impact energies > 2000 eV do not contribute to multipacting in Nb. However, both multipacting barriers are well defined at the lower voltage levels, keeping the operating region virtually multipacting free. What is hard to appreciate from the graphs, is that the barriers for the model with smaller extrusion length are heavily denser than those for the model with longer extrusion length.

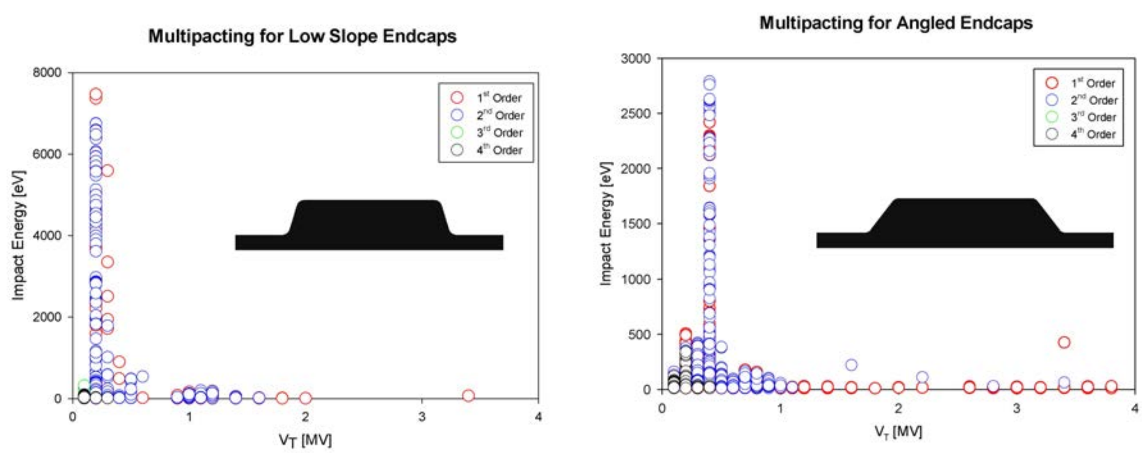

FIG. 63: Multipacting levels as a function of the transverse voltage for the 2 extremal values of extrusion length of the end-caps: 20 mm (left, model 1) and 50 mm (right, model 9).

Using this qualitative analysis, we can say that the 750 MHz rf dipole design does not show critical multipacting levels at the operation voltages (up to 3 MV per cavity) and most of the barriers are presented at lower voltages as seen in Fig. 64. It is obvious that the most problematic area for multipacting are the end-caps for this design, but the in general, the rf dipole shows to be relatively multipacting-clean design overall. Later, in Section 6.4.5, we will discuss how these results are in agreement with the multipacting activity observed during the prototype cryo test.

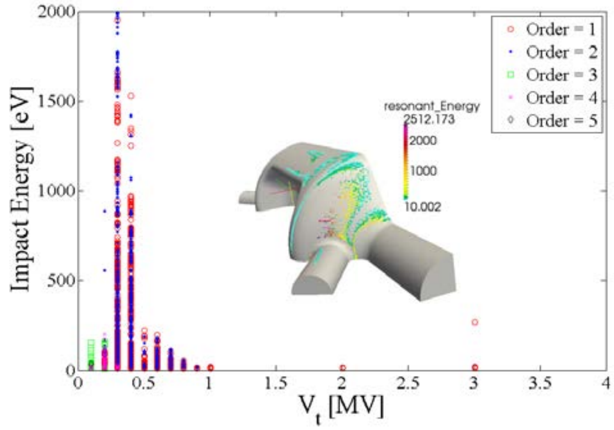

FIG. 64: Electron's impact energy vs V_t and their impact location, for the first 5 orders of multipacting in the 750 MHz rf dipole PoP cavity.

5.3 HIGHER ORDER MODE ANALYSIS

For high-current applications—for instance, up to 3 A stored for the electron beam in the MEIC—the properties of the higher-order modes and their damping become more relevant for cooling and stability during operations. The rf dipole geometry has the crabbing/deflecting mode as the lowest frequency mode, the closest higher order mode is a dipole mode with a frequency of ≈ 1.5 times the fundamental frequency (f_0). The first degenerated vertical mode has a frequency ≈ 2.1 times the fundamental frequency. We use the field components on axis to characterise the type of higher order modes, as can be appreciated in Table 5.

TABLE 5: Types of HOMs

Field on Beam Axis	**Type of Mode**
E_x, H_y	Deflecting in x
E_z	Accelerating
E_y, H_x	Deflecting in y
H_z	Doesn't couple to the beam

We have analysed the properties of the higher order modes, up to the beam pipe cutoff frequency for the 750 MHz rf dipole. In Table 6, we have listed the properties of the representative modes with relatively higher R/Q values. The HOM spectrum for the 750 MHz rf dipole is shown in Fig. 65, with the frequencies normalised with respect to the fundamental frequency of the cavity ($f_0 = 750$ MHz). An important factor to highlight for this design, is the absence of any lower order modes and similar order modes, along with a wide frequency separation between the HOMs and the fundamental mode, making the damping of the HOMs easier. Finally, the field distribution for three of the resonant modes are shown in Fig. 66.

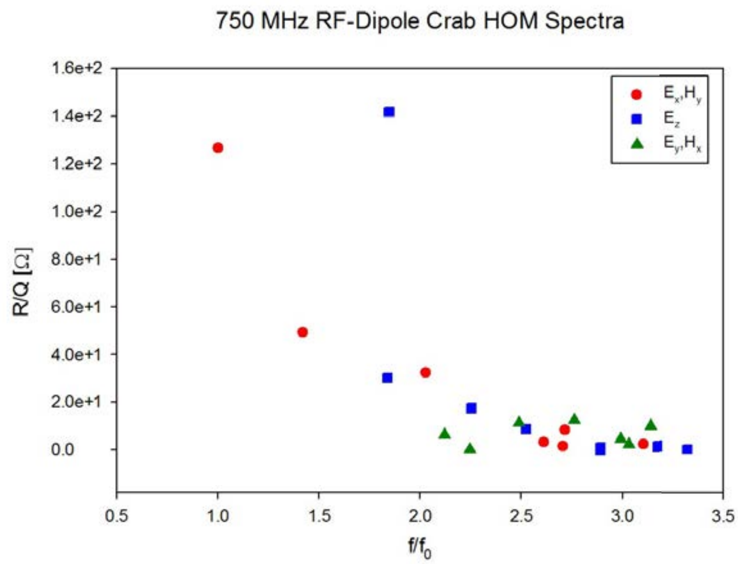

FIG. 65: HOMs spectrum for the $f_0 = 750$ MHz rf dipole.

TABLE 6: Modes with highest R/Q

Mode Type	Frequency [MHz]	R/Q [Ω]
E_x, H_y	750.10	124.294
E_z	1384.03	141.959
E_y, H_x	1589.31	6.51428

The transverse R/Q—or $[R/Q]_T$—values, calculated both using the direct integration method (Eq. 164) and the Panofsky Wenzel method (Eq. 165) [58], are in agreement within $< 2\%$. The longitudinal R/Q values for the deflecting modes were found to be negligible (see Eq. 166). For the fundamental mode and by using Eq. 104 and 167, the net deflection due to the magnetic field is $V^*_{T,H} = -0.211$ MV and due to the electric field is $V^*_{T,E} = 0.412$ MV (where the mark * means that the voltage has been normalised to a transverse field $E_T = 1.0$ MV/m), then from Eq. 115 and 103

$$\left[\frac{R}{Q}\right]_T = \frac{|V_T|^2}{\omega U} = \frac{|\int_{-\infty}^{\infty}\left[\vec{E}_x\left(z, x=0\right) + i\left(\vec{v}\times\vec{B}_y\left(z, x=0\right)\right)\right] e^{\frac{i\omega z}{c}} \mathrm{d}z|^2}{\omega U}, \tag{164}$$

$$\left[\frac{R}{Q}\right]_{T,PW} = \frac{|V_z\,(z, x = x_0)\,|^2}{(\omega U)\,(k x_0)^2} = \frac{|\int_{-\infty}^{\infty} \vec{E}_z\,(z, x = x_0)\,\mathrm{e}^{\frac{i\omega z}{c}}\mathrm{d}z|^2}{(\omega U)\,(k x_0)^2}\,, \tag{165}$$

this implies that $E_z\,(x = 0) = 0$.

$$\frac{R}{Q} = \frac{|V_z|^2}{\omega U} = \frac{|\int_{-\infty}^{\infty} \vec{E}_z\,(z, x = 0)\,\mathrm{e}^{\frac{i\omega z}{c}}\mathrm{d}z|^2}{\omega U}\,, \tag{166}$$

$$V_T = \int_{-\infty}^{\infty} \left[E_x(z)\cos\frac{\omega z}{c} + cB_y(z)\sin\frac{\omega z}{c}\right]\mathrm{d}z\,. \tag{167}$$

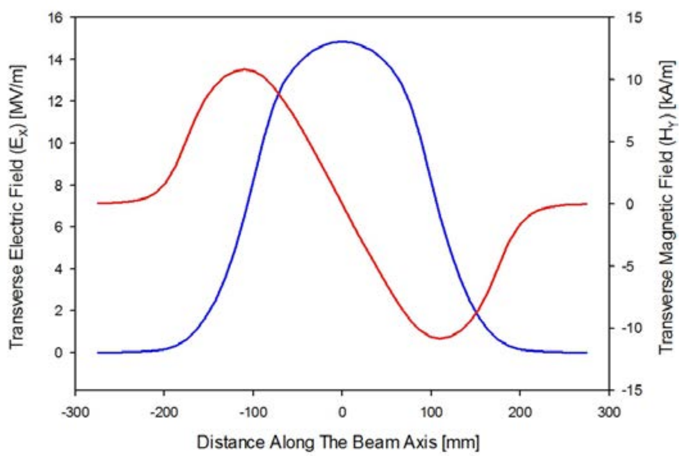

(a) Transverse fields for the fundamental mode

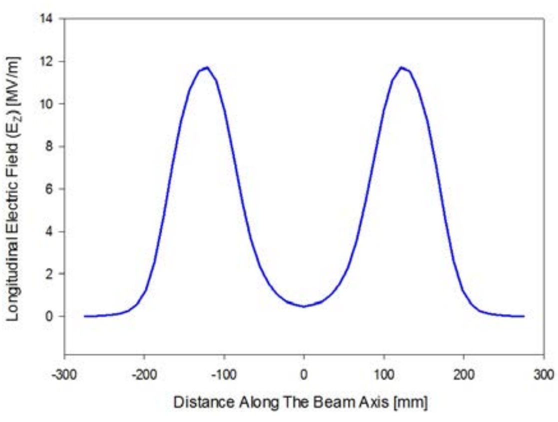

(b) Accelerating field of the highest R/Q HOM

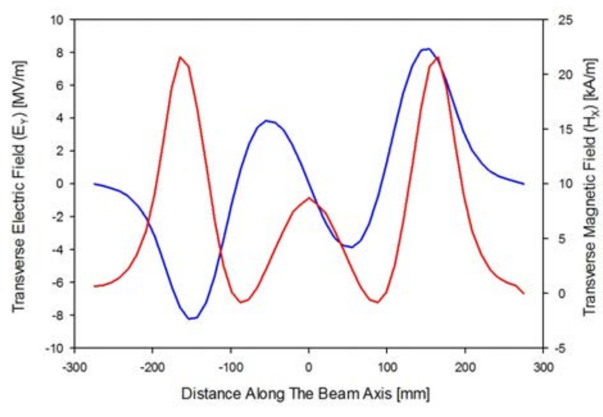

(c) Fields of the first vertical deflecting mode

FIG. 66: Field distributions along the beam axis for a representative set of modes of the 750 MHz rf dipole.

5.4 MULTIPOLE FIELD ANALYSIS

Recently, several studies regarding the rf dipole design have been presented, including analysis on the multipole components for some applications [59, 60]. However, this section is intended to provide a point of comparison on *to what extent* the parameters in the rf dipole geometry can be manipulated to tailor specific multipole components on the electromagnetic field in order to achieve the parameters required in different applications. In the case of the 750 MHz rf dipole crab cavity corrector for Jefferson Lab's Electron-Ion Collider [61], the multipole components and uniformity of the fields are crucial factors in the beam emittance conservation in linear and circular colliders—as previously discussed in Section 4.5.4. Thus, proper tailoring of the higher multipole components is key to achieve beam stability conditions for high luminosity machines, this being the main motivation for the present analysis.

In this section, we surveyed the field uniformities and multipole contents for a set of 750 MHz rf dipole models, presenting both a qualitative and quantitative analysis of the inherent flexibility of the structure, to facilitate the study of its potential limitations for specific applications.

5.4.1 PARAMETERISATION

The rf dipole does not have a longitudinal electric field on axis, and the deflecting/crabbing kick is mainly given by the transverse electric field, which is concentrated in the parallel loading elements region. Therefore, the field uniformity and its multipole components can be modified by introducing an inwards curvature around the flat section of the parallel bars, effectively wrapping them around the beam pipe axis to reduce transversal variations of the fields. For the present analysis, we parametrised this curved deformation of the parallel bars using an ellipse as is depicted in Fig. 67.

Keeping the parameter r_x constant and equal to the beam aperture, we varied the gap between the bars (dL), as well as the minor radius of the elliptical deformation (r_y). For comparative purposes we analysed twelve models of the 750 MHz rf dipole design and their correspondent parameters are enlisted in Table. 7.

5.4.2 MULTIPOLE TAILORING SURVEY

Using a Fourier series expansion of the longitudinal field $E_z(r, \phi, z)$ (see Eq. 120),

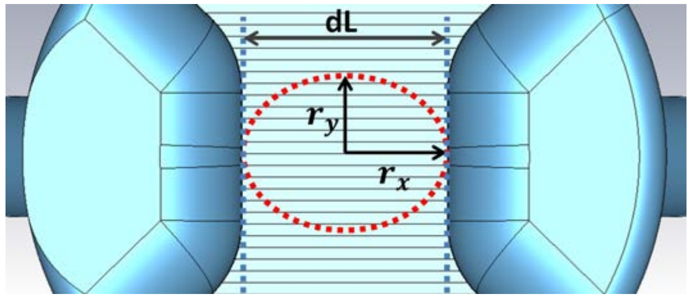

FIG. 67: Close up of the parallel loading elements and the varying parameters used to tailor the multipole components for the 750 MHz rf dipole.

TABLE 7: Parameters corresponding to the different 750 MHz rf dipole models

Model #	R_x **[mm]**	R_y **[mm]**	**dL [mm]**
1	30.0	30.0	59.8
2	30.0	29.0	59.8
3	30.0	28.0	59.8
4	30.0	27.0	59.8
5	30.0	26.0	59.8
6	30.0	25.0	59.8
7	30.0	20.0	59.8
8	30.0	30.0	58.0
9	30.0	20.0	58.0
10	30.0	30.0	57.0
11	30.0	20.0	57.0
12	30.0	30.0	56.0
13	30.0	20.0	56.0

we calculated the multipole components as:

$$E_z^{(n)}(z) = \frac{1}{r^n} \int_0^{2\pi} E_z(r, \phi, z) \cos(n\phi) \, \mathrm{d}\phi \tag{168}$$

Following the standard definition of the multipole components used for magnets and using that for time dependent rf fields $E_{acc}^{(n)}(z) = E_z^{(n)}(z) e^{j\omega t}$, then:

$$B^{(n)}(z) = j\frac{n}{\omega} E_z^{(n)}(z) e^{j\omega t} \tag{169}$$

$$b_n = \int_{-\infty}^{\infty} B^{(n)}(z) \, \mathrm{d}z \tag{170}$$

Some important remarks to make are that we neglected the skew components

(a_n) of the fields and found all the even components of the expansion (i. e. b_n, with $n = 0, 2, 4, ...$) to be negligible due to the two-fold symmetry of the rf dipole—this is true as long as the fabrication errors are also negligible. A detailed description of the analytical and numerical methods used to calculate the multipole field expansions is described by S. U. De Silva in [59]. To illustrate the field multipole component tailoring capabilities of the rf dipole, we present in Fig. 68 the survey of the main multipole strengths for the set of 750 MHz crab cavity models studied in this section.

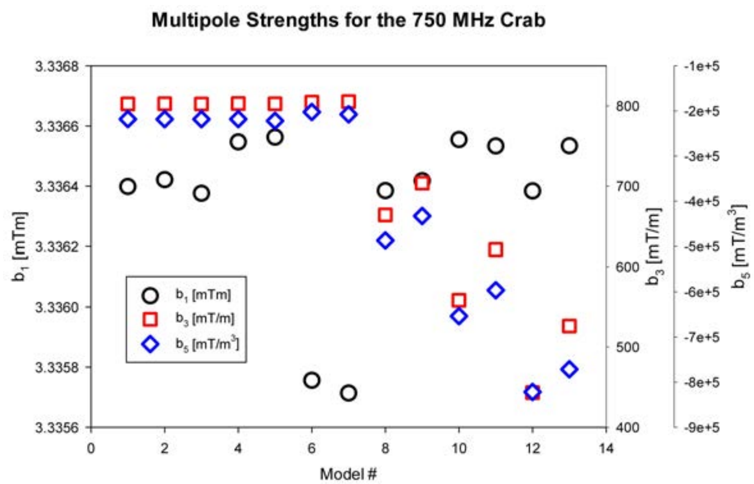

FIG. 68: Survey of the first non zero multipole components: dipole (black), sextupole (red) and decapole (blue) strengths for the design models at $V_T = 1$ MV.

Even when it is hard to appreciate a clear tendency of the dipolar strength for the different models in Fig. 68, due to the scale difference on the axis, it is important to notice that the variation range for b_1 is less than 0.1%, while for b_3 is $\sim$ 45%, and for b_5 it is about 75%, showing that it is possible to tweak higher multipole components without causing major altering in the dipolar content.

5.4.3 COMPARISON OF TWO CASES

Next, two cases from the set of models studied in this section are presented, which correspond to two extremal values of b_3 and b_5, such as model 1 and 12 (see Fig. 68 and Table 7). Figure 69 shows the difference in the curved deformation on the parallel loading elements for each one of these models.

The comparison of the first two multipole components of the field for both models are depicted in Fig. 70, where it is possible to see the reduction of the sextupolar

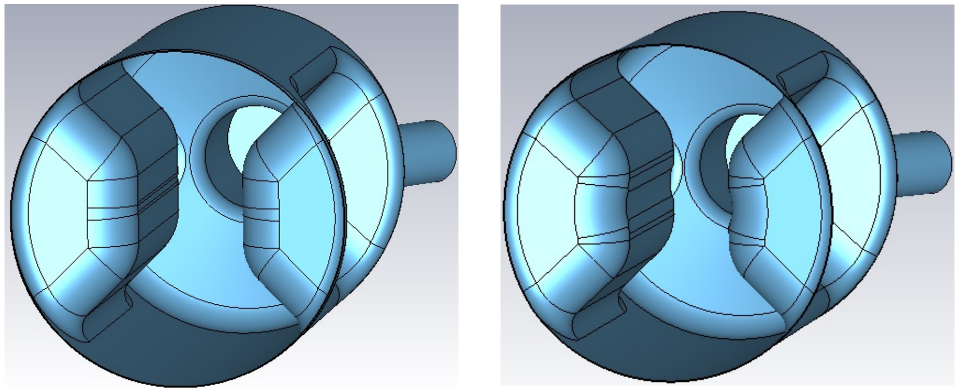

FIG. 69: Cut-plane views of two different shaped loading elements, corresponding to Model 1 (left) and Model 12 (right).

component while the dipolar component remains the same, up to a $\sim 99.9\%$.

After analysing the feasibility of employing elliptically parametrised curved deformations on the parallel loading elements as a tailoring method for the multipole components and transverse uniformity of the fields on the 750 MHz rf dipole, the results showed the versatility of the rf dipole for applications with strong emittance and bunch instabilities control requirements. We present, as point of comparison, the results of the two extremal cases from the set of models examined in here. The main multipole strength components are listed in Table 8.

TABLE 8: Multipole components for two models of the 750 MHz rf dipole

	Model 1	**Model 12**	**Units**
V_T	1.0	1.0	MV
b_1	3.336	3.336	mTm
b_2	0.0	0.0	mT
b_3	8.025	4.933	$\times 10^2$ mT/m
b_4	0.0	0.0	mT/m^2
b_5	-2.1780	-8.218	$\times 10^5$ mT/m^3

5.5 STRUCTURE ANALYSIS

In general, superconducting cavities see themselves under different stresses during their different operating conditions. For instance, a niobium cavity under vacuum will see a diverse set of external pressures, for example: during a leak check at room temperature (1 atm), in the vertical test dewar at 4 K (1.1 atm) or 2 K (0.003 atm).

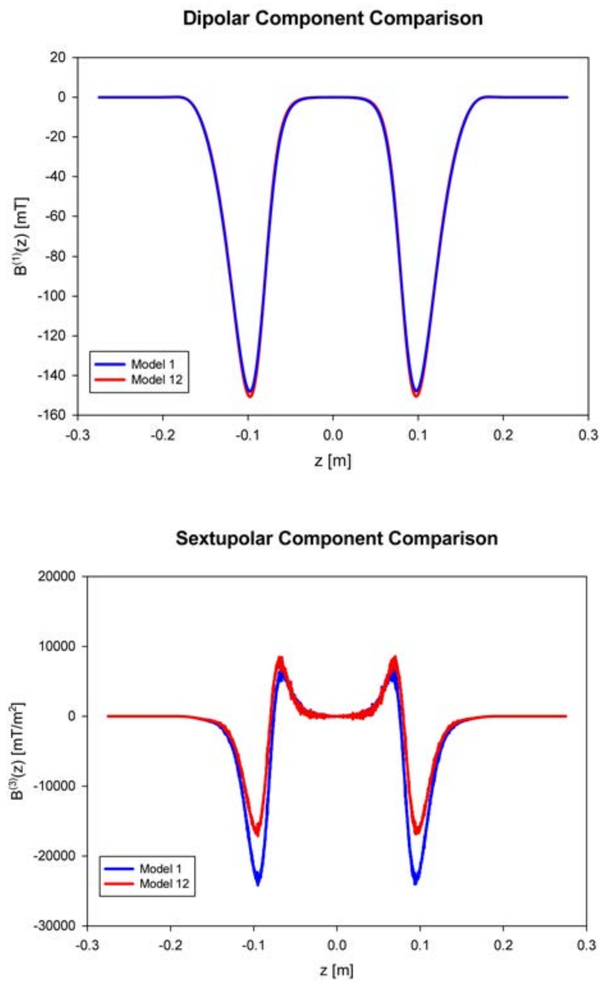

FIG. 70: Comparison of the multipole components: dipolar (top) and sextupolar (bottom), along the z- axis with a radial offset $r_{\text{off}} = 1$ cm for Models 1 (blue) and 12 (red).

For cryomodule testing, the conditions could vary between 1.5 and 1.8 atm, while the safety limit specifications could reach the 2.6 atm of external pressure at 300 K. These numbers are taken from specifications given for the HL-LHC crab cavities for the SPS test [62], specifications for the 750 MHz rf dipole have not been set yet. However, it is important to know the behavior of the cavity with respect to the external pressure. In this section, we present mechanical simulations made in ANSYS [63], both for the external pressure sensitivity ($\partial f/\partial P$) and the change in frequency due to internal radiation pressure—or Lorentz force detuning—(k_L). The Lorentz force detuning (LFD) and the pressure sensitivity will be discussed later on in Sections 6.4.4 and 6.4.2 respectively, where the calculations presented in this section will be compared to the results obtained during cryogenic testing of the rf dipole proof-of-principle cavity.

The material properties of the niobium used in the simulations, both for the pressure sensitivity and the Lorentz force detuning, are enlisted in Table. 9.

TABLE 9: Niobium properties at room and cryogenic temperatures

Parameter	**Value**	**Units**
Density	750.10	kg/m^3
Poisson's ratio	1384.03	
Young's modulus (300 K)	1589.31	Pa
Young's modulus (4 K)	1589.31	Pa

5.5.1 PRESSURE SENSITIVITY

The rf dipole structure is affected by external pressure, due to its relatively large flat surfaces on the parallel bar region, since the proof-of-principle cavity has been constructed without the intention of reaching operating conditions, the effects of external and radiation pressure are prominent in it, due to the lack of stiffening or structural reinforcement, along with a wall thickness of 3 mm (before forming or chemistry). Figure 71 shows a 3D model of the 750 MHz rf dipole, after reducing its size using its 3 mirror planes of symmetry to economise the computing time; in the images we can see that, when under an external pressure, the flat sections of the loading elements suffer an inwards deformation, increasing the cavity's capacitance and therefore lowering its frequency—following the fact that $\omega_0 = 1/\sqrt{LC}$, where ω_0 as the resonant frequency, L the inductance, and C the capacitance. The change of the resonant frequency, as a function of the external pressure, is what we call **pressure sensitivity** and after simulations—always considering we are working under a linear regime—it was found to be $\partial f/\partial P = -0.52$ kHz/torr. Crab cavity applications are typically stringent on the pressure sensitivity and Lorentz force detuning of the crabbing structures. Since the goal of this thesis is to present and study a general scheme of the crabbing systems for an electron-ion collider—for which the proof-of-principle cavity will suffice—these detailed structural studies will be proposed as future steps towards a finalised model ready for operations. However, it is worth mentioning that other rf dipole structures (499 MHz and 400 MHz) have been proven to reduce the pressure sensitivity for at least 1 order of magnitude using 4 mm thickness of the walls and stiffening bars [62], giving us confidence that this could be also extended to the 750 MHz.

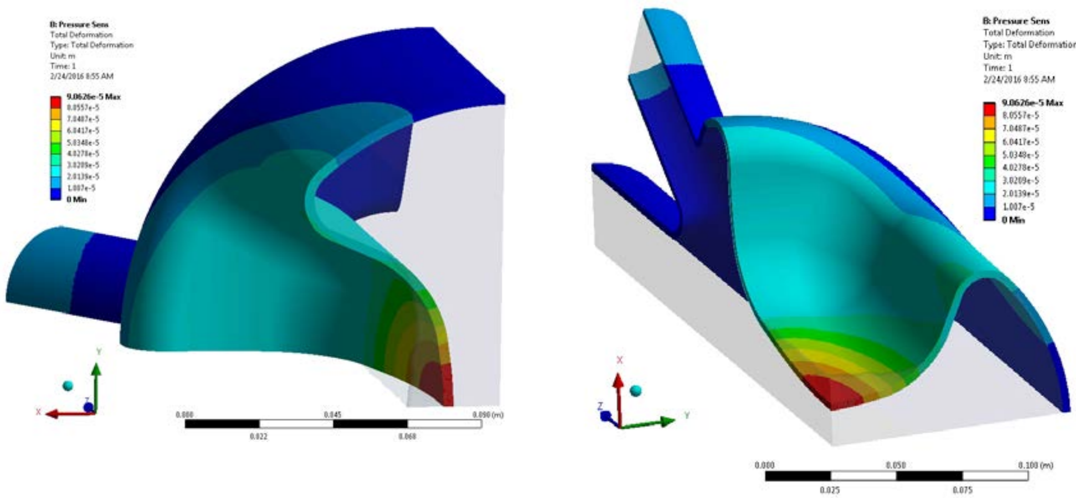

FIG. 71: Symmetry section of the 750 MHz rf dipole showing the deformations caused by external pressure.

5.5.2 LORENTZ FORCE DETUNING

The alternating fields inside the cavity, produce changes on the surface charge and current distributions on the cavity walls, thus inducing radiation pressure onto the structure, this pressure is excerted in different directions for the regions with high electric or high magnetic field. Changes on the high magnetic field region will change the effective inductance (L) of the cavity, while changes in the high electric field region will change the effective capacitance (C) and therefore resulting in detuning for both cases. The expression for the radiation pressure (P) due to the electric (E) and the magnetic (H) field magnitudes, can be seen in Eq. 171. While the detuning (Δf) due to this pressure, in terms of the transverse gradient (E_t), is written in Eq. 172.

$$P = \frac{1}{4}\left(\epsilon_0 E^2 - \mu_0 H^2\right) , \tag{171}$$

$$\Delta f = -k_L \cdot E_T^2 , \tag{172}$$

where k_L is called the *Lorentz coefficient*.

Figure 72 shows the deformations on the 750 MHz rf dipole, due to the Lorentz force. It is interesting to notice that the flat walls on the loading elements experience an inwards deformation, very similar to the one due to the external pressure.

However, it can also be observed that there is an extra deformation outwards on the curved walls, due to the high magnetic field contribution. These images depicting the deformations on the 750 MHz rf dipole due to the Lorentz force, were generated using ANSYS and the calculated Lorentz coefficient using this method was found to be $k_L = -258.8\,\frac{\mathrm{Hz}}{(\mathrm{MV/m})^2}$.

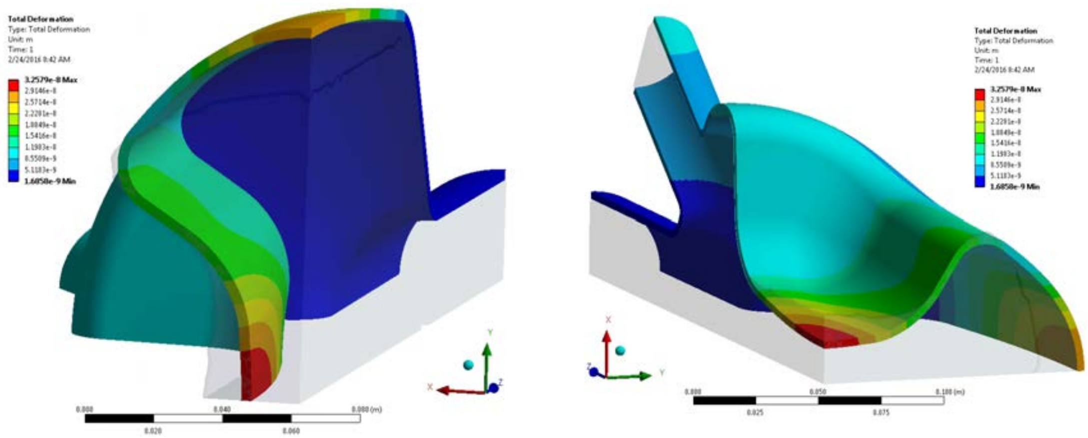

FIG. 72: Symmetry section of the 750 MHz rf dipole showing the deformations caused by radiation pressure.

CHAPTER 6

FABRICATION, PROCESSING, AND TESTING

Transverse deflectors have been studied for several applications in the past but when it comes to designing for high performance applications which require compact superconducting structures, some interesting approaches have been taken into consideration. TEM parallel rod cavities showed promising performance for high $\left[\frac{R}{Q}\right]_T$ [26] and after a long evolution and optimisation of parameters such as balanced peak surface fields and low multipacting, a TE-like resonant structure known as the rf dipole was developed by S. U. De Silva *et al* at Old Dominion University [6, 28, 64, 65].

The optimisation of an rf dipole structure will depend greatly on its applications and machine-specific constraints, from the impedance budget and field flatness to its physical dimensions. In this chapter, we present the fabrication, tests preparation, and results of a proof-of-principle (PoP) superconducting rf dipole, designed as a prototype for a 750 MHz crabbing corrector for the Jefferson Lab's Medium Energy Electron-Ion Collider. The 750 MHz rf dipole has been successfully tested at 4.20 K and 1.99 K at the Jefferson Lab's Vertical Testing Area (VTA). The analysis of its rf performance during cryogenic testing, along with Helium pressure sensitivity, Lorentz detuning, surface resistance, and multipacting processing analysis are presented in this work. Detailed calculations of losses at the port flanges are included for completeness of the cavity's cryogenic performance studies. Its principal parameters and rf properties have been discussed in Chapter 5, Table 4. For instance, Fig. 73 represents a visualization of the longitudinal (a) and transverse (b) cross sections of the structure.

It is important to remark that the design and fabrication of the 750 MHz MEIC crab cavity prototype was performed under the Small Business Technology Transfer (STTR) program of the United States Department of Energy (US-DOE) [66], as a project funded for both phases I & II, in a collaboration between Old Dominion University and Niowave, Inc.

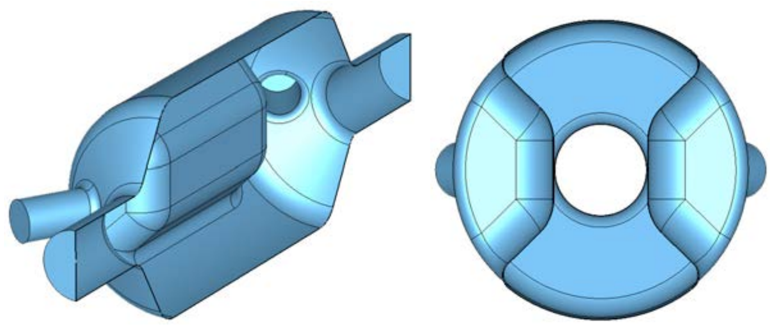

(a) Longitudinal (b) Transverse

FIG. 73: Cross sections of the optimised PoP 750 MHz rf dipole.

6.1 FABRICATION

During Phase I of the STTR, the preliminary electromagnetic design of the cavity [described previously in Chapter 5] was used as the basis for the mechanical design of the cavity prototype. The mechanical design was finalised during Phase II of the STTR project and its final version [shown in Fig. 74] was accepted for production.

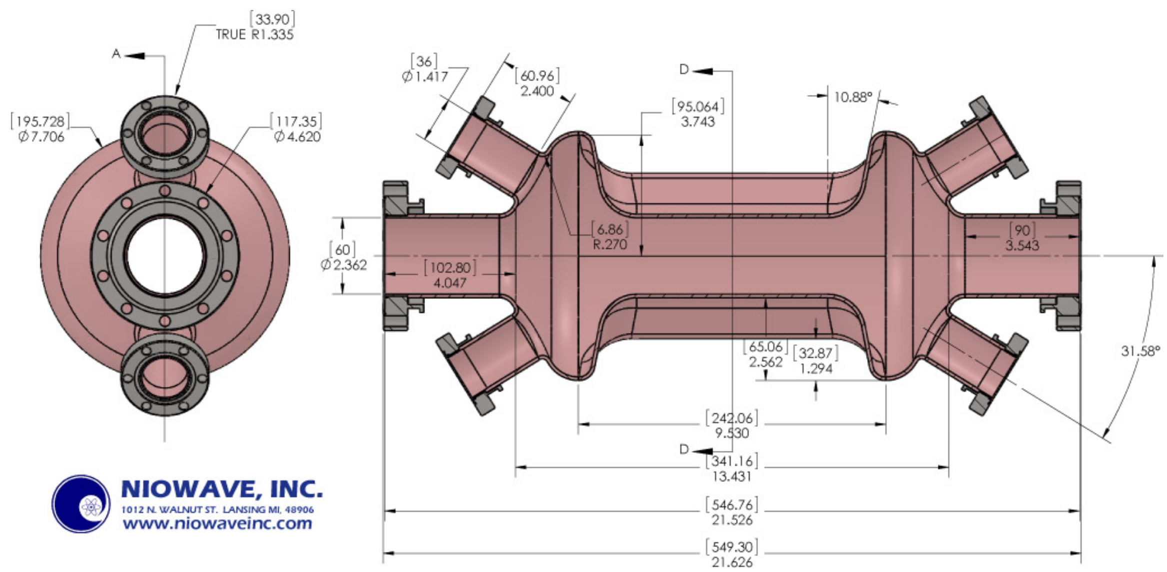

FIG. 74: Mechanical Design of the 750 MHz crab PoP cavity (Image: Niowave, Inc).

Several sets of subassemblies were manufactured from 3 mm thick, large grain, non alloyed, high purity, annealed Niobium sheets (residual resistivity ratio $RRR =$ 355-405) [67], and deep drawn. Electron beam (EB) welding was used for joining parts and subassemblies together, Fig. 75 (a), (b), (c), and (d) show the subassemblies prior to the final EB welding.

(a) End-cap ports EB welding (b) Cavity sections previous to final EB welding

(c) End-cap detail (d) Center body cross section view

FIG. 75: EB welding of the 750 MHz crab MEIC cavity end-cap's ports (a), welded subassemblies before the final welding (b), end-cap subassembly (c), and center piece (d). Images: Niowave, Inc.

As the final design step, a tuning stack parameter of df/dz=-0.9354 MHz/mm per side was calculated to estimate the relation between the length of the outer conductor and the change in the resonant frequency of the cavity. Following this, symmetrical trimming at the ends of the outer conductor were employed to tune up the cavity frequency during its construction prior to electron beam welding, a df/dz=-0.9259 MHz/mm per side was measured (see Fig. 76).

The preliminary measurements performed at Niowave, Inc. included the frequency spectrum measurements at room temperature in a vertical *stack-up* setup after EB welding (see Fig. 77). The measured frequency spectrum can be seen in Table 10. Additional room temperature measurements performed at ODU and Jefferson Lab will be discussed later in this chapter.

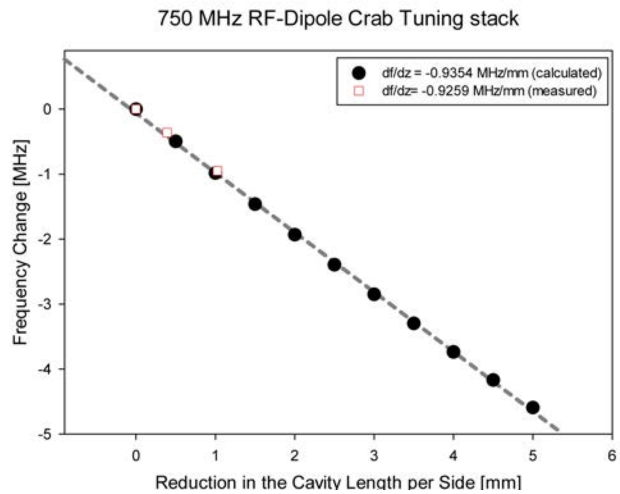

FIG. 76: 750 MHz crab cavity tuning stack calculations (black) and measured (red).

FIG. 77: Welded 750 MHz crab cavity preliminary room temperature testing.

6.1.1 BUFFERED CHEMICAL POLISHING

To remove the Nb layers damaged during forming and handling, the cavity was etched after the final welding, using a bulk buffered chemical polishing (BCP) acid mixture of HF:HNO_3:H_2PO_4 in 1:1:2 parts each. Iced bags were used to decrease and control the temperature of the acid mixture to reduce hydrogen absorption by the rf surface, the cavity was fixed vertically to a cart and the side ports were used to circulate the acid, a nominal removal of 150 μm (see Fig. 78(a)). Since all the surface processing was made at Niowave, Inc., we do not have cavity wall thicknesses, acid

TABLE 10: Measured eigenmodes at room temperature

Mode	f **[MHz]**	**Q**	**Loss [dB]**
1	749.492	5600	-53
2	1058.027	6900	-37
3	1370.410	1200	-16
4	1377.506	2000	-19

flow or etching rate measurements to present. Later surface treatments realised at Jefferson Lab will be discussed in Section 6.3.

(a) Vertical BCP (150 μm surface removal) (b) HPR after chemistry

FIG. 78: 750 MHz crab cavity during surface preparation.

After the BCP, and high pressure rinsing (HPR) with ultra pure water, the cavity was let to dry vertically inside the clean room. In a following leak check, the cavity was found to have a leak at the braze joint in one of the side ports. To fix this, the side port was cut and a Nb plug was EB welded, Figure 79 shows the plugged port from the exterior (a) and the interior (b) of the cavity. A light BCP was performed by the vendor on the cavity after EB welding of the Nb plug, with a reported nominal removal of 15 μm. The vendor realised some tests of the cavity at 4.20 K, their results will be presented in Section 6.4 as a preamble to the cryogenic tests performed at Jefferson Lab. After the testing, the cavity was carefully packed and sent to Jefferson Lab/ODU for further studies.

After receiving the shipping from Niowave, Inc., the cavity was cleansed, degreased, high pressure rinsed again, and prepared for cryo-testing at 4.20 K and

(a) External view (b) Internal view

FIG. 79: Nb plug on side port replacing leaky braze joint, view from outside (a) and inside (b).

1.99 K at the Jefferson Lab's SRF institute. The cavity was then plugged into a vacuum pumping for 3 days for a slow evacuation, after which the vacuum levels were oscillating in between 10^{-4} and 10^{-6} Torr. The cavity was suspected to have a virtual leak due to a probable volume trapped inside or dirty hardware; the test was temporary set in stand by and the cavity was vented and dissembled. One of the possible reasons for a trapped volume was the 0.22 in Niobium plug capping the side port, since the cavity had been confirmed as vacuum tight beforehand, there was no obvious reason to suspect a physical leak. In order to take a closer look of this area, the cavity was set onto a borescope and we proceeded to perform an optical inspection (see Fig. 80).

After the visual inspection we determined that even when the plugged port is not ideal for cleaning, it does not seem to represent a big problem or trapped volume for the vacuum (see Fig. 79(b)). We then proceeded to do a leak detection in several steps.

6.1.2 LEAK DETECTION AND CHARACTERISATION

Following the optical inspection and with the support of Jefferson Lab's cryomodule group, we performed a detailed leak check on the cavity, after pumping down for several hours with a turbo pump and several runs of dry nitrogen gas to try to clean

(a) Borescope setup and controls

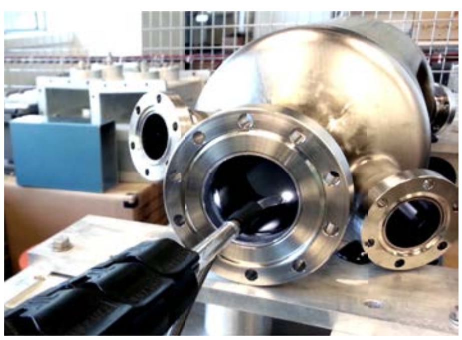

(b) Cavity inspection

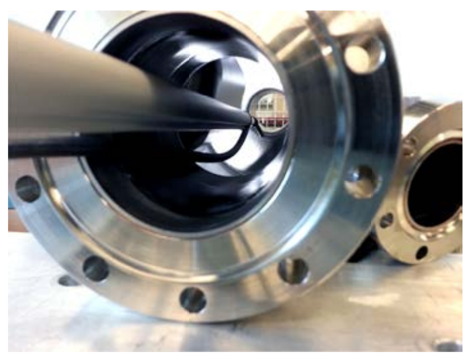

(c) Capturing images

FIG. 80: Optical inspection with borescope used to discard trapped volumes at the Nb plug.

up the cavity to reduce trapped moisture inside of the vacuum volume, the system was not able to reach vacuum levels (10^{-5} Torr) sufficient to run the mass spectrometer for residual gas analysis (RGA). Changing the copper gaskets and retightening the bolts did not solve the problem, so the cavity was switched to a Helium leak detector that works at higher pressures and is very sensitive to Helium leaks in vacuum (down to 10^{-12} Torr·l/s). Having determined a real leak in the beam port area with this system, an optical inspection was then performed using Jefferson Lab's *Kyoto-KEK* type optical bench (see Fig. 81(a)).

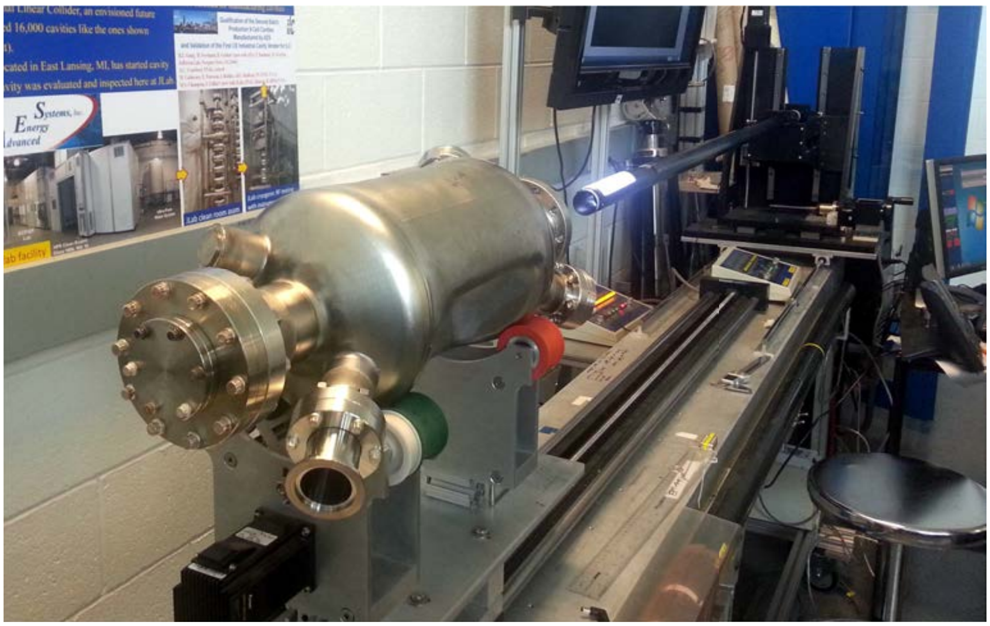

(a) Cavity on the optical bench

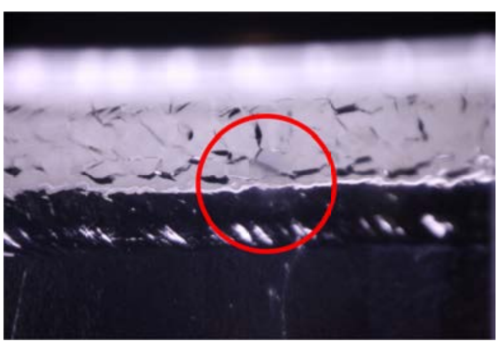

(b) Beamport weld

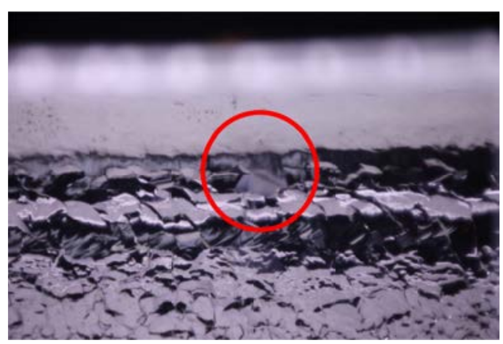

(c) Beamport weld rotated by 180°

FIG. 81: Optical inspection of the beam port welding area, consistently showing a blurry spec (b) and (c).

During the optical inspection, a small blurry spot that corresponds to the site marked up (in the outside) by the technician was found and determined as a suspect location for the leak. This spot presented a higher light dispersion than the rest of the seam, this "*blurry spot*" is characteristic of chemical residuals, it was suspected to be alcohol sprayed by the technician during the leak check that then seeped through a crack on the seam made by mechanical stresses or thermal shock during previous test or shipping (see Fig. 81(b) and (c)). The pictures shown in Fig. 81, are both taken at the same spot, changing the illumination and camera angles by 180 degrees. This reinforces the notion that is not an optical illusion due to shades or reflections on the surface but a real residual spot.

The cavity then was taken to the installations of the Center for Accelerator Science (CAS) at ODU for a more detailed leak inspection, having then carefully diagnosed that the leak was in the bracing of the beam pipe flange. After careful analysis, the decision was taken to cut out both the leaky beam port and the plugged side port and replace them with leak tight certified new ports, bought from Niowave, Inc.

6.1.3 BEAM PIPE AND PORT PIPE WELDING

After receiving the new ports, the cavity was sent to Jefferson Lab's machine shop to have the faulty ports cut out and the pipes machined for EB welding, as seen in Fig. 82 for the beam pipe port (left) and side pipe port (right).

Figure 83 shows the cavity after having the beam port welded, being mounted with the help of a customised fixture onto the EB weld chamber for welding the side port (top-left), a close up to the welded side port (top-right), and a top-down view of the cavity after repair (bottom).

6.2 ROOM TEMPERATURE MEASUREMENTS

Once repaired, the cavity was sent back to ODU for leak test to conduct a series of studies at room temperature that included bead pull measurements to determine the symmetry of the fields and couplers calibration as part of the preparations for the cryogenic tests.

6.2.1 BEAD PULL

The bead pull measurements consist of finding the frequency shift ($\left[\frac{\Delta f}{f}\right]_D$) due to the perturbation on the fields by a small dielectric (teflon) bead pulled along the cavity's longitudinal axis, the relation between the associated frequency shift and the

FIG. 82: Faulty brazed pipes machined and ready for EB welding of the new flanges.

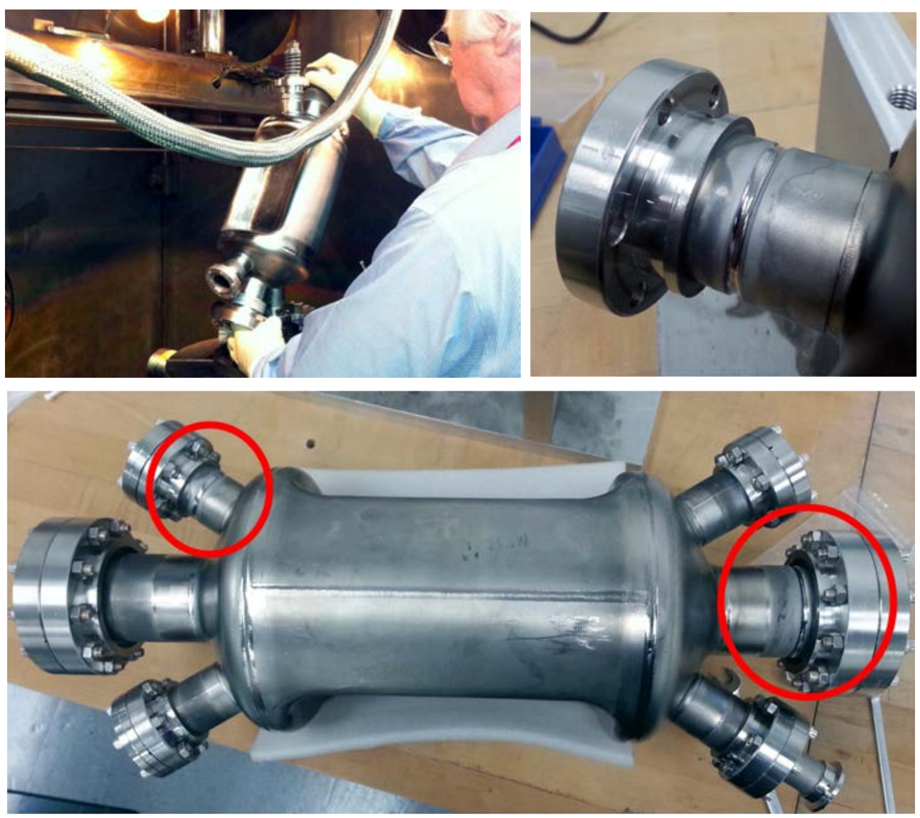

FIG. 83: The cavity was repaired at Jefferson Lab and leak checked at ODU.

transverse electric field can be related to this frequency shift using Eq. 173.

$$\left[\frac{\Delta f}{f}\right]_D = -\frac{\pi a^3}{U}\left[\left(\frac{\epsilon_r - 1}{\epsilon_r + 2}\right)\epsilon_0 |E|^2\right]. \tag{173}$$

Where a is the spherical bead radius, U the energy stored in the fields inside the cavity, ϵ_r the Teflon's relative permittivity, and ϵ_0 the vacuum permittivity. Then, for a conductor bead (brass) the frequency shift ($\left[\frac{\Delta f}{f}\right]_C$) is given by Eq. 174:

$$\left[\frac{\Delta f}{f}\right]_C = -\frac{\pi a^3}{U}\left[\epsilon_0 |E|^2 - \frac{\mu_0}{2}|H|^2\right]. \tag{174}$$

With μ_0 as the vacuum permeability. Thus, from Eq. 173 & 174 we can derive the absolute value for the fields as:

$$\begin{aligned} |E_x| &= \sqrt{\left(\frac{-U}{\pi a^3}\right)\left(\frac{\epsilon_r + 2}{\epsilon_r - 1}\right)\frac{1}{\epsilon_0}\left[\frac{\Delta f}{f}\right]_D}, \\ |H_y| &= \sqrt{\left(\frac{2U}{\pi \mu_0 a^3}\right)\left\{\left[\frac{\Delta f}{f}\right]_C - \left(\frac{\epsilon_r + 2}{\epsilon_r - 1}\right)\left[\frac{\Delta f}{f}\right]_D\right\}}. \end{aligned}$$

Figure 84(a) shows the relation of the frequency shifts for both the teflon and the brass beads, while Figures 84(b) and (c) compare respectively the extracted electric and magnetic fields from the bead pull, to the ones obtained by the CST Microwave Studio® simulations. No scale factors have been used to match the simulated fields to the measurements. It is worth mentioning that the system employed is precise enough to allow us to extract the transverse magnetic field profile fairly well, despite the small signal-to-noise ratio. The apparent slight asymmetry of the magnetic field is attributed to errors of alignment between the frequency shift curves (see Fig. 84(a)) at the moment of their subtraction to calculate the field.

In case of need to re-tune the cavity at this point, the capacitive plates could be plasticly deformed inwards to increase the capacitance and therefore lower the cavity's frequency, or the beam ports could be plasticly deformed inwards or outwards in a tuning bench, to increase or lower the frequency, respectively.

6.2.2 COUPLER ROD CALIBRATION

Copper rod electric antennas of 9.5 and 3.1 mm diameters were used as fundamental power coupler (FPC) and field probe (FP) respectively. The distance from the probes tip to the cavity end cap entrance, along with their external coupling (Q_{ext})

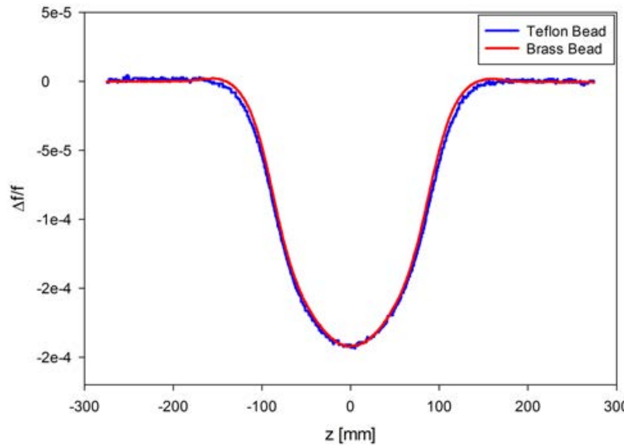

(a) Frequency shift

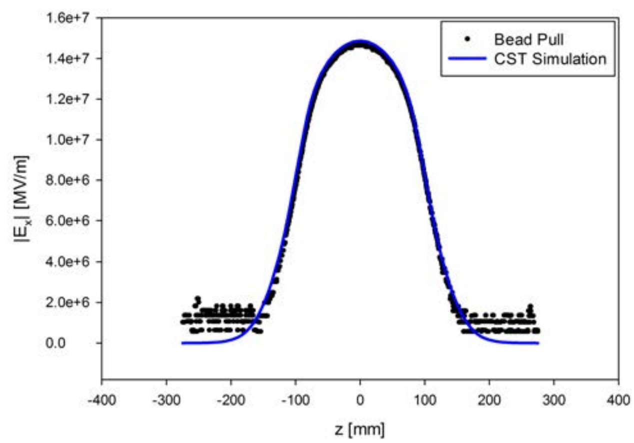

(b) Transverse electric field

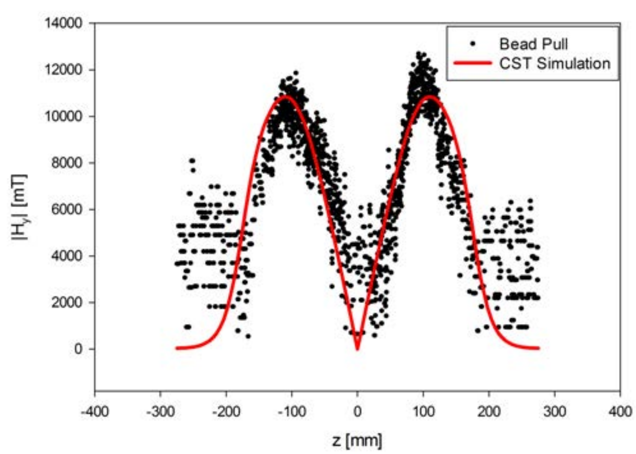

(c) Transverse magnetic field

FIG. 84: Bead pull measurements and transverse fields extracted from the numerical simulations.

were measured and recorded during the calibration. Fig. 85 shows the calibration data compared to Q_{ext} simulations on CST Microwave Studio® for perfect electric conductor rods of different diameters (see Fig. 86).

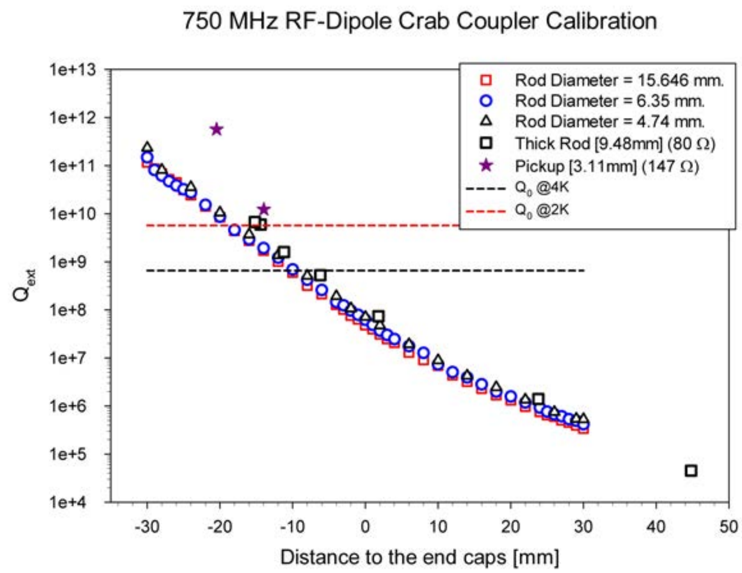

FIG. 85: Comparison of measured and simulated data for the 750 MHz crab cavity field couplers.

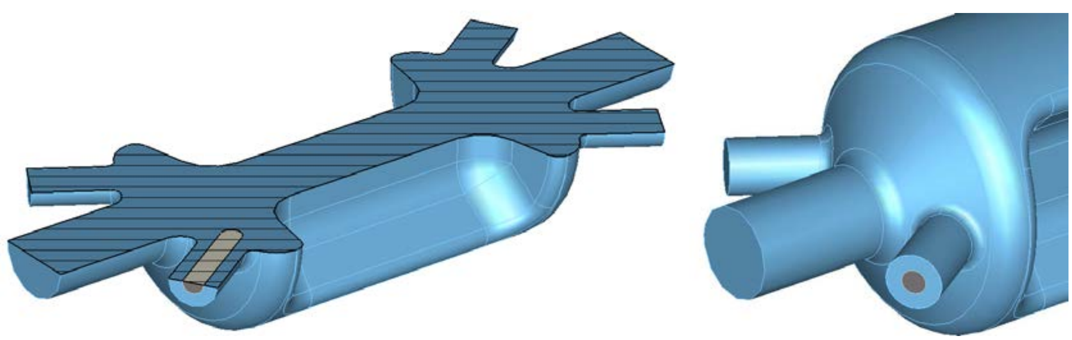

(a) Longitudinal cross section, cavity with FPC

(b) FPC rod in the side port

FIG. 86: Model used for the calculations of the Q_{ext} using CST Microwave Studio®.

Figure 85 shows the measured values of the Q_{ext} for the field probe antenna (star) and the fundamental power coupler (black square) for different lengths of the rod, compared to the Q_{ext} values obtained from simulations on CST Microwave Studio® for perfect electric conductor rods of different diameters. The dotted lines show the cavity expected Q_0 of the cavity at 4 K (black) and 2 K (red), a further discussion on the behavior of Q_0 for the cavity will be presented in the following Sections 6.3 and 6.4.

6.3 SURFACE TREATMENT

Having performed a bulk BCP on the cavity previously, and for purposes of studying the limitations and flexibility of the rf dipole structure, a 30 μm horizontal electropolishing (HEP) was performed (see Fig. 87). Due to the complexity of its geometry, the rf dipole presents some challenges for electropolishing surface etching. To address this, the employed aluminium cathode was covered with a dense teflon grid to mask its surface when the distance between this and the cavity surface (anode) was shortest, and correspondingly, making the grid less dense to expose more cathode surface as the distance to the walls was increasing, to procure uniform etching rate. Figure 88(b) shows, in black empty diamonds, the measured removal at different locations after the HEP, the highest achieved removals correlated to the points, where the distance between the cathode and the walls are shortest (i.e. points 1 and 12 in Fig. 88(a)), while the lowest removals correspond to the points placed in the farthest walls (i.e. 2 to 11 as Fig. 88(a) indicates).

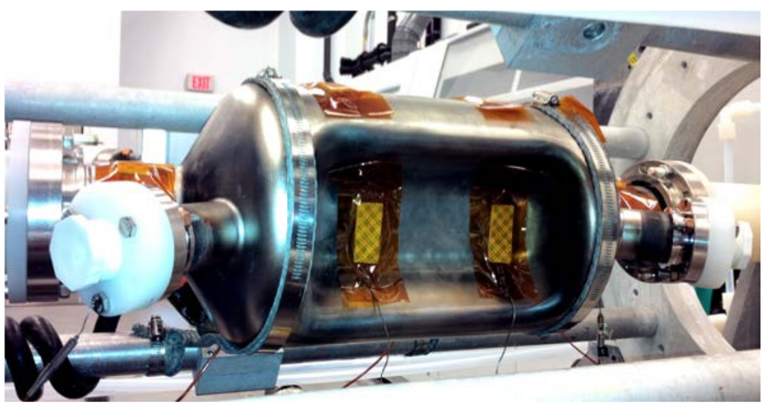

FIG. 87: Comparison of measured and simulated data for the 750 MHz crab cavity field couplers.

A flash 5 μm buffered chemical polishing (BCP) followed the HEP, with a more uniform thickness removal along the different measured points (shown in Fig. 88(b) as empty red diamonds). This proves that the rf dipole geometry favours the use of BCP, nevertheless, it perfectly allows the use of HEP with a bit of cathode customisation, which would be useful when in search of higher gradients. Figure 88(b) shows, in solid blue diamonds, the effective Nb removal at the different measured points after both

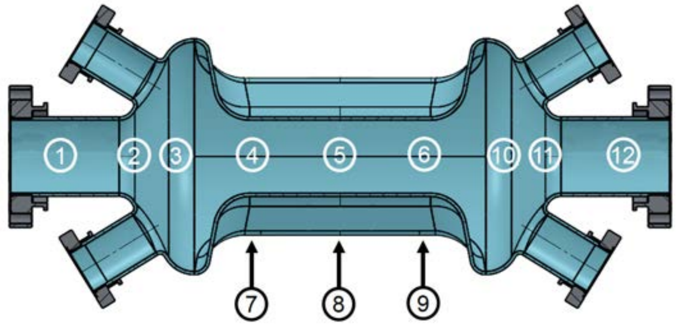

(a) Thickness measurement points

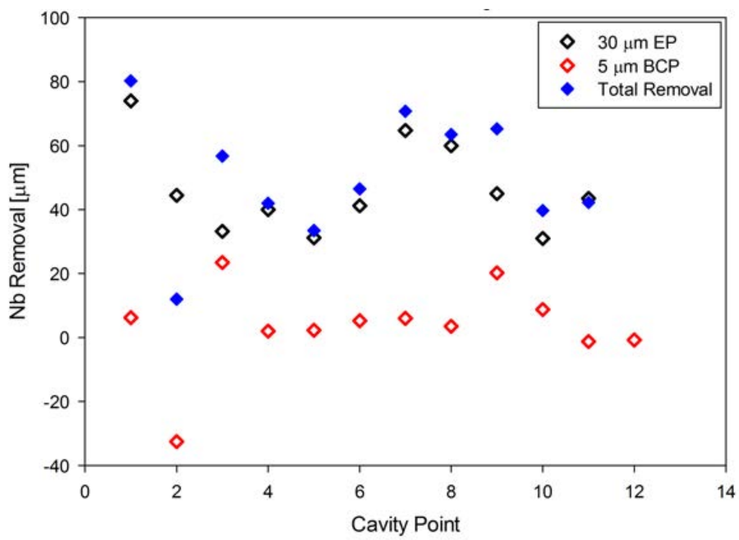

(b) Thickness removal per location

FIG. 88: Nb removal after a 30 μm HEP (empty black) and a flash 5μm BCP (empty red).

processes. Thickness measurements previous to the clean assembly were performed, followed by a thorough high pressure rinse (HPR), using deionised water at 1250 psi. After the surface treatment and clean assembly, the effective surface resistances expected were $R_S = 200\,n\Omega$ at 4 K and $R_S = 23\,n\Omega$ at 2 K, both corresponding to the unloaded quality factors of $Q_0(4K) = 6.57 \times 10^8$ and $Q_0(2K) = 5.71 \times 10^9$ respectively.

6.4 CRYOGENIC RF TEST

The cavity's quality factor "Q_0", field levels, and resonant frequency were monitored using the in-house phase locked loop (PLL) system and after placing the cavity under vacuum on the liquid Helium bath at the vertical test area in Jefferson Lab, both for 4.20 K and 1.99 K cases. Using this information we can analyse and study the cryogenic performance of the rf dipole, including: multipacting processing, quenches, field emission, Lorentz detuning, and power losses among other things.

6.4.1 SURFACE RESISTANCE

Starting from the definition of the surface resistance derived in [68](Eq. 143) from the BCS theory [40, 69]:

$$R_S = \left(\frac{A}{T}\right) f^2 e^{-\Delta/k_B T} + R_{\text{res}}\,, \tag{175}$$

where A is a material dependant constant, k_B is the Boltzmann constant, f the rf frequency, 2Δ the Nb energy gap, T is the surface temperature, and R_{res} the residual resistance.

The methodology followed to determine the residual resistance was to record the Q_0 of the cavity and the temperature of the He bath while cooling down from 4.20 K to 1.99 K, at a controlled gradient range of $E_T = 0.49$ to 1.99 MV/m. Then, using from Table 4, the geometric factor $G = 131.4\,\Omega$ and the relation:

$$R_S = \frac{G}{Q_0}\,. \tag{176}$$

The recorded R_S was plotted against the inverse of the cavity's temperature and fitted using Eq. 175, leaving A, Δ, and R_{res} as free parameters, with $k_B = 1.38 \times 10^{-4} n\Omega \cdot K \cdot s^2$ and $f = 750$ MHz, obtaining $R_s = 39.34\,n\Omega$ as shown in Fig. 89.

The residual resistance was found to be almost double as the expected $20\,n\Omega$, even when this could be due to some surface contamination, we have reasons to believe it is consistent with power losses at the S.S. flanges, similar observations have been confirmed previously with other rf dipole designs [6] and the proper calculations and discussion are presented in the *Analysis on Losses* section bellow (Section 6.5). The cavity was not baked after etching, low temperature baking could be expected to lower the Q_0, but presumably move the quench point farther up in field level [24].

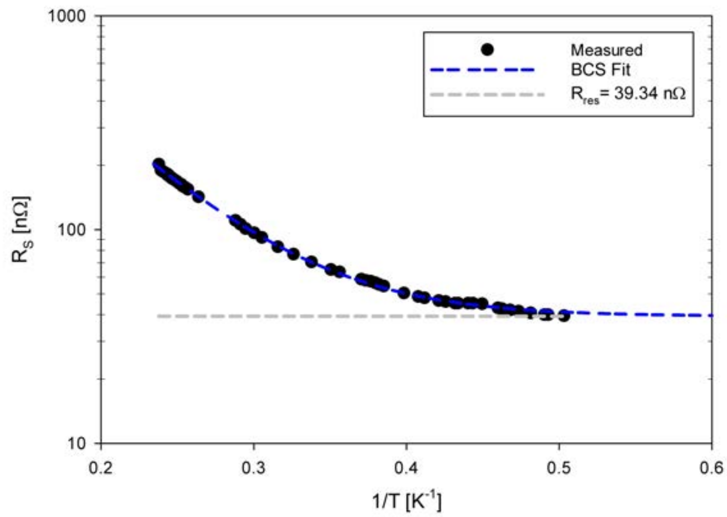

FIG. 89: Cryogenic measurements of the surface resistance.

6.4.2 PRESSURE SENSITIVITY

Another important aspect of the structure design is its relative robustness to maintain the resonant frequency within a small range while under stresses, exerted by the pressure differences between the ultrahigh vacuum inside the cavity and the He bath it is submersed into. This difference is about 11 orders of magnitude (from an inside vacuum of $\sim 10^{-9}$ to a liquid Helium bath of 755 torr).

Plotting the frequency shift as a function of the liquid Helium bath pressure during the cool down, the pressure sensitivity can be obtained by extracting the slope from a linear fit, which, in the case of the proof-of-principle (naked) 750 MHz rf dipole studied in this thesis, was found to be $\partial f/\partial P = 0.7$ kHz/torr as shown in Fig. 90. This measurement differ by about a 26% from the calculated pressure sensitivity of 0.52 kHz/torr, found by simulations using ANSYS [63], as previously discussed in Section 5.5.1. The pressure sensitivity can be easily reduced by adding properly placed stiffening elements to the cavity walls. In order to do so, structural studies using numerical tools can be performed to optimise the place and number of stiffening required, such analysis won't be discussed further in this thesis, since it is not relevant for the proof-of-principle cavity.

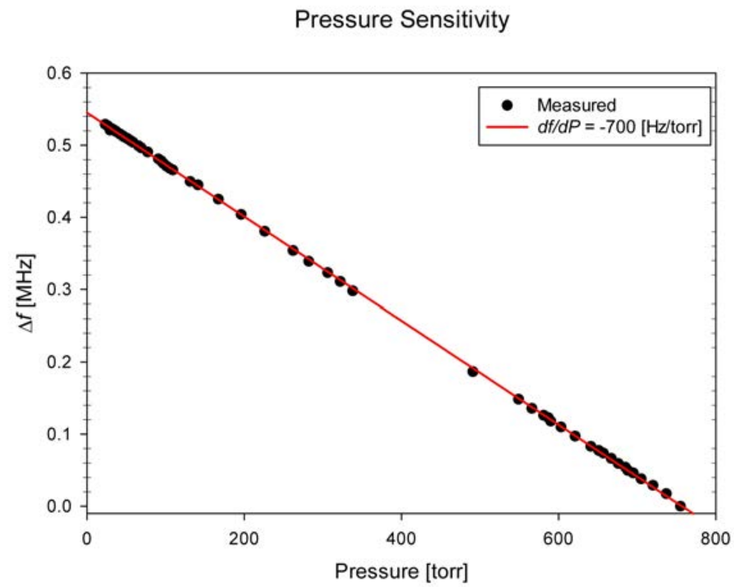

FIG. 90: Pressure sensitivity from measurements of the resonant frequency shift during the liquid Helium pump down in the Dewar (from 760 to 23 torr).

6.4.3 QUALITY FACTOR

Figure 91 shows the measured Q_0 at 4.20 K (black) and at 1.99 K (blue), as a function of the transverse electric field E_T, the transverse voltage V_T, and the electric and magnetic peak surface fields E_P and B_P respectively. The empty triangles show the radiation levels measured by the x-ray monitors placed outside the dewar.

The notorious dips on the 4.20 K (black) Q_0 curve show Q degradation due to multipacting activity, this will be discussed in more detail in the corresponding *Multipacting* section bellow (Section 6.4.5). When it comes to the 1.99 K (blue) Q_0 curve, there is no strong low field Q slope, however, an evident medium field Q slope can be noticed, as described in Padamsee, *et al* [24], this can be attributed to a non-linear surface resistance, which is a function of the magnetic field, due to grain boundaries, defects, and impurities. A thorough study on this slope may include fairly complex calculations and detailed analysis of the surface composition and structure that could be extended into a PhD thesis in itself. Thus, we will not extend any further on the matter in the present work, a reduced bibliography on this subject could include for example [70, 71, 72].

A high field Q slope appears at about E_T = 12 MV/m at 1.99 K, the ramp up

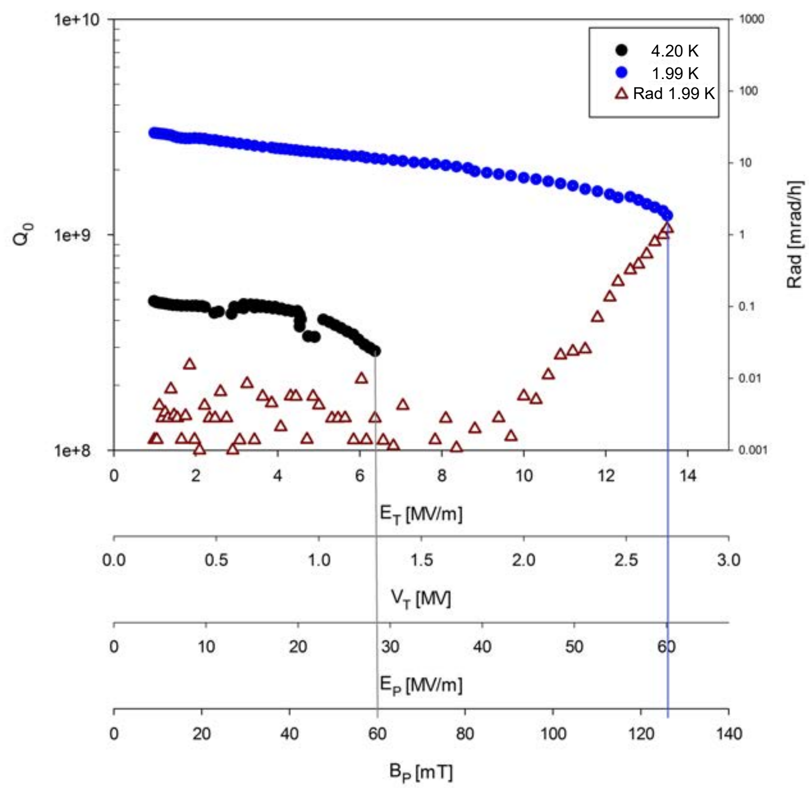

FIG. 91: Quality factor at 4.20 K (black) and 1.99 K (blue), with radiation measurements (maroon).

on the x ray emission after $E_T = 10$ MV/m may indicate activation of field emitters, which could be addressed by He processing. It is worth pointing out that a low temperature baking may push the quenching point further up in gradient. However, it is important to notice the fairly high peak surface fields reached of about $E_p = 60$ MV/m and $B_p = 125$ mT, reached at the $V_T = 2.7$ MV of deflecting voltage at 1.99 K with a very low x-ray emission ~ 1 mrad/h, which, even when not at the theoretical limits yet, are still in a high value region, showing a good performance of the cavity.

6.4.4 LORENTZ FORCE DETUNING

During operation, cavity deformations occur due to the force exerted on the walls by the radiation pressure; the contribution due to the magnetic field exerts an outwards force on the cavity walls, while the electric field contribution to the radiation pressure pushes the cavity outer conductor inwards, all this is in accordance to the Slater's theorem. Thus, resulting in a shifting (decreasing) of the resonant frequency. This frequency shift is known as Lorentz detuning, for the case of the 750 MHz rf dipole, the Lorentz coefficient k_L was determined by a linear fit to the recorded frequency shift as a function of the squared of the transverse gradient E_T^2, as can be seen in Fig. 92.

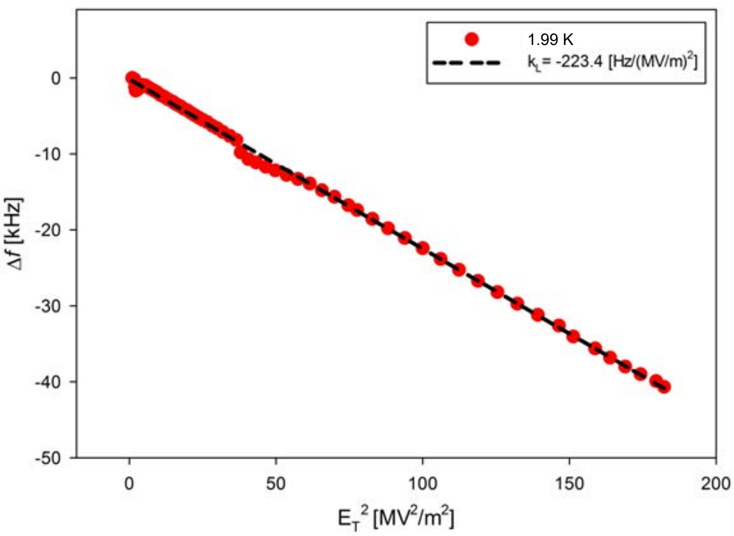

FIG. 92: Lorentz detuning measurements.

The Lorentz coefficient was experimentally found to be $k_{L,\mathrm{exp}} = -223.4$ Hz$/(MV/m)^2$, compared to the calculated value from simulations $k_{L,\mathrm{sim}} = -252.8$ Hz$/(MV/m)^2$ [as previously discussed in Section 5.5.2], shows a very good agreement within a 13% margin. The high sensitivity to the radiation pressure is due to the relatively large flat surfaces on the loading elements subjected to the high electric fields. The Lorentz coefficient can be improved by adding stiffeners in the areas of higher deformation similarly to the case of pressure sensitivity. Numerical studies are necessary to determine the mechanical properties of the structure, in order to reduce these coefficients. In the case of a proof-of-principle cavity, such as the one described in the present work, these studies are not relevant, nevertheless and depending on the applications for operating cavities, pressure sensitivity, Lorentz detuning, as well as promptness to ponderomotive effects can be of high relevance to the specifics of operation and control [73].

6.4.5 MULTIPACTING

As mentioned in the *Quality factor* section above and looking closer to the Q_0

curve obtained at 4.20 K (shown in solid black in Fig. 93), it is possible to see two clear multipacting barriers occurring at slightly above $V_T = 0.4$ MV and slightly bellow $V_T = 0.9$ MV, these barriers have a width in between 0.1 and 0.2 MV and were found to be easily broken with an increase of power, their observation reocurred with following measurements at 4.20 K. The degree of Q degradation shown depends on the amount of energy put into the multipacting process by the rf fields. Benchmarking the multipacting simulations obtained, using TRACK3P from the ACE3P suite, we observed a great consistency between the expected range of voltages for multipacting occurrence and the barriers encountered. The areas affected by multipacting at these levels are mostly the end caps and the high magnetic surface field area on the outer conductor (cavity's top and bottom, so to speak). Also, from the simulations we observed that predominantly there is 1st and 2$^{\mathrm{nd}}$ order multipacting for this geometry.

It can be suspected, primarily the 1$^{\mathrm{st}}$ order multipacting (shown as red empty circles in Fig. 93), since this is the fastest process to put energy into from the rf fields, also seems to be consistent with the field levels at which the barriers were observed. At 1.99 K the two barriers were observed in the same voltage levels as expected, but after the first gradient sweep, they were successfully cleaned up and they were not observed again. Higher voltage barriers were neither predicted by the simulations nor observed during the test (see the 1.99 K Q_0 curve (blue) in Fig. 91).

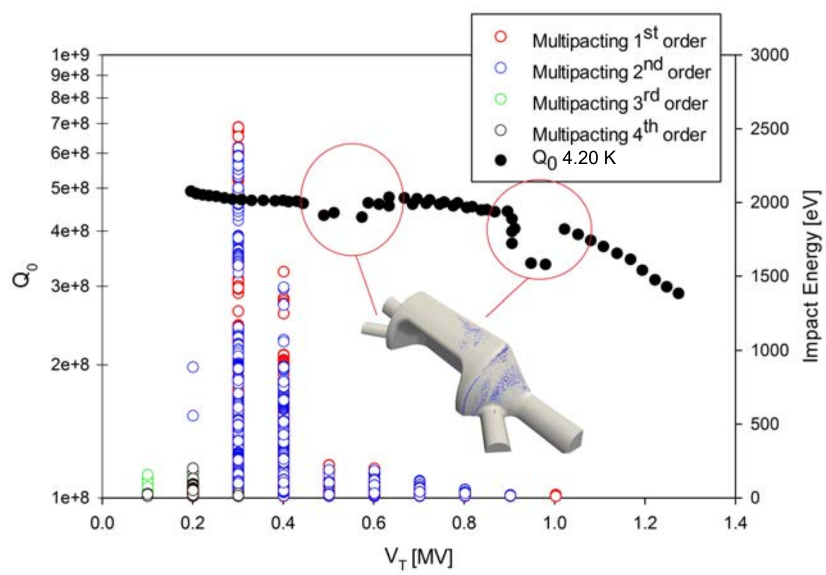

FIG. 93: TRACK3P simulation (empty dots) and multipacting barriers encountered during the test at 4.20 K (solid dots).

6.5 ANALYSIS ON LOSSES

In this section, we calculate the power dissipated on the flanges due to Ohmic losses generated by the residual magnetic field at their location. In order to do this, we will consider the total loss as the sum over the 2 beam pipes and the 4 auxiliar ports' flanges. The time-averaged power dissipated at the flanges per unit area due to the rf fields can be expressed as:

$$\frac{dP_{\text{loss}}}{dA} = \frac{R_S}{2}|\mathbf{H}_{||}|^2\,, \tag{177}$$

then, the dissipated power by one of the flanges is:

$$P_{\text{loss}} = \frac{R_S}{2}\iint |\mathbf{H}_{||}|^2 dA\,. \tag{178}$$

For the rf dipole's fundamental mode, $\mathbf{H}_{||}$ corresponds to $\mathbf{H}_y$, while the integral is bounded to the area A of the flanges exposed to the fields. R_S is the resistance presented to the rf fields by the flanges' surface and can be expressed in terms of the material's conductivity σ_m and the rf frequency ω as shown in Eq. 179.

$$R_S = \sqrt{\frac{\mu_0\omega}{2\sigma_m}}\,, \tag{179}$$

where m is only an indicator that refers to copper (Cu) or stainless steel (S.S.).

The 3D fields were extracted from the CST Microwave Studio® simulations, a script to calculate the numerical area integral of the field at the flanges location was written using *Visual Basic*. The quality factors associated to the total power dissipated by all the flanges ΣP_{loss} can be calculated using Eq. 180 and the results are presented in Table 11.

$$Q_0 = \frac{\omega U}{\Sigma P_{\text{loss}}}\,. \tag{180}$$

TABLE 11: Power Dissipated by the Flanges at $U = 1$ J

Material	σ_m **[S/m]**	ΣP_{loss} **[W]**	Q_0
Copper	5.80×10^{7}	0.2265	2.08×10^{10}
Stainless Steel	1.45×10^{6}	1.4324	3.29×10^{9}

The goal Q_0 shown in Fig. 94 (star) was calculated using Eq. 176, for $R_{\text{res}} = 20\,n\Omega$ and $R_{BCS} = 4\,n\Omega$ at 2 K. The measured Q_0 at 1.99 K (see Fig. 94 (blue)) is very close to the expected value when the power dissipation is dominated by the losses at the

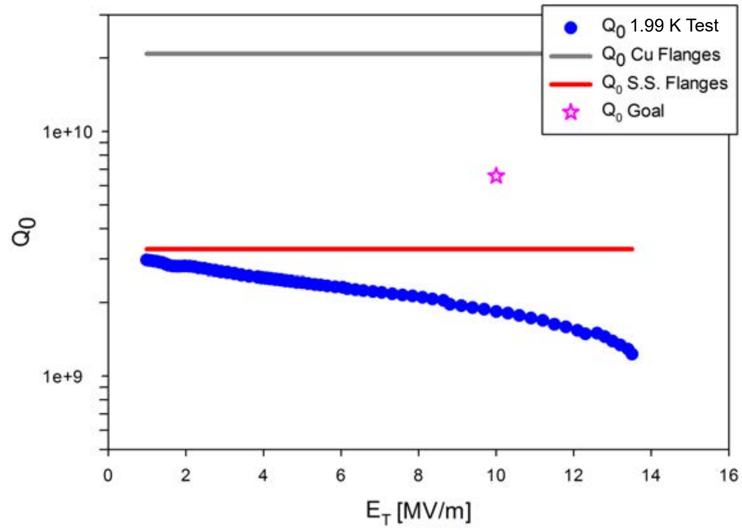

FIG. 94: Measured Q_0 for the cavity (blue), Q_0 associated with the losses on the flanges for Cu (grey) and S.S. (red).

stainless steel flanges, shown as a red line in Fig. 94. Then, presumably, changing to copper or copper-coated flanges, should avoid any limitations to reach the expected Q_0 value due to undesirable losses, as shown by the grey line in Fig. 94. This result presents speculative arguments to explain why the Q_0 measured at 1.99 K is lower than the value correspondent to the expected residual resistance, but would need to be confirmed in the future with a new cryogenic test beyond the scope of this thesis.

CHAPTER 7

CONCLUSIONS

7.1 PROTOTYPE DESIGN AND PERFORMANCE

A compact proof-of-principle superconducting crab cavity was fabricated by Niowave, Inc. based on the 750 MHz rf dipole design developed as part of this thesis work. This prototype was tested in several occasions, both in Niowave, Inc. and Jefferson Lab's vertical testing areas (VTA). Two multipacting barriers at low transverse voltage levels ($V_T < 1$ MV) were observed at both 4.2 K and 2.0 K cryotests, but found to be easily processed and eliminated at 1.99 K. Figure 95 shows a comparison between the Q_0 data with multipacting events taken during the cryotest at Jefferson Lab's [74] and the multipacting levels obtained from the simulations, showing a very good agreement.

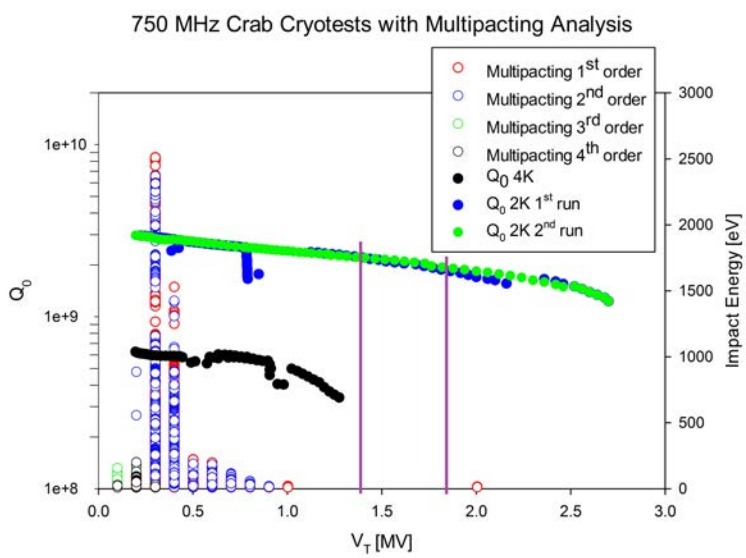

FIG. 95: Q_0 data at 4.20 K (solid black) and 1.99 K before (solid blue) and after (solid green) processing of multipacting, compared to the multipacting levels obtained from simulations (open circles). The purple lines define the operating voltage range per cavity.

In this thesis, we studied the effects on the resonant locations and incident energies for multipacting condition on the 750 MHz rf dipole due to variations of the geometrical parameter *extrusion length* of the cavity end-caps (l), for a range between 20 mm to 50 mm. We presented a subset of the studied models to illustrate the variations in the location and density of resonant particles in the cavity structure using the parameter l as tweaking knob. Even when the multipacting barriers appear at roughly the same field levels in all our simulations, the density of the resonant particles and their impact energy decrease and also the resonant positions relocate to potentially less problematic areas of the structure for larger values of the parameter l. We compared the simulation results with the experimental observation of multipacting events for the 750 MHz rf dipole prototype with considerably good agreement. We concluded that by modifying the extrusion length, the multipacting can be tweaked for the case of the rf dipole, but one should always keep in mind that by doing this, the cavity becomes longer and physical space restrictions for machine integration may apply. It is necessary to carry out further studies to determine if a different parameter can also be used to lower further the mutipacting levels in the rf dipole geometry, such as the blending radius of the end-caps, which consistently showed to be one of the locations most susceptible to multipacting. However, the experimental data has proven that multipacting is easily processed and is not a limiting factor in the rf dipole performance, not just for the 750 MHz prototype, but for the 400 MHz and the 499 MHz prototypes as well [6].

Bead pull measurements were presented in agreement with the numerical simulations. The surface resistance analysis showed to be consistent with losses on the stainless steel flanges, suggesting the use of copper flanges to reach a better Q_0 at 1.99 K, for the 750 MHz rf dipole in the—high Q—vertical test. The pressure sensitivity and the Lorentz detuning of the bare proof-of-principle cavity were found to be $df/dP = -0.7$ kHz/torr and $k_L = -223.4$ Hz/$(MV/m)^2$ respectively, compared to the calculated values of $df/dP = -0.52$ kHz/torr and $k_L = -258.8$ Hz/$(MV/m)^2$.The field levels achieved in the 1.99 K test were considerably high, $E_T = 13.5$ MV/m for the transverse gradient, with peak surface fields of $E_p = 60$ MV/m and $B_p = 126$ mT which are fairly close to the practical limits, all of these for a transverse voltage of $V_T = 2.7$ MV before quench.

7.2 BEAM DYNAMICS REMARKS

The design strategy of the Medium Energy Electron-Ion Collider (MEIC) at Jefferson Lab considers both the matching of the beam spot sizes at collision and a

50 mrad crossing angle along with crab crossing scheme for both electron and ion beams over the energy range ($\sqrt{s} = 20 - 70$ GeV) to achieve high luminosities at the interaction points. However, the desired locations for placing the crabbing cavities may include regions, where the transverse degrees of freedom of the beams are coupled with variable coupling strength that depends on the collider rings' magnetic elements (solenoids and skew quadrupoles). In this thesis, we explored the feasibility of employing *twin* rf dipoles that produce a variable direction crabbing kick to account for a range of transverse coupling of both beams.

We proved analytically that an orthonormal transverse basis—at the interaction point—back propagated towards the crabbing cavity location considering a solenoid, will still be orthonormal, but rotated by an angle that depends on the solenoid strength as $\theta_{\text{coup}}(B_{Sol}) = KL$. Thus, for the MEIC in the case of electrons at 5 GeV, this angle changes from 0 to $\sim \frac{\pi}{8}$ for a solenoid magnetic induction $B_{Sol} \leq 5$ T. Also, it is important to remark that all the contributions due to the angles and energy spreads have been neglected from the calculations for simplicity, since—for the purpose of studying the twin crab scheme—we did not propagate 6D bunch distributions, but merely the 2D transverse coordinate system as a first approximation. We concluded that for the Jefferson Lab's Electro-Ion Collider a scheme of *twin* crabbing cavities that provides the proper kick for several angles in the necessary range for the various solenoid strengths is feasible and the extra solenoid focusing has to be compensated by the FFB to avoid a maximum error on the crabbing angle of $\sim 7\%$ for electrons and $< 0.1\%$ for protons. Further studies will require consideration of the higher order contributions of the magnetic elements and particle tracking analysis.

The impact on the beam dynamics of Jefferson Lab's Electron-Ion Collider, due to the multipole content of the 750 MHz crab cavity, was studied using thin multipole elements for 6D phase space particle tracking in ELEGANT. Target values of the sextupole component for the cavity's field expansion were used to perform preliminary studies on the proton beam stability, when compared to the case of pure dipole content of the rf kicks. Finally, important effects on the beam sizes due to non-linear components of the crab cavities' fields were identified and some criteria for their future study were proposed, concluding that more detailed long-term tracking—for several thousand turns—needs to be done to fully insure beam stability during operations.

The lattice model proposed for particle tracking studies hereby presented has proven to properly describe the transverse and longitudinal dynamics of the MEIC proton storage ring. Also, rf crab cavities were successfully implemented to account for a relative 25 mrad crabbing angle of the 60 GeV proton bunches at the interaction point, showing effects of small phase advance errors between the crab cavities that are consistent with previous analytical calculations. The stability of the longitudinal beam size growth, due to the induced emittance exchange, needs to be studied for a sufficient amount of turns, both for the case of pure dipole and sextupole components to ensure stable operation conditions and to establish multipole budgets for the rf crab cavities on the MEIC. These criteria are—in general—applicable to any Electron-Ion Collider, provided that the proper lattice design is implemented for the analysis.

7.3 SUMMARISING

We studied extensively the rf dipole geometry, with specific applications at 750 MHz. The electromagnetic optimisation process—using a few geometric parameters—showed to be consistent to previous rf dipole designs developed at Old Dominion University. An important remark was made about the necessary trade off between the rf performance and the machine constraints—both from the machine integration and the beam dynamics point of view—when finalising a cavity design. But most important is the fact, that from the present studies we can conclude that the rf dipole is a very suitable compact design for crabbing applications, both for electron and proton species, at low, medium, and high energies for the future high luminosity machines.

CHAPTER 8

FUTURE WORK

8.1 AN IMPORTANT CHANGE

After the *Nuclear Science Advisory Committee Electron-Ion Collider Cost Estimate Sub-Committee* evaluated the preliminary cost estimate for Jefferson Lab's Electron-Ion (JEIC) proposal in January, 2015, the baseline for the accelerator fixed some major changes. Amongst the most relevant—from the view point of the present work—is the fact that the rf frequency has changed from 750 MHz to 476 MHz. This due to the fact that, in order to reduce the costs of fabrication, the JEIC will reuse hardware—magnets, vacuum chambers, rf cavities, and rf sources—from the PEP-II High Energy Ring (HER). The HER beam line and a 476 MHz accelerating cavity can be seen in Fig. 96.

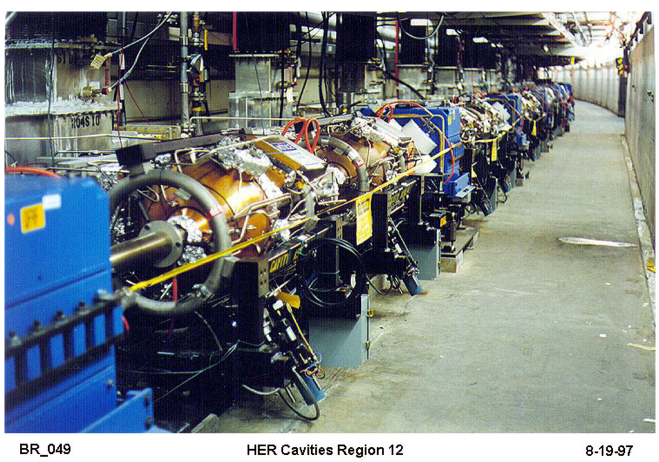

(a) Rf section in PEP-II

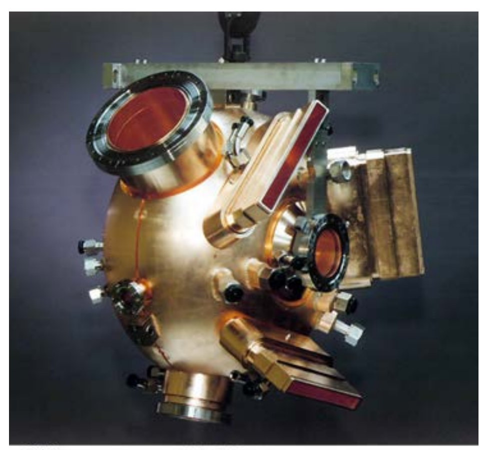

(b) 476 MHz Cu cavity

FIG. 96: Rf elements from PEP-II to be used for the JEIC (Images courtesy of SLAC PEP-II archives).

This decision was taken after careful cost studies and lattice analysis. Probably the biggest changes derived from this, were on the ion lattice design: the exchange of the pre-booster (3 GeV) and booster (10 GeV) for a single figure-8 booster based in super ferric magnets as the new baseline, along with the 476 MHz bunch repetition. But it is worth to say that for the case of developing a crabbing system, these changes, even when leaving the 750 MHz option obsolete, they also open two *new doors*: a 476 MHz or a 952 MHz bunch repetition rate—and with that—the opportunity to explore several criteria which one should consider when choosing the final frequency. This chapter intends to present a reduced list of aspects to take into account when choosing and designing the new repetition frequency, from the rf point of view. I hope that all *lessons learned* during the development of this thesis will be of good help to those developing the final crabbing system for the JLEIC and other future high luminosity colliders.

8.2 ELLIPTICAL VS COMPACT

To have a general point of comparison, a quick optimisation was made, using two different squashed elliptical geometries—inspired by the KEK crab cavity original design—and the rf dipole geometry. For this, the designs were scaled to fit the desired frequencies, keeping the beam aperture to 60 mm in all the cases, this is important due to the—previously discussed in Section 5.1.1—shunt impedance dependency with respect to ratio of the beam aperture to the rf half-wavelength ($d/\lambda_{\mathrm{rf}}/2$). Figure 97 shows the shunt impedance dependency to $d/\lambda_{\mathrm{rf}}/2$ for different models, the description of these models will be given shortly after.

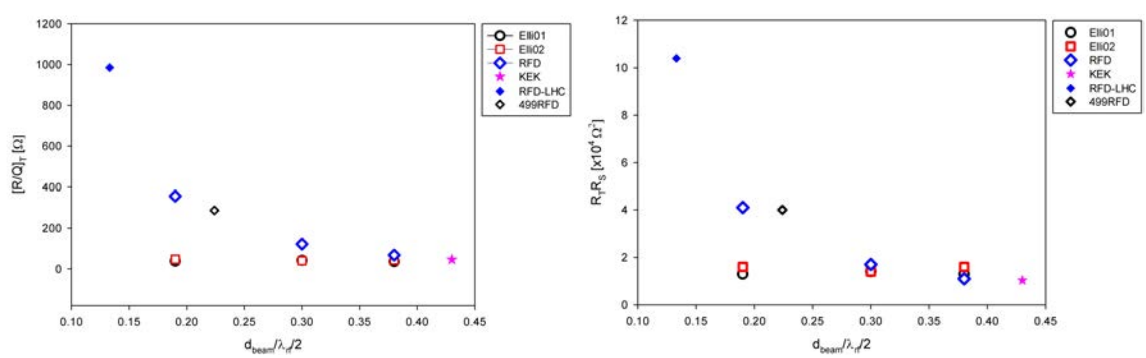

(a) R/Q (b) $(R/Q) \cdot G$

FIG. 97: Comparing the impedances for different models, including the KEK 500 MHz crab cavity (star), the 400 MHz rf dipole (blue solid diamond), and the 499 MHz rf dipole (open black diamond).

Figure 97 is very helpful to understand the performance dependance of the crab cavities with respect to their dimensions. For example, it becomes obvious that for larger values of the $d/(\lambda_{\mathrm{rf}}/2)$ ratio ($\sim$0.3), the transverse shunt impedance of the rf dipole geometry becomes comparable to the elliptical design—at least for this very *simple* analysis. However, the message should be that for higher frequencies, more refined optimisation of the rf dipole needs to be performed. Recently, H. Park *et al.* presented optimised versions of the rf dipole for 476 and 952 MHz, showing promising improved properties and explore as well as the possibility of using multi cell cavities for high frequency applications of the rf dipole [75]. Other examples of multi-cell, high frequency deflecting structures, have been studied and developed by Z. A. Conway *et al.* in Argonne National Lab [76].

8.2.1 A MATTER OF SCALE

By doing this *scaling* exercise, we can get a general idea of the strengths and weaknesses of compact structures, such as the rf dipole. For instance, even when the transverse dimension of all the cavities will scale linearly with the rf wavelength λ_{rf}, the scaling factor for the elliptical cavities is considerable bigger than the one of the rf dipole, and therefore going to lower frequencies with elliptical cavities will considerably increase the cavity size and volume, posing restrictions both to machine integration and cooling systems—in the case of superconducting cavities. Figures 98 to 100 show qualitatively the scale difference between the two elliptical geometries and the rf dipole, for three different frequencies, keeping a constant beam aperture. As it can be seen, the difference can be substantial, showing one of the advantages of the compact structures.

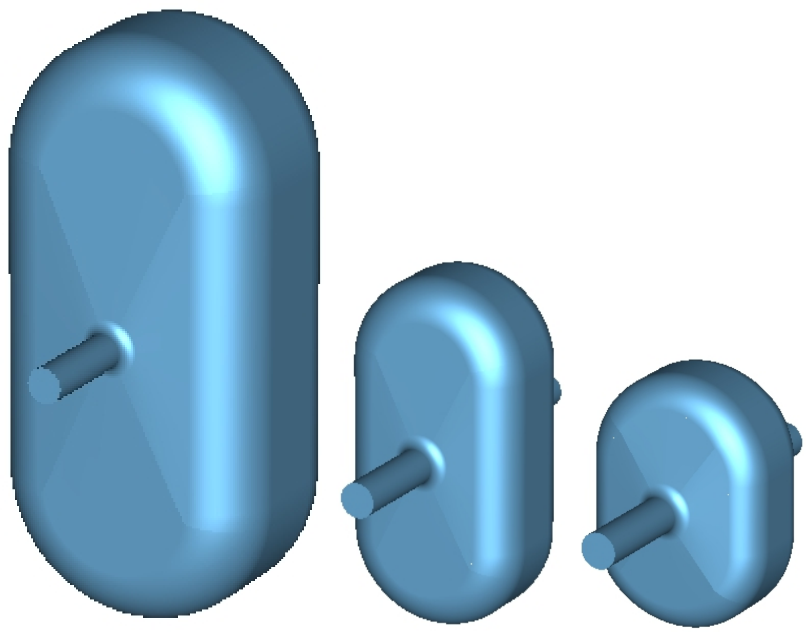

(a) 476 MHz (b) 750 MHz (c) 952 MHz

FIG. 98: Elliptical-01 design for crabbing.

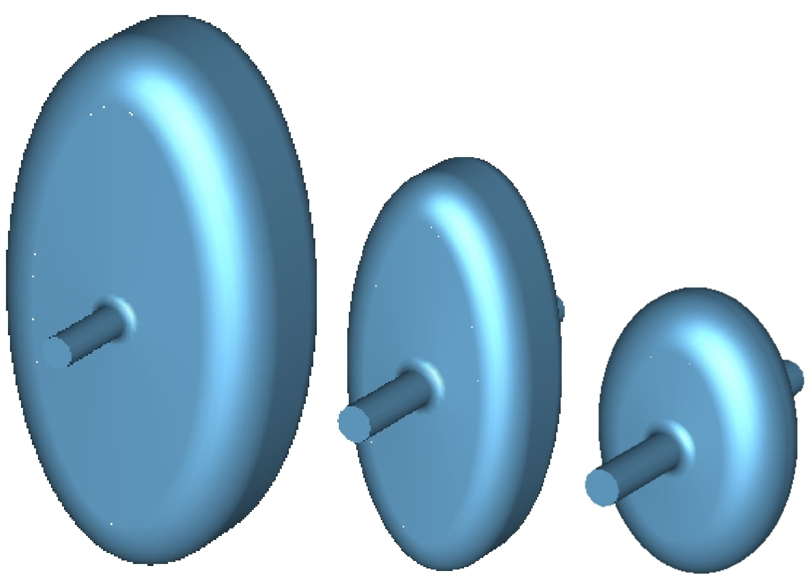

(a) 476 MHz (b) 750 MHz (c) 952 MHz

FIG. 99: Elliptical-02 design for crabbing.

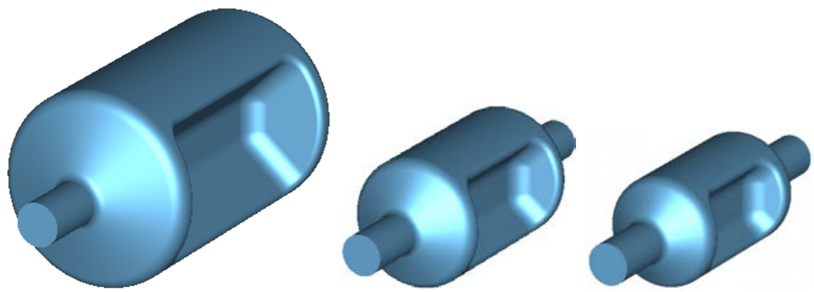

(a) 476 MHz (b) 750 MHz (c) 952 MHz

FIG. 100: RF dipole design for crabbing.

8.2.2 A MATTER OF FIGURES

There are different operational aspects to consider in the crabbing systems, when changing the collision frequency of a collider. The most relevant ones are: the voltage needed to crab the bunches, the cavity's physical dimensions (including fabrication tolerances and integration restrictions), rf performance, impedance budget, extraction of higher order modes, etc. Again, to get a general idea of the differences on the figures of merit between the squashed elliptical and the rf dipole geometries, Some quick comparisons were made; Fig. 101 shows the peak surface fields for the different models, while Fig. 102 shows the cavity impedances.

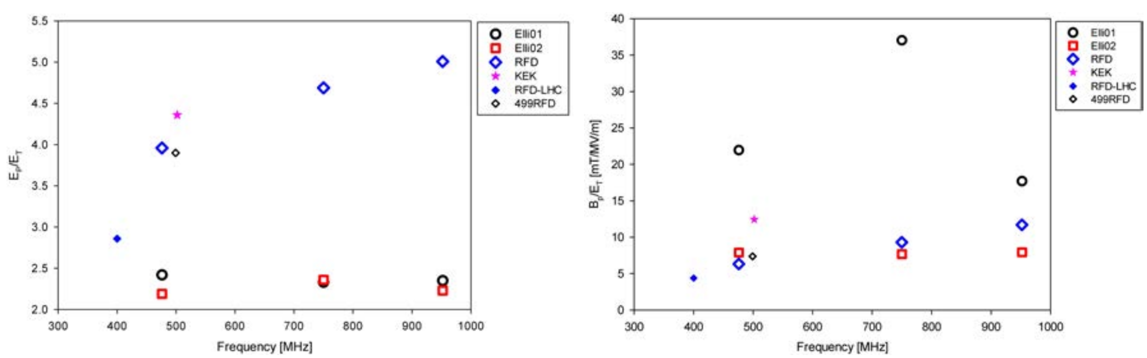

(a) Peak surface electric field (b) Peak surface magnetic field

FIG. 101: Peak surface fields for the different models.

Some of these analyses could be misleading if we do not take into account that this simple *scaling* of the geometries is not entirely correct, due to small features such as the beam aperture diameter typically needed for HOM damping in elliptical

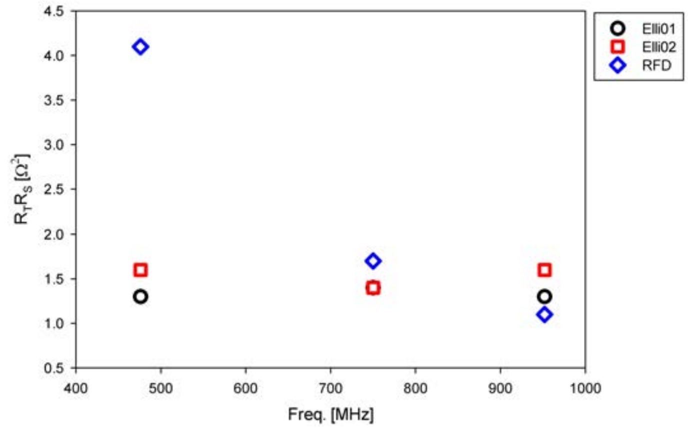

FIG. 102: Impedances for the different models studied in this chapter.

structures, etc. that will show detrimental effects in their properties. However, it gives us a general idea of the representative figures of merit. Having said that, in Fig. 101 we observe that for this rough approach, the rf dipole shows higher peak surface fields than the elliptical cavities, while the rf dipole shows considerably higher shunt impedance. For frequencies higher than 750 MHz, it starts to be comparable to the elliptical geometries if no further optimisation is performed on them. The latter can be solved by following [75].

8.2.3 A MATTER OF RESISTANCE

Another practical detail—that even when arguably less important—that is easily overlooked, is the frequency dependence on the cavity's surface resistance. Figure 103 shows, in a *log-log* plot, the surface resistance of pure untreated niobium for different frequencies and cryogenic temperatures.

From this plot, we can see that at a fixed temperature, the difference between 476 MHz and 952 MHz correspond to an increment on the surface resistance of about a factor of ∼3. This will reduce the expected Q_0 of the cavity by a factor ∼3 by following the relation $Q_0 = G/R_s$ and neglecting the residual resistance contribution (R_{res}). One should not forget that at lower temperatures the R_{res} term becomes more dominant than the BCS term in the surface resistance ($R_s = R_{\text{BCS}} + R_{\text{res}}$).

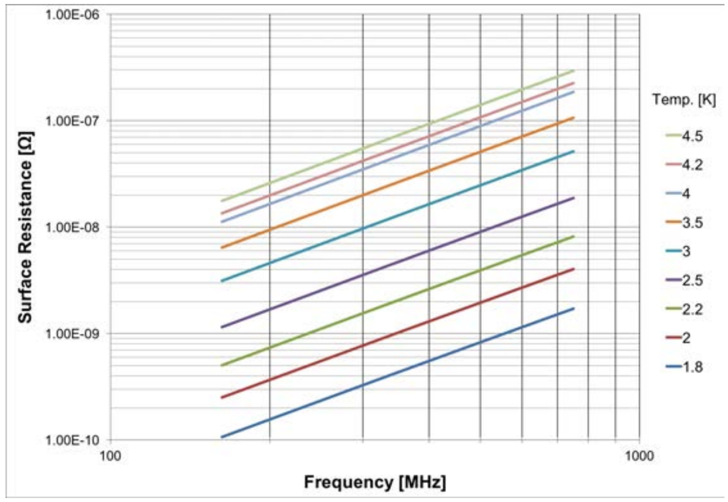

FIG. 103: Nb surface resistance as a function of frequency for different temperatures.

8.2.4 A MATTER OF VOLTAGE

We have seen in Section 2.3 that the total crabbing voltage V_T needed to correct for a crossing angle θ_c depends on the bunch frequency ω_{b}, or $V_T = \frac{cE_b \tan(\theta_c/2)}{\omega_{\mathrm{b}}\sqrt{\beta_x^* \beta_x^c}}$. This means that the crabbing voltage needed will increase inversely proportional to the crab cavity frequency. Figure 104 shows the crabbing voltage V_T as a function of the beta function of the beams at the location of the crabs (β_x^c), for both species, to understand better the impact of the different frequencies on the requirements.

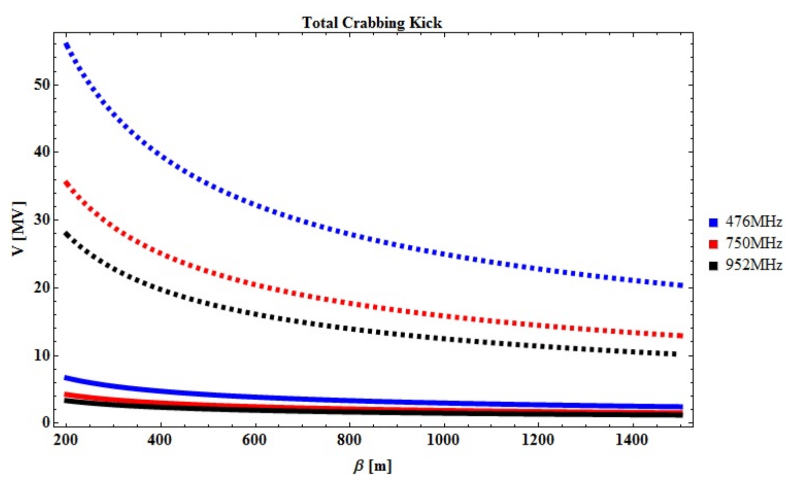

FIG. 104: Crabbing voltage needed to correct for 50 mrad, as a function of the beam β at the crab cavity location, for electrons (solid) and protons (dashed).

Perhaps a more useful plot would be the total number of cavities needed to correct for the 50 mrad of crossing angle. One could calculate this by using the results from the cryogenic test of the 750 MHz rf dipole (see Section 6.4.3), more specifically the peak surface fields reached by the proof-of-principle cavity at 2 K (i.e. $E_p = 60$ MV/m and $B_p = 125$ mT), and finding the correspondent V_T for the 476 and 952 MHz that could be reached at this peak surface fields, respectively. Figure 105 presents—as a back-of-the-envelope estimation—the number of cavities needed to provide the necessary crabbing kick to correct the 50 mrad crossing angle, for both electron and proton species, for the different rf dipole frequencies and as a function of the beam β_x^c at the crabbing location.

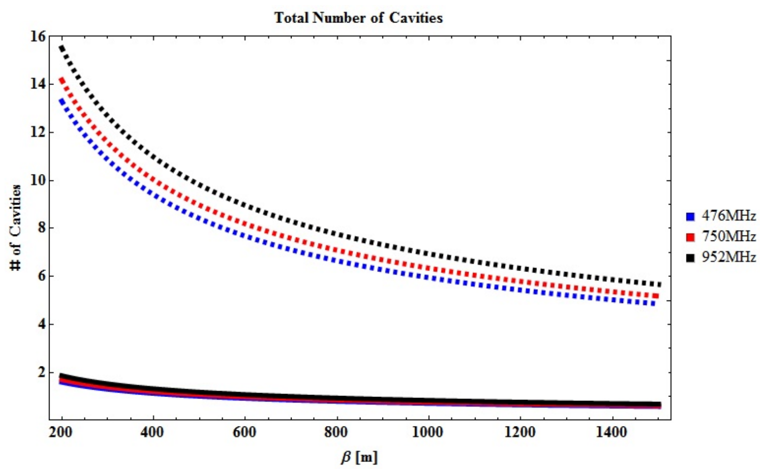

FIG. 105: Number of cavities needed to correct 50 mrad crossing angle for different repetition frequencies, as a function of the beam β at the crab cavity location, for electrons (solid) and protons (dashed).

It is essential to underline, that these numbers are not final, especially due to the quick nature of the analysis presented in this chapter. However, this sets the general idea of the first steps to take into account for the future work on finalising the JEIC crabbing systems. Not all the numbers presented here—for the 750 MHz are dipole—are directly scalable, but the methods presented for its design and optimisation, are completely generic for this geometry and can, therefore, be used as guideline for other rf dipole designs, after applying the proper machine dependent constraints.

BIBLIOGRAPHY

[1] A. Puckett, "The 6 GeV TMD Program at Jefferson Lab," vol. 21, pp. 8–11, 2015.

[2] C. S. Hopper and J. R. Delayen, "Superconducting spoke cavities for high-velocity applications," *Phys. Rev. ST Accel. Beams*, vol. 16, p. 102001, Oct 2013.

[3] M. Borland, "Simulation and analysis of using deflecting cavities to produce short x-ray pulses with the Advanced Photon Source," *Physical Review Special Topics - Accelerators and Beams*, vol. 8, no. 7, pp. 1–18, 2005.

[4] T. Abe, K. Akai, M. Akemoto, A. Akiyama, M. Arinaga, K. Ebihara, K. Egawa, A. Enomoto, J. Flanagan, S. Fukuda, H. Fukuma, Y. Funakoshi, K. Furukawa, T. Furuya, K. Hara, T. Higo, S. Hiramatsu, H. Hisamatsu, H. Honma, T. Honma, K. Hosoyama, T. Ieiri, N. Iida, H. Ikeda, M. Ikeda, S. Inagaki, S. Isagawa, H. Ishii, A. Kabe, E. Kadokura, T. Kageyama, K. Kakihara, E. Kako, S. Kamada, T. Kamitani, K. Kanazawa, H. Katagiri, S. Kato, T. Kawamoto, S. Kazakov, M. Kikuchi, E. Kikutani, K. Kitagawa, H. Koiso, Y. Kojima, I. Komada, T. Kubo, K. Kudo, N. Kudo, K. Marutsuka, M. Masuzawa, S. Matsumoto, T. Matsumoto, S. Michizono, K. Mikawa, T. Mimashi, S. Mitsunobu, K. Mori, A. Morita, Y. Morita, H. Nakai, H. Nakajima, T. T. Nakamura, H. Nakanishi, K. Nakanishi, K. Nakao, S. Ninomiya, Y. Ogawa, K. Ohmi, S. Ohsawa, Y. Ohsawa, Y. Ohnishi, N. Ohuchi, K. Oide, M. Ono, T. Ozaki, K. Saito, H. Sakai, Y. Sakamoto, M. Sato, M. Satoh, K. Shibata, T. Shidara, M. Shirai, A. Shirakawa, T. Sueno, M. Suetake, Y. Suetsugu, R. Sugahara, T. Sugimura, T. Suwada, O. Tajima, S. Takano, S. Takasaki, T. Takenaka, Y. Takeuchi, M. Tawada, M. Tejima, M. Tobiyama, N. Tokuda, S. Uehara, S. Uno, Y. Yamamoto, Y. Yano, K. Yokoyama, M. Yoshida, M. Yoshida, S. Yoshimoto, K. Yoshino, E. Perevedentsev, and D. N. Shatilov, "Compensation of the Crossing Angle with Crab Cavities at KEKB," in *Conf.Proc.*, vol. C070625, p. 27, 2007.

[5] A. Barachetti and et al., "FP7 High Luminosity Large Hadron Collider Design Study: Final Project Report," Tech. Rep. CERN-ACC-2016-0007, CERN, 2016. CERN HiLumi LHC Publication.

[6] S. U. D. Silva, *Investigation and Optimization of a New Compact Superconducting Cavity for Deflecting and Crabbing Applications*. PhD thesis, Old Dominion University, 2014.

[7] J. Dudek, R. Ent, R. Essig, K. S. Kumar, C. Meyer, R. D. McKeown, Z. E. Meziani, G. A. Miller, M. Pennington, D. Richards, L. Weinstein, G. Young, and S. Brown, "Physics opportunities with the 12 GeV upgrade at Jefferson Lab," *European Physical Journal A*, vol. 48, no. 12, pp. 1–34, 2012.

[8] S. Abeyratne, A. Accardi, S. Ahmed, D. Barber, J. Bisognano, A. Bogacz, A. Castilla, P. Chevtsov, S. Corneliussen, W. Deconinck, P. Degtiarenko, J. Delayen, Y. Derbenev, S. DeSilva, D. Douglas, V. Dudnikov, R. Ent, B. Erdelyi, P. Evtushenko, Y. Filatov, D. Gaskell, R. Geng, V. Guzey, T. Horn, A. Hutton, C. Hyde, R. Johnson, Y. Kim, F. Klein, A. Kondratenko, M. Kondratenko, G. Krafft, R. Li, F. Lin, S. Manikonda, F. Marhauser, R. McKeown, V. Morozov, P. Nadel-Turonski, E. Nissen, P. Ostroumov, M. Pivi, F. Pilat, M. Poelker, A. Prokudin, R. Rimmer, T. Satogata, H. Sayed, M. Spata, M. Sullivan, C. Tennant, B. Terzić, M. Tiefenback, H. Wang, S. Wang, C. Weiss, B. Yunn, and Y. Zhang, "Science Requirements and Conceptual Design for a Polarized Medium Energy Electron-Ion Collider at Jefferson Lab," p. 160, 2012.

[9] A. Accardi, J. L. Albacete, M. Anselmino, N. Armesto, E. C. Aschenauer, A. Bacchetta, D. Boer, W. K. Brooks, T. Burton, N. B. Chang, W. T. Deng, A. Deshpande, M. Diehl, A. Dumitru, R. Dupré, R. Ent, S. Fazio, H. Gao, V. Guzey, H. Hakobyan, Y. Hao, D. Hasch, R. Holt, T. Horn, M. Huang, A. Hutton, C. Hyde, J. Jalilian-Marian, S. Klein, B. Kopeliovich, Y. Kovchegov, K. Kumar, K. Kumerički, M. A. C. Lamont, T. Lappi, J. H. Lee, Y. Lee, E. M. Levin, F. L. Lin, V. Litvinenko, T. W. Ludlam, C. Marquet, Z. E. Meziani, R. McKeown, A. Metz, R. Milner, V. S. Morozov, A. H. Mueller, B. Müller, D. Müller, P. Nadel-Turonski, A. Prokudin, V. Ptitsyn, X. Qian, J. W. Qiu, M. Ramsey-Musolf, T. Roser, F. Sabatié, R. Sassot, G. Schnell, P. Schweitzer, E. Sichtermann, M. Stratmann, M. Strikman, M. Sullivan, S. Taneja, T. Toll,

D. Trbojevic, T. Ullrich, R. Venugopalan, S. Vigdor, W. Vogelsang, C. Weiss, B. W. Xiao, F. Yuan, Y. H. Zhang, L. Zheng, H. Paukkunen, A. Prokudin, V. Ptitsyn, X. Qian, J. W. Qiu, M. Ramsey-Musolf, T. Roser, F. Sabatié, R. Sassot, G. Schnell, P. Schweitzer, E. Sichtermann, M. Stratmann, M. Strikman, M. Sullivan, S. Taneja, T. Toll, D. Trbojevic, T. Ullrich, R. Venugopalan, S. Vigdor, W. Vogelsang, C. Weiss, B. W. Xiao, F. Yuan, Y. H. Zhang, and L. Zheng, "Electron Ion Collider: The Next QCD Frontier - Understanding the glue that binds us all," *Eur. Phys. J. A.*, vol. 58, p. 268, 2016.

[10] S. Abeyratne, D. Barber, A. Bogacz, P. Brindza, Y. Cai, A. Camsonne, P. Chevtsov, E. Daly, Y. S. Derbenev, D. Douglas, V. Dudnikov, B. Erdelyi, Y. Filatov, D. Gaskell, J. Grames, J. Guo, L. Harwood, C. Hyde, K. Jordan, A. Kimber, G. A. Krafft, M. Kondratenko, R. Li, F. Lin, T. Mann, P. Mcintyre, V. S. Morozov, Y. M. Nosochkov, K. Park, F. Pilat, M. Poelker, N. J. Pogue, R. Rimmer, Y. Roblin, T. Satogata, A. Sattarov, M. Spata, R. Suleiman, M. Sullivan, A. Sy, H. Wang, M.-h. Wang, S. Wang, U. Wienands, H. Zhang, Y. Zhang, Z. Zhao, A. Institutions, N. News, and M. Park, "MEIC Design Summary," pp. 1–65, 2015.

[11] D. Edwards and M. Syphers, *An Introduction to the Physics of High Energy Accelerators*. Wiley Series in Beam Physics and Accelerator Technology, Wiley, 2008.

[12] M. Conte and W. MacKay, *An Introduction to the Physics of Particle Accelerators*. World Scientific, 2008.

[13] E. Wilson and E. Wilson, *An Introduction to Particle Accelerators*. Oxford University Press, 2001.

[14] A. Chao and M. Tigner, *Handbook of Accelerator Physics and Engineering*. Handbook of Accelerator Physics and Engineering, World Scientific, 1999.

[15] USPAS, "US Accelerator School," 2016. http://uspas.fnal.gov.

[16] CERN, "The CERN Accelerator School," 2016. http://cas.web.cern.ch/cas/.

[17] K. L. Brown, "A First- and Second-Order Matrix Theory for the Design of Beam Transport Systems and Charged Particles Spectrometers, number = SLAC-75-rev-4, institution = SLAC, year = 1982," tech. rep.

[18] Y. H. Chin, “Effects of Non-Zero Dispersion at Crab Cavities on the Beam Dynamics* .,,” Tech. Rep. LBL-29581, LBL, 1991.

[19] ATLAS Collaboration, “Measurement of the total cross section from elastic scattering in pp collisions at $\sqrt{s} = 7$ TeV with the ATLAS detector,” *Nuclear Physics B*, vol. 889, pp. 486–548, dec 2014.

[20] K. Ohmi, R. Tomás, Y. Funakoshi, R. Calaga, T. Ieiri, Y. Morita, K. Nakanishi, K. Oide, Y. Ohnishi, Y. Sun, M. Tobiyama, and F. Zimmermann, “Response of colliding beam-beam system to harmonic excitation due to crab-cavity rf phase modulation,” *Physical Review Special Topics - Accelerators and Beams*, vol. 14, no. 11, p. 111003, 2011.

[21] J. Qiang, M. A. Furman, and R. D. Ryne, “Strong-strong beam-beam simulation using a Green function approach,” *Physical Review Special Topics - Accelerators and Beams*, vol. 5, no. 10, p. 104402, 2002.

[22] R. B. Palmer, “Energy Scaling, Crab Crossing, and the Pair Problem,” *eConf*, vol. C8806271, pp. 613–619, 1988.

[23] H. Padamsee, J. Knobloch, and T. Hays, *RF Superconductivity for Accelerators.* Germany: Wiley-VCH, 2008.

[24] H. Padamsee, *RF Superconductivity.* Germany: Wiley-VCH, 2009.

[25] K. I. Wysoki, “Remarks on the first hundred years of superconductivity,” no. 2, pp. 1–5, 2011.

[26] J. R. Delayen and H. Wang, “New compact TEM-type deflecting and crabbing rf structure,” *Phys. Rev. ST Accel. Beams 12 062002*, vol. 062002, pp. 1–10, 2009.

[27] B. Xiao, L. a. f. Alberty, S. Belomestnykh, I. Ben-Zvi, R. Calaga, C. Cullen, O. Capatina, L. Hammons, Z. Li, C. Marques, J. Skaritka, S. Verdu ´ Andres, and Q. Wu, “Design, prototyping, and testing of a compact superconducting double quarter wave crab cavity,” *Phys. Rev. ST Accel. Beams*, vol. 18, p. 041004, Apr 2015.

[28] S. U. D. Silva and J. R. Delayen, "Design evolution and properties of superconducting parallel-bar rf-dipole deflecting and crabbing cavities," *Phys. Rev. ST Accel. Beams 16 012004*, vol. 012004, pp. 1–19, 2013.

[29] B. Hall, *Designing the Four Rod Crab Cavity for the High-Luminosity LHC Upgrade.* PhD thesis, Cockroft Institute UK, 2014.

[30] J. Tuckmantel, "The Fundamental Beam Loading Theorem," Tech. Rep. CERN-ATS-Note-2011-002 TECH, CERN, Geneva, CH, 2011.

[31] D. Van Delft and P. Kes, "The discovery of superconductivity," *Physics Today*, vol. 63, no. 9, pp. 38–43, 2010.

[32] C. Enss and S. Hunklinger, *Low-Temperature Physics.* Germany: Springer, 2010.

[33] W. Meissner and R. Ochsenfeld, "Ein neuer Effekt bei Eintritt der Supraleitfähigkeit," *Naturwissenschaften*, vol. 21, pp. 787–788, Nov 1933.

[34] A. Pippard, "An experimental and theoretical study of the relation between magnetic field and current in a superconductor," *Proc. Roy. Soc. London*, vol. 216 A, pp. 547–568, 1953.

[35] M. Tinkham, *Introduction to superconductivity.* USA: Courier Corporation, 1996.

[36] V. L. Ginzburg and L. D. Landau, "On the Theory of superconductivity," *Zh. Eksp. Teor. Fiz.*, vol. 20, pp. 1064–1082, 1950.

[37] M. Cyrot, "Ginzburg-landau theory for superconductors," *Reports on Progress in Physics*, vol. 36, no. 2, p. 103, 1973.

[38] J. Bardeen, "Theory of the Meissner Effect in Superconductors," *Phys. Rev.*, vol. 97, pp. 1724–1725, Mar 1955.

[39] L. N. Cooper, "Bound Electron Pairs in a Degenerate Fermi Gas," *Phys. Rev.*, vol. 104, pp. 1189–1190, Nov 1956.

[40] J. Bardeen, L. N. Cooper, and J. R. Schrieffer, "Microscopic Theory of Superconductivity," *Phys. Rev.*, vol. 106, pp. 162–164, Apr 1957.

[41] T. Abe, K. Akai, N. Akasaka, M. Akemoto, A. Akiyama, M. Arinaga, Y. Cai, K. Ebihara, K. Egawa, A. Enomoto, E. Ezura, J. Flanagan, S. Fukuda, H. Fukuma, Y. Funakoshi, K. Furukawa, T. Furuya, J. Haba, K. Hara, T. Higo, S. Hiramatsu, H. Hisamatsu, H. Honma, T. Honma, K. Hosoyama, T. Ieiri, N. Iida, H. Ikeda, M. Ikeda, S. Inagaki, S. Isagawa, H. Ishii, A. Kabe, E. Kadokura, T. Kageyama, K. Kakihara, E. Kako, S. Kamada, T. Kamitani, K.-i. Kanazawa, H. Katagiri, S. Kato, T. Kawamoto, S. Kazakov, M. Kikuchi, E. Kikutani, K. Kitagawa, H. Koiso, Y. Kojima, I. Komada, T. Kubo, K. Kudo, S.-i. Kurokawa, K. Marutsuka, M. Masuzawa, S. Matsumoto, T. Matsumoto, S. Michizono, K. Mikawa, T. Mimashi, T. Mitsuhashi, S. Mitsunobu, T. Miura, K. Mori, A. Morita, Y. Morita, H. Nakai, H. Nakajima, T. T. Nakamura, H. Nakanishi, K. Nakanishi, K. Nakao, H. Nakayama, M. Nishiwaki, Y. Ogawa, K. Ohmi, Y. Ohnishi, S. Ohsawa, Y. Ohsawa, N. Ohuchi, K. Oide, T. Oki, M. Ono, T. Ozaki, E. Perevedentsev, H. Sakai, Y. Sakamoto, M. Sato, K. Satoh, M. Satoh, Y. Seimiya, K. Shibata, T. Shidara, M. Shimada, S. Stanic, M. Shirai, A. Shirakawa, T. Sueno, M. Suetake, Y. Suetsugu, R. Sugahara, T. Sugimura, T. Suwada, O. Tajima, S. Takano, S. Takasaki, T. Takenaka, Y. Takeuchi, M. Tawada, M. Tejima, M. Tobiyama, N. Tokuda, K. Tsuchiya, S. Uehara, S. Uno, Y. Wu, N. Yamamoto, Y. Yamamoto, Y. Yano, K. Yokoyama, M. Yoshida, S.-i. Yoshimoto, K. Yoshino, M. Yoshioka, D. Zhou, F. Zimmermann, and Z. Zong, "Achievements of KEKB," *Progress of Theoretical and Experimental Physics*, no. 3, p. 3A001, 2013.

[42] M. Borland, "User Manual for Elegant V. 29.0.0," 2016.

[43] A. Castilla, V. S. Morozov, T. Satogata, and J. R. Delayen, "Effects of crab cavities' multipole content in an electron-ion collider.," in *Proc. 6th International Particle Accelerator Conference*, p. 3561, JACoW, May 2015.

[44] X. Huang, "Coupled beam motion in a storage ring with crab cavities," *Phys. Rev. Accel. Beams*, vol. 19, p. 024001, Feb 2016.

[45] F. Ciocci, G. Dattoli, and M. Migliorati, "Generalized twiss coefficient including transverse coupling and e-beam growth," in *Proc. 10th European Particle Accelerator Conference*, p. 1966, EPS-AG, June 2006.

[46] F. Lin and et al., "Interaction region design and detector integration at JLab's MEIC.," in *Proc. 2013 North American Particle Accelerator Conference*, p. 508, JACoW, September 2013.

[47] M. Abramowitz and I. A. Stegun, *Handbook of Mathematical Functions: with Formulas, Graphs, and Mathematical Tables.* USA: Dover Publications; 0009-Revised edition, 1965.

[48] A. Castilla and J. R. Delayen, "Multipole and field uniformity tailoring of a 750 MHz rf dipole.," in *Proc. 27th Linear Accelerator Conference*, p. 326, JACoW, August 2014.

[49] S. U. De Silva and J. R. Delayen, "Design of superconducting parallel-bar deflecting/crabbing cavities with improved properties.," in *Proc. 2011 Particle Accelerator Conference*, p. 1021, JACoW, March 2011.

[50] J. R. Delayen, "Medium-β Superconducting Accelerating Structures," in *10th International Workshop on RF Superconductivity*, (Tsukuba, Japan), pp. 152–161, JACoW, 2001.

[51] A. Castilla and J. R. Delayen, "Multipacting optimization of a 750 MHz rf dipole.," in *Proc. 27th Linear Accelerator Conference*, p. 1111, JACoW, August 2014.

[52] K. Hosoyama, K. Hara, A. Kabe, Y. Kojima, Y. Morita, H. Nakai, K. Saito, T. Furuya, K. Akai, H. Hattori, and S. Imatake, "Crab Cavity for KEKB," in *7th International Workshop on RF Superconductivity*, pp. 671–675, JACoW, 1995.

[53] K. Hosoyama, K. Hara, A. Honma, A. Kabe, Y. Kojima, Y. Morita, H. Nakai, K. Nakanishi, K. Akai, K. Ebihara, T. Furuya, S. Mitsunobu, M. Ono, Y. Yamamoto, K. Okubo, K. Sennyu, H. Hara, and T. Yanagisawa, "Construction and Commisioning of Kekb Superconducting Crab Cavities," in *13th International Workshop on RF Superconductivity*, pp. 63–69, JACoW, 2007.

[54] S. U. De Silva and J. R. Delayen, "Multipacting analysis of the superconducting parallel-bar cavity.," in *Proc. 2011 Particle Accelerator Conference*, p. 1018, JACoW, March 2011.

[55] H. Padamsee and A. Joshi, “Secondary electron emission measurements on materials used for superconducting microwave cavities,” *Journal of Applied Physics*, vol. 50, no. 2, pp. 1112–1115, 1979.

[56] SLAC, “ACE3P-Advanced Computational Electromagnetic Simulation Suite,” 2016. [Online; accessed 14-June-2016].

[57] US-DOE, “NERSC-National Energy Research Scientific Computing Center,” 2016. `http://www.nersc.gov`[Online; accessed 14-June-2016].

[58] W. K. H. Panofsky and W. A. Wenzel, “Some Considerations Concerning the Transverse Deflection of Charged Particles in Radio Frequency Fields,” *Review of Scientific Instruments*, vol. 27, no. 11, pp. 967–967, 1956.

[59] S. U. De Silva and J. R. Delayen, “Multipole field effects for the superconducting parallel-bar/rf-dipole deflecting/crabbing cavities.,” in *Proc. 26th Linear Accelerator Conference*, p. 981, JACoW, September 2012.

[60] R. G. Olave, S. U. De Silva, J. R. Delayen, and Z. Li, “Study of cavity imperfection impact on rf-parameters and multipole components in a superconducting rf-dipole cavity.,” in *Proc. 2013 North American Particle Accelerator Conference*, p. 871, JACoW, September 2013.

[61] A. Castilla, J. R. Delayen, and G. A. Krafft, “Design of electron and ion crabbing cavities for an electron-ion collider.,” in *Proc. 3rd International Particle Accelerator Conference*, p. 2447, JACoW, May 2012.

[62] S. U. De Silva, J. R. Delayen, and H. Park, “Mechanical analysis of the 400 MHz rf-dipole crabbing cavity prototype for the LHC high luminosity upgrade.,” in *Proc. 2013 North American Particle Accelerator Conference*, p. 862, JACoW, September 2013.

[63] ANSYS, “Ansys Academic Research, Release 13.0, Structural Mechanics Analysis, ANSYS, Inc.,” 2010. `http://www.ansys.com`.

[64] S. U. D. Silva and J. R. Delayen, “Cryogenic test of a proof-of-principle superconducting rf-dipole deflecting and crabbing cavity,” *Phys. Rev. ST Accel. Beams 16 082001*, vol. 082001, pp. 1–9, 2013.

[65] S. U. De Silva, J. R. Delayen, and A. Castilla, "Compact superconducting rf-dipole cavity designs for deflecting and crabbing applications.," in *Proc. 4th International Particle Accelerator Conference*, p. 2483, JACoW, May 2013.

[66] US-DOE, "SBIR/STTR Office of Science, US-DOE," 2016. `http://science.energy.gov/sbir/`[Online; accessed 23-March-2016].

[67] W. Singer, A. Ermakov, and X. Singer, "RRR-Measurement Techniques on High Purity Niobium," tech. rep., DESY, 2010.

[68] H. Piel, "Superconducting Cavities," Tech. Rep. CERN-89-04, CERN, 1989. CAS - CERN Accelerator School : Superconductivity in Particle Accelerators.

[69] J. Bardeen, L. N. Cooper, and J. R. Schrieffer, "Theory of Superconductivity," *Physical Review*, vol. 108, no. 5, pp. 1175–1204, 1957.

[70] J. Vogt, O. Kugeler, and J. Knobloch, "Impact of cool-down conditions at T_c on the superconducting rf cavity quality factor," *Phys. Rev. ST Accel. Beams*, vol. 16, p. 102002, Oct 2013.

[71] A. Gurevich, "Reduction of dissipative nonlinear conductivity of superconductors by static and microwave magnetic fields," *Phys. Rev. Lett.*, vol. 113, p. 087001, Aug 2014.

[72] T. Junginger, "Field dependent surface resistance of niobium on copper cavities," *Phys. Rev. ST Accel. Beams*, vol. 18, p. 072001, Jul 2015.

[73] J. R. Delayen, "Ponderomotive Instabilities And Microphonics A Tutorial*," in *12th International Workshop on RF Superconductivity*, (Ithaca, NY), pp. 35–39, 2005.

[74] A. Castilla and J. R. Delayen, "Analysis of a 750 MHz rf dipole.," in *Proc. 17th International Conference on RF Superconductivity*, p. 1200, JACoW, Sep 2015.

[75] H. Park, A. Castilla, S. U. De Silva, J. R. Delayen, and V. Morosov, "Analyses of 476 MHz and 952 MHz crab cavities for Jefferson Lab electron-ion collider.," in *Proc. 7th International Particle Accelerator Conference*, p. 2348, JACoW, May 2016.

[76] Z. A. Conway, A. Barcikowski, S. M. Gerbick, M. J. Kedzie, M. P. Kelly, S. H. Kim, S. V. Kutsaev, R. C. Murphy, A. Nassiri, P. N. Ostroumov, T. C. Reid, T. L. Smith, and A. A. Zholents, "Development and Test Results of a Quasi-Waveguide Multicell Resonator," in *Proc. 5th International Particle Accelerator Conference*, p. 2596, JACoW, June 2014.

VITA

Alejandro Castilla
Department of Physics
Old Dominion University
Norfolk, VA 23529

Alejandro Castilla was born on December 21st, 1982 in Mexico City, Mexico. He obtained his Bachelor degree in Physics Engineering from the Autonomous University of Yucatan (UADY) in Merida, Mexico, 2007. Alejandro then joined the Physics Department of the University of Guanajuato (UG) in Leon, Mexico, 2008 and obtained his Masters degree in Physics there in 2010, shortly after he joined the departaments' PhD program. Afterwards, Alejandro enrolled in the graduate program at the Department of Physics of the Old Dominion University (ODU) in Virginia, USA, the fall of 2010 and obtained his second Masters degree in Physics from ODU in 2013. Alejandro is currently a senior fellow physicist in the superconducting radiofrequency section at the European Council for Nuclear Research (CERN) in Geneva, Switzerland.

Typeset using LaTeX.